VALIDATING ANNUAL GROWTH BANDS OF DEEP-SEA BLACK CORALS AND CALCULATING OCEAN RESEVOIR AGES FROM THE GULF OF MEXICO AND SOUTHEASTERN UNITED STATES

A Thesis

by

LESLYE MITTY MOHON

Submitted to the Office of Graduate and Professional Studies of
Texas A&M University
in partial fulfillment of the requirements for the degree of

MASTER OF SCIENCE

Chair of Committee,	E. Brendan Roark
Committee Members,	Ethan Grossman
	Oliver W. Frauenfeld
Head of Department,	Vatche P. Tchakerian

August 2014

Major Subject: Geography

ABSTRACT

Deep–sea black corals have been found to be long-lived and grow in a tree like fashion depositing rings in their skeleton that have been suggested to be annual growth bands. Iodine was used in this study to develop a novel dating method to measure the life spans and growth rates of these black coral, *Leiopathes* sp. The visual growth band count dating method was conducted on three of the GOM specimens and resulted in life spans ranging from 490 ±50 to 1315 ±130 years with growth rates ranging from 11 ±3 to 16 ±2 μm yr^{-1}. The iodine dating method resulted in life spans of 630 ±65 to 1240 ±125 years and growth rates ranging from 10 ±1 to 19 ±3 μm yr^{-1}. The life spans and growth rates that resulted from the counting of iodine peak generally matched the radiocarbon results, which yielded life spans of 620 ±40 to 2040 ±40 Cal yr. BP (before present 1950). The new iodine dating method in conjunction with radiocarbon and visual ring counts from SEM images validated the annual growth bands in the deep-sea black coral *Leiopathes* sp. from the GOM and SEUS.

Using the independent (iodine) age models in conjunction with the radiocarbon records, ocean reservoir age records can be developed for the last ~500 to 1000 years. These findings provide a rare continuous record through time of highly variable reservoir ages suggestive of changing ocean dynamics in association with climatic events in the late Holocene. The preferred explanation for the variability found in these reservoir ages is that the changes in the reservoir ages reflect changes in the strength of the Yucatan current. This study is the first to validate that the rings deposited in the

skeleton of deep-sea black corals, *Leiopathes* sp., are annual growth bands and that peaks in iodine counts associated with the growth band can be used as an independent dating method if good quality thin sections are made before analyses are conducted

In loving memories of,

Rita Elaine Mohon

Rodney Mohon

Javier Chavez

Petra Cirbrian Chavez

Charles “Chuck” Mohon

ACKNOWLEDGEMENTS

I would like to thank my committee chair, Dr. Brendan Roark for believing in me and giving me the opportunity to obtain a Masters of Science. He helped me accomplish a goal that I thought almost impossible to reach by providing me the tools and guidance necessary to be successful. Brendan Roark is someone who has had such a positive impact in my life and for that I will forever be thankful.

To my to supporting committee members, Dr. Ethan Grossman and Dr. Oliver Frauenfeld, I would like to thank them for the guidance and support throughout the course of this research. The feedback and knowledge that they provided to me made my thesis possible. The patience and support that they both showed is greatly appreciated.

I would like to thank those who have directly helped with my thesis project. Renald Guillemetter, for running my thin sections through the SEM and taking the time to help solve some issues with my corals (e.g. bubbling). Tom Guilderson and the CAMS_LLNL for hosting me and teaching me the proper steps to preparing samples for the AMS. Steve Ross, who provided the deep-sea corals utilized in this research project. Nancy Prouty, for providing previously sampled results and guidance to my project. Thanks to the USGS Terrestrial, Marine, and Freshwater Environments-Outer Continental Shelf Ecosystem Program. Thanks to the USGS Coastal, Marine Geology Program, and a grant to Dr. Brendan Roark from The Norman Hackerman Advanced Research Program that supported this work.

I would like to recognize my friends, colleagues, and the faculty at Texas A&M University for keeping me motivated and for all the amazing memories added to my life. Furthermore, I would like to thank Geovany Garcia for his support throughout my graduate studies. Last but not least, thanks to my dad (Paul C. Mohon), mi mama (Maria Mohon), and my loving brother (Daniel P. Mohon), without your love and support I would not be here today.

NOMENCLATURE

AMS	Accelerator Mass Spectrometer
BP	Before Present
Br	Bromine
BSE	Backscatter Electron
CAMS	Central Accelerator Mass Spectrometer
CITES	Convention on International Trade in Endangered Species
CM	Centimeter
DIC	Dissolved Inorganic Carbon
DSC	Deep-Sea Coral
GOM	Gulf of Mexico
GPS	Global Positioning System
I	iodine
JSL	Johnson-Sea-Link
KOH	Potassium hydroxide
LLNL	Lawrence Livermore National Laboratory
M	Meter
MM	Millimeter
MMS	Minerals Management Service
NMFS	National Marine Fisheries Service
NOAA	National Oceanic Atmospheric Administration

PET	Prentaery Thrital
POC	Particulate Organic Carbon
R	Reservoir Ages
ROV	Remotely Operated Vehicle
SEM	Scanning Electron Microscope
SEUS	Southeastern United States
TAP	Thallium Acid Phthalate
TOW	Trawling
U/Th	Uranium Thorium
WDS	Wavelength-Dispersive Spectrometer

TABLE OF CONTENTS

LIST OF FIGURES

LIST OF TABLES

CHAPTER I

INTRODUCTION

Deep-sea corals (DSC) have the potential to be used as an archive of historical oceanographic and biochemical changes of surface and intermediate water processes as they can extend our observations of ocean dynamics and climate well beyond the onset of instrumental records. Thus, long-term, high-resolution, and perhaps annually resolved chronologies records in DSC have to be developed to observe changes in oceanographic and biochemical changes. In addition, un-sustainable fishing practices along with other anthropogenic impacts (pharmaceutical products, oil and gas exploration, mining, and pipe/cable laying) that threaten DSC have pushed scientists and resource managers to develop management practices in order to better conserve DSC. Management plans depend on age and growth rate studies to determine maximum sustainable yields in precious coral fisheries, and to estimate growth rates and resilience to damaging fishing practices. This study utilized six specimens, Leiopathes sp., four from the Gulf of Mexico (GOM) and two from the Southeastern United States (SEUS) collected at depths ranging from 300 m to 700 m in order to validate annual growth bands and to develop an independent chronology using iodine measurements. With the independent chronometer, radiocarbon measurements can be used to calculate reservoir ages in order to trace ocean circulation changes.

CHAPTER II

VALIDATING ANNUAL GROWTH BANDS

2.1 Introduction

Deep-sea corals (DSC) have the potential to be used as an archive of historical oceanographic and biogeochemical changes of surface and intermediate water processes (Adkins et al., 1998; Andrew et al., 2005; Prouty et al., 2011; Roark et al., 2006; Robinson et al., 2005; Sherwood et al., 2005; Williams et al., 2006). They can also extend our observations of ocean dynamics and climate well beyond the onset of instrumental records (Roark et al., 2006, 2009; Robinson et al., 2005; Prouty et al., 2011; Sherwood et al., 2005). Furthermore, instrumental records are not sufficiently widespread or long-standing enough to allow predictive mechanistic understandings of paleoclimate and oceanographic events to be constructed. Thus long-term, high-resolution, and perhaps annually resolved chronological records in marine archives have to be developed to observe changes in oceanographic and biochemical changes.

2.1.1 DSC as Archives of Oceanographic and Climate Change

Despite living below the photic zone, proteinaceous DSCs are linked to changes in the surface ocean since they feed upon rapidly exported particulate organic matter (POM) (Druffel et al., 1995; Prouty et al., 2011; Roark et al., 2005, 2006, 2009; Sherwood et al., 2009). The ^{14}C content of the atmosphere and the deep-sea are coupled,

but our knowledge of the history of these two reservoirs is vastly different (Robinson et al., 2005).

Robinson et al. (2005) used radiocarbon analyses of DSC and paired benthic-planktonic foraminifera to develop a deep ocean record with detailed information of glacial to Holocene time period. These deep-ocean records support the notion of a bipolar seesaw with increased Northern-source deeper water formation linked to northern Hemisphere warming and vice-versa (Robinson et al., 2005). Komugabe et al. (2013) used U/Th measurements from a deep-sea black coral to develop an independent chronology to calculate the reservoir ages in the Tasman Sea to understand regional ocean circulation patterns. These results indicated lower reservoir ages after 1900 AD, which were potentially caused by variations in the lateral advection of ^{14}C-rich waters of tropical and temperate origin, or changes in ventilation of surface waters overlaying the Norfolk Ridge region due to differences in mixing with deeper ^{14}C-poor water masses (Komugabe et al., 2013).

Geochemical signatures captured in coral skeletal protein including stable carbon isotopes ($\delta^{13}C$) have been used to detect the "Seuss effect" (decrease on oceanic $\delta^{13}C$ caused by anthropogenic burning of fossil fuel and biomass), thus establishing coral skeleton protein (particulate organic mater) as a useful archive of global biochemical cycling (Sherwood et al., 2005; Sherwood et al., 2009). Geochemical analyses of the organic node of bamboo coral has been used to track a variety of biochemical cycles in overlying surface waters. By linking these analyses with those from the calcitic internodes, which are derived from dissolved inorganic carbon (DIC) at depth, detailed

records of both surface and deep-water processes can be generated from the same coral (Roark et al., 2005; Sherwood et al., 2009).

2.1.2 Conservation and Fishery Management

Recent research expeditions conducted over the last couple of decades have provided considerable new information on the distribution, habitat, and biodiversity of DSC communities found as far north as the Norwegian Sea and as far south as the Ross Sea in Antarctica (Stanley and Cairns, 1988). These expeditions and explorations have identified many new DSC beds and increased awareness of the importance of these resources. These DSC provide essential habitats that are used for feeding, spawning, and as nursery grounds for a range of commercially important fish and crustacean populations (Roberts and Hirshfield, 2004; Witherell et al., 2000). Evidence that corals are important to fisheries includes fisherman's accounts that areas with DSC are good fishing grounds, and that the disappearance of corals influences the fish distribution in the area (Roberts and Hirshfield, 2004). These DSC disappearances or disturbances are mostly due to anthropogenic impacts (jewelry trade harvesting, bottom trawling, pharmaceuticals products, oil and gas exploration, mining, and pipe/cable laying).

It was estimated in 1970, that precious coral jewelry earned a total of $300 million of world retail sales (Grigg, 1976). A study of the history of black coral sustainable fisheries in Hawaii conducted by Grigg (2001) reported that 22 pounds of shallow black corals were harvested per day, averaging $25 per pound for each dive made by Maui divers. By 1969, a dozen companies had joined these Maui divers

producing $2 million in gross sales of black coral jewelry. One of the concerns about the jewelry trade was how little was known about the ecology of black corals, and whether their growth rates were sufficient to sustain commercial harvest rates (Grigg, 2001).

Several studies have shown that bottom trawling can damage or destroy DSC, reducing the 3-dimensional complexity of the bottom topography and decreasing biodiversity and biomass (Koslow et al., 2001; Morgan et al., 2005). Bottom trawling consists of a large bag-shaped net that is dragged along the seafloor to catch fish, shrimp, and crabs. In Norwegian waters, Fossa et al. (2002) estimated that one-third to one-half of the deep water reefs have been damaged or destroyed by bottom trawling. In Alaskan waters alone, the National Marine Fisheries Service (NMFS) estimated that over one million pounds of corals and sponges were removed from the seafloor annually between 1997 and 1999 by commercial fishing, ~90% of which was by bottom trawling (NMFS, 2003). This supports the view of many scientists, managers, and fisherman, that bottom trawling is the most ecologically destructive fishing practice (Chuebpagdee et al., 2003).

These non-sustainable fishing practices along with other anthropogenic impacts (pharmaceuticals products, oil and gas exploration, mining, and pipe/cable laying) have pushed scientists to develop management practices for the conservation of these long-lived slow-growing corals (Roark et al., 2009; Roberts and Hirshfield, 2004). Management plans depend on age and growth rate studies to determine maximum sustainable yields in the precious coral fisheries and to estimate growth rates and resilience to damaging fishing practices. Overexploitation of these corals without proper management practices could easily lead to local population extinctions (Morgan et al.,

2007). This is significant because factors such as low frequency recruitment events, delayed first reproduction, limited larval dispersal, and the demonstrated longevity and slow growth rates suggest that it may take centuries to millennia, if ever, for extreme long-lived species (deep-sea black and gold coral) to recover from these negative impacts.

Black corals (Antipatharia) are protected by international treaties and are listed in Appendix II of the Convention on International Trade in Endangered species (CITES) of 1981, restricting their exportation and importation. In the United States, the Magnusson Stevenson Act requires that marine resources, which include DSC, be managed and protected from such negative impacts and overexploitation. United States, federal agencies with deep-sea coral management authority include NMFS, NOAA's National Marine Sanctuary Program, and the Minerals Management Service (MMS) in the Department of Interior. In other parts of the world such as Canada, Europe, and New Zealand, laws and regulations protect local DSC populations; most of these laws include prohibiting bottom trawling (Roberts and Hirshfield, 2004).

2.1.3 Deep-Sea Black Coral

The deep-sea black corals belong to the genus *Leiopathes* and have yellow/orange tissue but acquire their common name from the coral's black skeleton (Figure 1), which can grow to more than 2 m in height (Roark et al., 2009). These DSC are not true "coral" like the scleractinians or hermatypic-reef building corals that have hard calcareous skeletons supporting softer tissue and consume algae (zooxanthelle)

(Bradley, 1999; Hillaire-Marcel and De Vernal, 2007). These black corals have mainly organic, semi-precious skeletons known as antipathin, a composite of chitin and protein (Goldberg, 1991; Nowak et al., 2009). Black corals have lustrous, hard, and sturdy skeletons that stand upright on ocean floors, seamounts and continental margins worldwide at depths of ~30 to 6,000 m and temperatures ranging between 4* and 20*C (Adkins, 1998; Prouty et al., 2001; Roark et al., 2009; Nowak et al., 2009). The skeletons of black corals are comprised mainly of organic matter, which consists of successive layers of chitin and protein micro-layers "glued" together by an organic cement layer. The mass of the skeletal organic component is made of almost 60% protein, 15% chitin, 1.5% lipid, and 1.0% carbohydrate (Goldberg, 1991). Previous studies have confirmed that deep-sea black corals are suspension feeders and get their nutrients from particulate organic carbon (POC), which is composed of detritus, marine snow, and plankton that fall from the ocean's surface (Prouty et al., 2011; Roark et al., 2009).

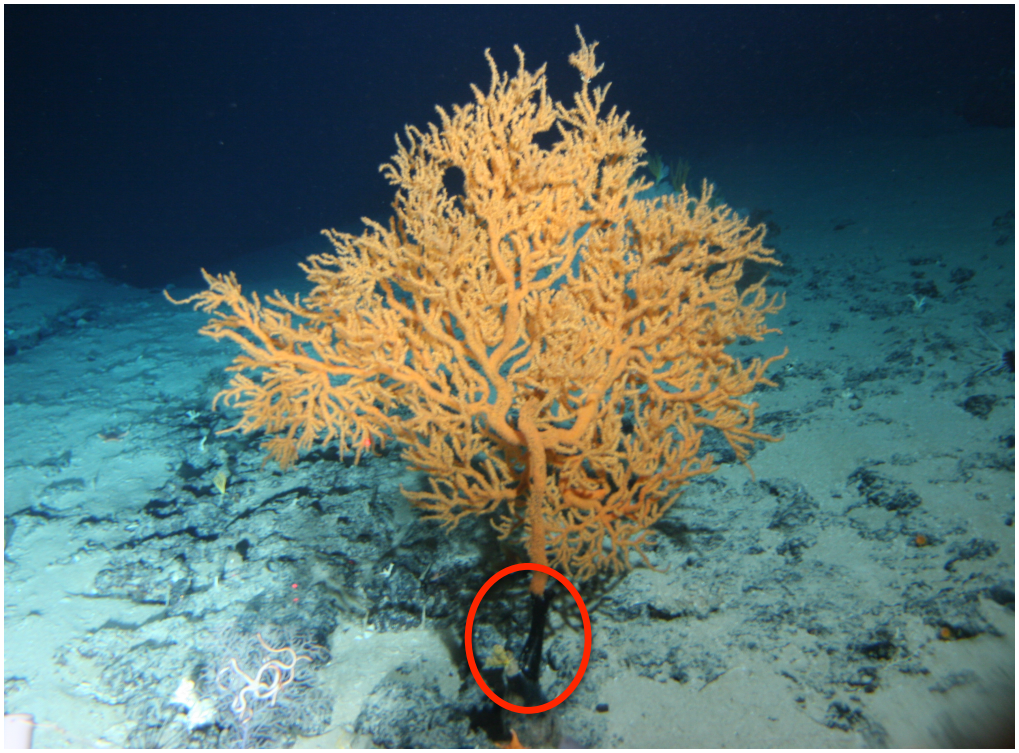

Figure 1 *Leiopathes* sp. deep-sea coral. *Leiopathes* sp. (Antipatharian order) coral has yellow/orange tissue but gets its common name from the coral's black skeleton (circled in red). This is a specimen from the Hawaiian Island (Hawaiian Under Sea Research Laboratory).

Specimens of *Leiopathes* sp. from the Gulf of Mexico (GOM) and Southeastern United States (SEUS) shelf will be analyzed to determine the ages, life spans, and growth rates using the traditional growth band counting method, radiocarbon analyses, and a novel dating method based on iodine concentrations associated with growth bands. This novel approach focuses on identifying peaks in iodine concentrations to develop a high-resolution, annually-resolved chronology. The well-established radiocarbon dating method will be used to validate both the iodine and growth band count chronologies. If the growth bands and associated peaks in iodine concentrations are in fact annual, then the ages and growth rates of black corals can be determined independently of the radiocarbon dating method.

2.2 Determining Ages and Growth Rates

Black coral skeletons are composed of thin, concentric bands of protein and chitinous organic material, allowing for the development of a growth chronology (Goldberg, 1991; Williams et al., 2007). A gorgonian bamboo coral from the Gulf of Alaska revealed alternating light and dark growth rings that could be counted. The results revealed that these bamboo corals did not have annual growth rings, but more likely formed as a result of monthly cycles (Roark et al., 2005). *Leiopathes* sp. also revealed tree-like growth bands of proteinaceous and chitinous material that could result in decadally-resolved and perhaps annually-resolved paleoceanographic records (Prouty et al., 2011). Few, if any, studies have made systematic attempts to validate the annual periodicity of these tree-like growth bands in deep-sea black corals.

Different dating methods have been used to determine the life spans and growth rates of DSC. Past studies have used tagging (Grigg, 1976; Parish and Roark, 2009), counting visual rings presumed to be annual (Grigg, 2002; William et al., 2006), as well as radiometric techniques such as ^{210}Pb (Andrew et al., 2005; Williams et al., 2006), radiocarbon (Roark et al., 2005, 2006, 2009; Prouty et al., 2011), and uranium-thorium (U/Th) (Komugabe et al., 2013). The tagging dating method allows the coral to continue to grow in their natural environment, but is restricted to finding the corals from the initial visit in pristine conditions because of environmental impacts or anthropogenic disturbances can destroy or alter the position of the coral. The visual ring count dating method uses the actual growth bands found in the coral's skeleton to obtain the life spans and growth rates, instead of using chemical analysis that may not adequately represent or resolve these visual growth bands. The visual ring count dating method is subjective because observers can have different definitions of growth bands, and it relies on good quality SEM images to adequately resolve the growth bands. The ^{210}Pb dating method provides life spans and growth rates up to ~200 years, but it assumes a constant growth rate. Using radiocarbon, coral specimens can be dated from modern to ~50,000 years BP (Before Present, 1950) and can measure small sample sizes (e.g. 1 mg) but assumes the atmospheric concentrations of radiocarbon remained constant. The U/Th method can date corals from ~10 to ~350,000 years BP but assumes that the sample is a closed system, which means U or Th has been gained or lost.

2.2.1 Tagging Dating Method

The tagging and dating studies of shallow black corals (*Antipathes dichotoma* and *Antipathes grandis*) were conducted at depths between 25 to 70 m off the coast of Kauai and Maui, Hawaii (Grigg, 1976). Over a 3.5-year time span, 150 dives were performed with scuba gear, which limited the depth and amount of time the diver had to acquire the coral measurements and observations. The deeper depths ranging from 75 to 300 m were surveyed 31 times using a submersible (Star II) and some observations were made using a remotely controlled television camera. Twenty-one tagged corals were observed on an approximately annual basis. Sixteen of the colonies were *A. dichotoma* and five colonies were *A. grandis*. Grigg (1976) found that the average annual linear growth rate over the 3.5-year time period was 6.42 cm for *A. dichotoma* and 6.12 cm for *A. grandis*, indicating fast growing corals. Grigg (1974) reported growth rates of 5.86 cm per year for *A. dichotoma* and 2.92 mm per year for *A. grandis*.

A tagging study by Parish and Roark (2009) revisited multiple corals (*Gerardia* sp.) to measure the linear extension rate over 1-9 year period. The locations of the corals were acquired using GPS-based slant range positioning from the submersible's support vessel. Once located, the coral colonies were marked and the overall heights and widths were measured to examine the differences in linear growth rates associated with the maturity of the colony. When possible, on larger colonies (>100), the length of branches were also measured. The initial height of the marked gold coral colonies ranged from 10 to 250 cm. Video recordings and photographs, along with a calibrated laser scale that is projected on the coral colony, were used for reference. Natural landmarks or the

placement of numbered concrete flower pots (Figure 2) were also used to verify the colony's identity and serve as a reference (Parrish and Roark, 2009). For the tagging dating method to be successful, a return visit to the study site is essential.

The time between the initial measurements and the 2007 follow-up visit ranged from 1 to 9 years. Changes in shape and patterns of each colony's distal branches were checked, noting any differences. Measurements on subsequent visits were repeated without reviewing the data from the initial measurements to limit observer bias. Parish and Roark (2009) successfully revisited 48 colonies, resulting in 70 measurements to compare with values from the initial visits. They found that the overall height of the coral colonies relative to the marked concrete flower pots did not indicate any change between the initial and follow up visits, suggesting little if any growth. No changes were observed in the shape profiles of the distal branches when the colonies were compared to the video from the initial visit. Two colonies had sustained obvious physical damage to the skeletal structure and were not included in the analyses. The reason for suggesting little growth in the gold coral colonies is due to the bulk of the sample (87%) did not exceed the ±9 cm measurement error (Parish and Roark, 2009).

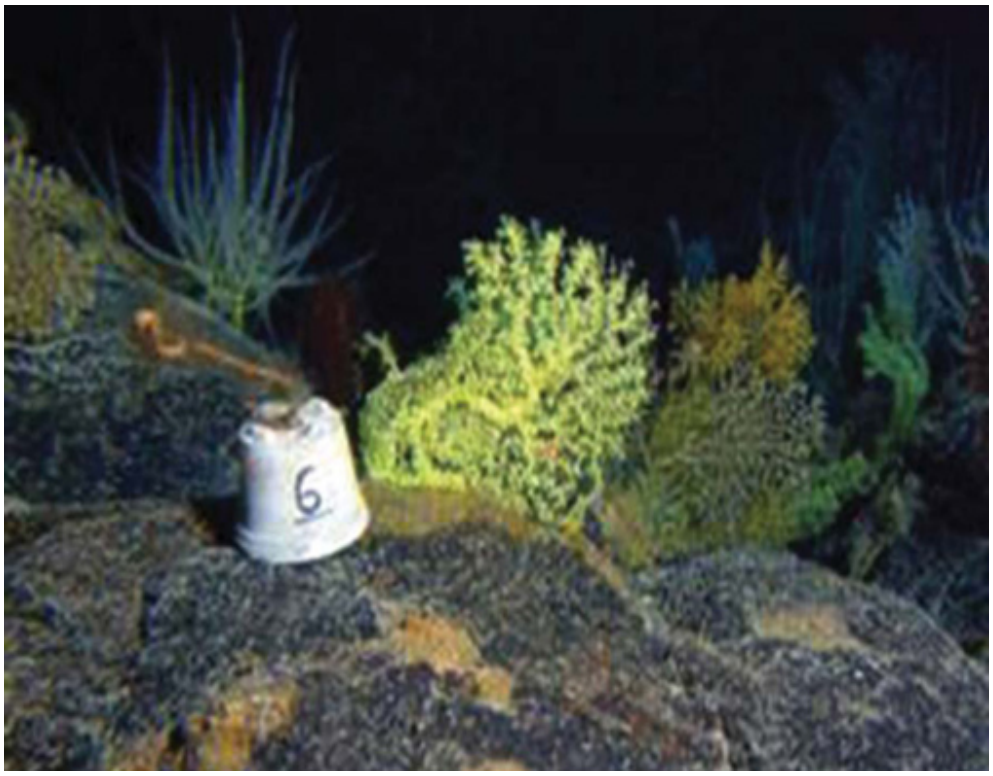

Figure 2 Numbered concrete flower pots. An example of the numbered concrete flower pots that were used for the tagging dating method (Parrish and Roark, 2009).

The difficulties in matching the angle and distance measured in the initial visit were some of the limitations found in the tagging dating method. This limitation created a degree of error from the compromised viewing perspective and had to be considered. If the follow-up measurements were too severely compromised, the colonies of corals were dropped from the analyses (Parrish and Roark, 2009). In conclusion Grigg (1976) estimated a 9 cm per year of linear growth, but Parrish and Roark (2009) observed no linear growth where growth should have been measurable over the 9 years. These findings supported the results from Druffel et al. (1995) and Roark et al. (2005) that suggested slower growth rates based on ^{14}C analyses.

2.2.2 Visual Ring Counts

Previous studies on growth ring structures of black corals indicated that the skeleton is formed of concentric coeval rings (Granger and Goldberg, 1992; Prouty et al., 2011), such that visually counting the rings provides a means of developing radial growth chronologies. Studying shallow-sea black corals (*Antipathes sp*.) from the Red Sea at depths of 2 to 8 m, Risk et al. (2009) found good correspondence between the number of visually counted rings and the calculated ages and growth rates using a bomb-radiocarbon estimate of their ages. To obtain the ages and growth rates of these black corals *(Antipathes sp.*), a chronological record was generated using the visual ring counts and overlapping a reference record (bomb-^{14}C curve) to validate the assumption that the visual growth bands are annually deposited. The visual ring counts indicated ages of >70

years and radial growth rates of ~50 μm yr^{-1}. The bomb-^{14}C dating method showed that the error of visual growth bands count was quite small (Risk et al., 2009).

In another study, the visual ring count method was utilized on deep-sea black coral *Leiopathes* sp. from the GOM (GOM-JSL04-4734-BC1) collected at 300 m depth (Prouty et al., 2011). The visual growth bands were imaged using a SEM and analyzed by counting the optically visible light lines (Figure 3). The dark bands that were visible represent organic cement layers that serve to 'glue' the laminae together (Goldberg, 1991; Nowak et al., 2009). Each visible light band was counted regardless of thickness. These visual ring counts yielded an average age of 576 ±37 years and a growth rate of 17 μm yr^{-1}, which is slightly lower than the calculated ^{14}C age of 670 ±40 years. Taking into account the ^{14}C age error (37 to 40 years), there is a minimum age difference of 21 years based on the two dating techniques (Prouty et al., 2011). The low resolutions of the SEM images were a limitation of the visual ring count method (Figure 3)(Prouty et al., 2011).

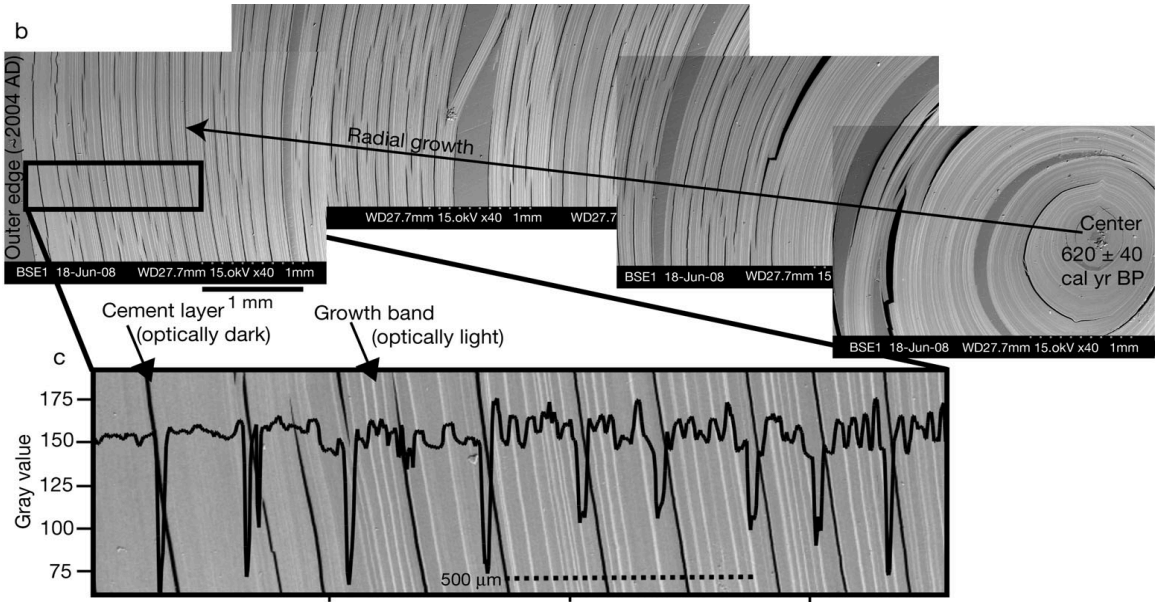

Figure 3 Visual growth bands. Light and dark bands from a *Leiopathes* sp. coral skeleton from the Gulf of Mexico revealed with SEM imaging (90x magnification), appear annual couplets (Prouty et al., 2011).

2.2.3 ^{210}Pb Dating Method

A method often used to determine the growth rates and ages of coral specimens is ^{210}Pb dating. A major assumption with this method is that the coral grows at a constant rate. The excess of ^{210}Pb fractions can be used to determine the age of the subsample but other sources of ^{210}Pb must be accounted for. Detrital particles in the water column are a source of supported ^{210}Pb, which comes from the decay of ^{238}U. The in-growth of the ^{210}Pb fraction comes from *in-situ* decay of daughter-product ^{226}Ra taken from seawater during skeletal formation (Williams et al., 2006). ^{210}Pb has low solubility, which means that it adheres to particulate matter in the water column. Only the last ~200 years can be fully resolved by ^{210}Pb dating. Beyond that, growth rates must be assumed constant and life spans calculated based on extrapolation. In contrast, the radiocarbon dating method is capable of dating specimens with ages ranging from 20 to 50,000 years. DSC from the GOM and SEUS collected at depths of 300 to 500 m were analyzed using the ^{210}Pb dating method. These black corals resulted in ^{210}Pb ages of 198, 290, 386, and 483 years with an average radial growth rate of 14.5 μm yr^{-1} (Williams et al., 2006). In contrast, the ^{14}C ages from the same specimen suggest a life span of 670 years instead of the 386 years reported by the ^{210}Pb dating method (Prouty et al., 2011). The differences in the results were in part due to the assumptions made in the ^{210}Pb dating method, but will further be explained in the radiocarbon dating method section.

2.2.4 Radiocarbon Dating Method

Radiocarbon analysis of DSC specimens with both carbonate and proteinaceous skeletons is the most widely used method to measure the life spans and growth rates of DSC (Adkins, 1998; Sherwood et al., 2005; Prouty et al., 2011; Roark et al., 2005, 2006, 2009; Parish and Roark, 2009; Carreiro-Silva et al., 2013). The range of conventional radiocarbon dating is from modern time (defined as 1950 AD) to ~50,000 years BP and simply relies on 1) knowing the ^{14}C decay rate, 2) measuring the ^{14}C amount in the sample by accelerator mass spectrometer (AMS), and 3) knowing the amount of ^{14}C in the sample at the time of formation. While the principles are straightforward and the methods well established, there are limitations. For example, the atmospheric concentration of radiocarbon has varied over time (Stuiver and Brazunias, 1993; Reimer et al., 2009), which can affect the amount of ^{14}C in the sample at the time of formation. In the marine environment, radiocarbon ages are also corrected for the differences between the atmospheric radiocarbon content and the local radiocarbon content of the surface ocean, known as the "reservoir correction". Taking these limitations into account, the radiocarbon dating method has been effectively used to determine the life spans and growth rates of deep-sea corals.

Prouty et al. (2011) used the radiocarbon dating method to determine the life spans and growth rates of five black corals (*Leiopathes* sp.) from the GOM at 300 m in depth, resulting in life spans ranging from 620 ±40 to 2040 ±40 yr. and growth rates ranging from 8 to 22 μm yr^{-1}. A *Leiopathes* specimen at 450 m depths from off Hawaii yielded a life span of ~2,377 yr. with a growth rate of ~5 μm yr^{-1} (Roark et al., 2006).

Leiopathes specimens from Hawaii that were analyzed from the basal attachment of the coral structure had life spans of 350 to 4,265 ±44 yr. These black corals had radial growth rates of >5 μm yr^{1} (Roark et al., 2009). Roark et al. (2009) also calculated the ages and growth rates for a *Gerardia* sp. specimen (n=36), which gave an average life span of ~970 years and an average growth rate of 36 ±20 μm yr^{-1}(n=31). A determination in DSC using radiocarbon dating is most applicable to growth occurring over centuries to millennia for living specimens, and can be extended for fossil specimens into the tens of thousands of years (Guilderson et al., 2005).

A second method of radiocarbon dating for some living DSC's involves the identification of the anthropogenic bomb-radiocarbon signal from the testing of thermonuclear devices in the 1950's and 1960's. This method is sometimes referred as the bomb-radiocarbon dating method (Roark et al., 2005; Sherwood et al., 2005). The bomb radiocarbon results in a sharp increase in atmospheric ^{14}C starting in the late 1950's, peaking in ~1965 and gradually tailing off since then. In the surface ocean the bomb curve is typically represented by increasing ^{14}C in the early 1960's peaking in the 1970's, followed by an ongoing gradual decrease. The timing of these inflection points can be used to estimate ages in marine organisms where the bomb curve can be reconstructed.

A critical finding of previous studies is that the bomb-carbon spike was found in the outermost millimeter of live collected specimens, which supports the contention that corals are feeding on POC that in turn records sea surface conditions (Roark et al., 2006,

2009; Prouty et al., 2001). Either method will provide a reliable estimate of the calendar age of a specimen for comparison to ages derived from growth band counts.

2.2.5 U/Th Dating Method

The U/Th dating method has shown promising results in dating DSC and in establishing ocean ventilation ages. During the skeletal growth, uranium is co-precipitated from seawater to form part of the coral structure, while thorium concentrations are essentially zero (Bradley, 1999). The principle of U/Th series dating in corals is that uranium in oxygenated environments is about ten thousand times more soluble in seawater than thorium. As corals grow, they incorporate significant amounts seawater uranium and virtually no thorium into their skeletons. This causes a disruption in the equilibrium of the ^{234}U decay chain because the parent ^{234}U isotope is incorporated into the skeleton preferentially, without the daughter ^{230}Th isotope. Over the years, ^{234}U in the skeleton decays into ^{230}Th. The age of the coral is thus determined by calculating the measured amount of ^{230}Th to accumulate from the decay of ^{234}U (Adkins, 1998; Bradley, 1999). Assuming it is a closed system (e.g. no coral recrystallization), this method can be used to date carbonate corals from ~10 to ~350,000 yr BP.

In the only application of this dating method to black corals, Komugabe et al. (2013) dated a deep-sea black coral collected at 560 m depth in the Tasman Sea, between Australia and New Zealand, and obtain a calendar age life-span of 300 ±51 years. The radial growth rates ranged from 2 to 100 μm yr^{-1} and averaged 25 μm yr^{-1} (Komugabe et al., 2013). One advantage of U/Th is that it can be used as an independent

chronometer, providing true calendar ages that can be paired with radiocarbon measurement results to reconstruct ventilation histories in different oceans (Adkins, 1998; Robinson et al., 2005). Future work should apply the U/Th dating method to validate the ages, growth rates, and life spans derived from the novel iodine dating method.

2.3 Trace Element Analyses

A study was conducted to analyze trace element concentrations in the coral skeleton of shallow gorgonian and Antipatharians (Goldberg, 1978). The results showed iodine, bromine, and chlorine were present in the coral specimens and that iodine accounted for 23% of the skeletal weight and >94% of all halogens in the basal portion of the coral's skeleton. There were also signs of increasing iodine with skeletal age in gorgonian and some Antipatharian species (Goldberg, 1978). In a recent study, the inorganic content of black coral specimens from the Chinese coast close to Hong Kong (*Cnidaria, Antipatharia*), from the Caribbean near the Bahamas (*Antipathes Salix* sp.), and from the Gulf of Mexico were analyzed. Transverse cross sections of the corals were created and examined using an SEM image at 900x magnification (Figure 4) to do consecutive elemental mappings from the electron microprobe for C, Na, O, N, Mg, Br, I, Ca, and S (Nowak et al., 2009). Chemical mapping of Cl, K, Al, I, S, Si, Ca, Fe, and Si in black coral by μ-PIXIE method were also presented (Figure 5). The μ-PIXIE method was selected since the detection limits for the elements were lower than in the electron microprobe (Nowak et al., 2009).

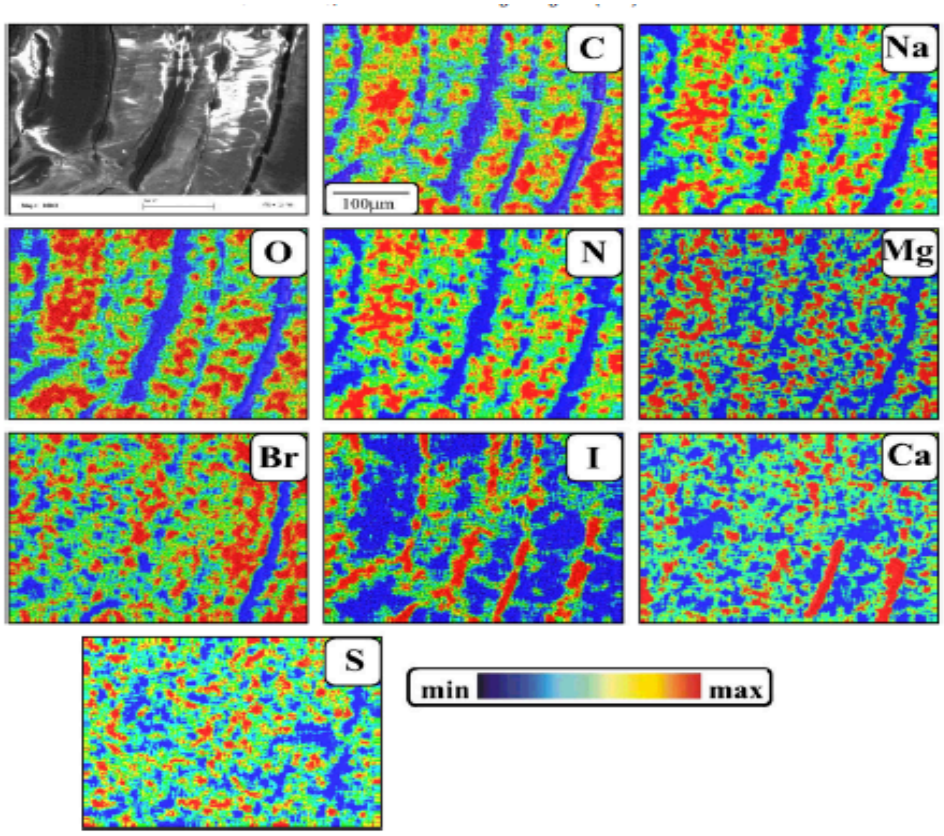

Figure 4 Elemental mapping using a electron microprobe. SEM image (top left) and elemental maps of black coral cross-section using an electron microprobe (Nowak et al., 2009).

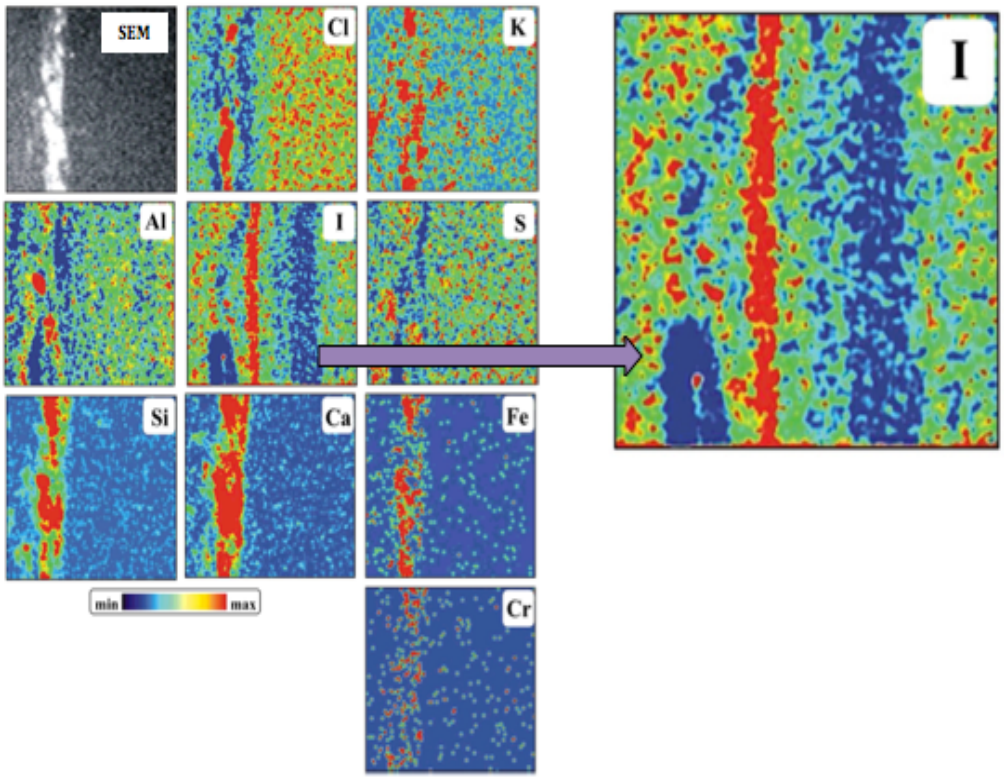

Figure 5 Chemical mapping by µ-PIXIE method. Chemical maps of black coral specimens using the u-Pixie method. The SEM image is from the electron microprobe and the iodine image was enlarged to emphasize the correlation with the SEM image (Nowak et al., 2009).

This study concluded that the gluing layer showed high I, K, Zn, and Ca concentrations that were probably associated with the carboxyamino acids and lipids, which are also concentrated with the gluing zones (Nowak et al., 2009). Nowak et al. (2009) also found that iodine was highly concentrated within the organic zone of the growth bands, giving an indication that perhaps iodine in combination with the growth bands can serve as annual chronometers if it is sampled across the entire radius of a specimen.

2.4 Scanning Electron Microscope (SEM)

A scanning electron microscope (SEM) uses a focused beam of high-energy electrons to generate chemical and textural information about the surface of the samples. Black coral (*Antipathes fioedensis*) colonies for microscopic examinations were collected by scuba diving in Doubtful, New Zealand at depths of 10-20 m. A cross section of the coral's skeleton was treated with formic acid and then imaged using an SEM (Figure 6). The SEM image (Figure 6) shows 6 μm distance of a skeletal cross section that demonstrates that growth rings are an aggregate of thin microlayers (laminae), generally ≤1 μm diameter, separated from one another by a layer of cement (Goldberg et al., 1991). Another study also used an SEM at high resolution (900x) to image the coral's skeleton (Nowak et al., 2009). Based on these results, Nowak et al. (2009) suggest that high iodine concentrations were associated with the visual growth bands in black coral skeletons (Figure 7).

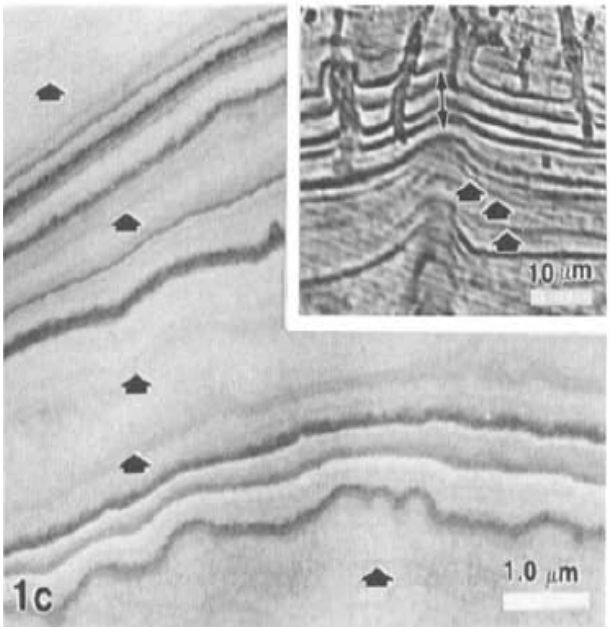

Figure 6 SEM images of multiple growth bands. An SEM image of a black coral (*Antipathes fiordensis*) skeleton in cross sectional disk after formic acid treatment where multiple layers are observed (Goldberg et al., 1991).

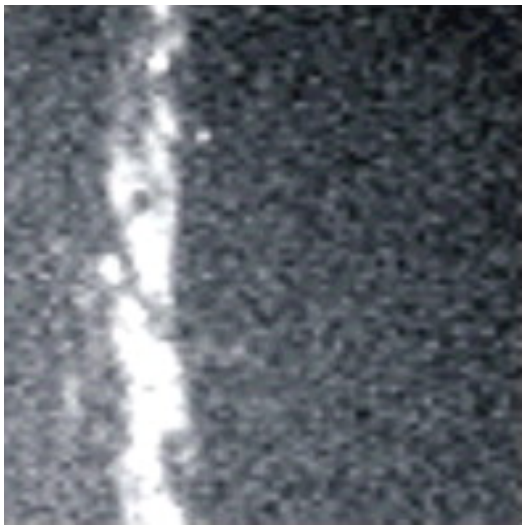

Figure 7 SEM Image of a black coral. An example of a SEM image (250 x 250 µm) of a black coral (*Cnidaria, Antipatharia*) from the Chinese Coast close to Hong Kong (Nowak et al., 2009).

2.5 Study Site and Samples

Dense populations of black corals have been found in all parts of the world's oceans, including the GOM, SEUS, southwestern Pacific, Hawaiian Islands, Gulf of Alaska, the Azores, and tropical western Atlantic. Six families and at least 20 species of Antipatharian have been documented within the Gulf of Mexico region (Brooke and Schroeder, 2007). Black corals (*Leiopathes* sp.) were collected in the Gulf of Mexico along the continental slope and from the SEUS at depths of 300 to 700 m (Figure 8). Six specimens were analyzed as part of this project (Table 1). Four of the corals were collected from the head of the De Soto Canyon and Viosca Knoll east of the Mississippi delta in the Gulf of Mexico. The other two were collected from Stetson Banks located in the SEUS. The samples ID's were labeled indicating the manner that the specimens were collected. Tow samples were collected by a trawl net and were marked (TOW), while samples from the Viosca Knoll region and SEUS were collected by the manned submersible *Johnson-Sea-Link* (JSL). The advantage of using a submersible or ROV to collect specimens is that one can clearly describe the environmental conditions in which the coral was living and most importantly, one can document whether the coral was alive or dead at the time of collection, in contrast to corals collected via trawl.

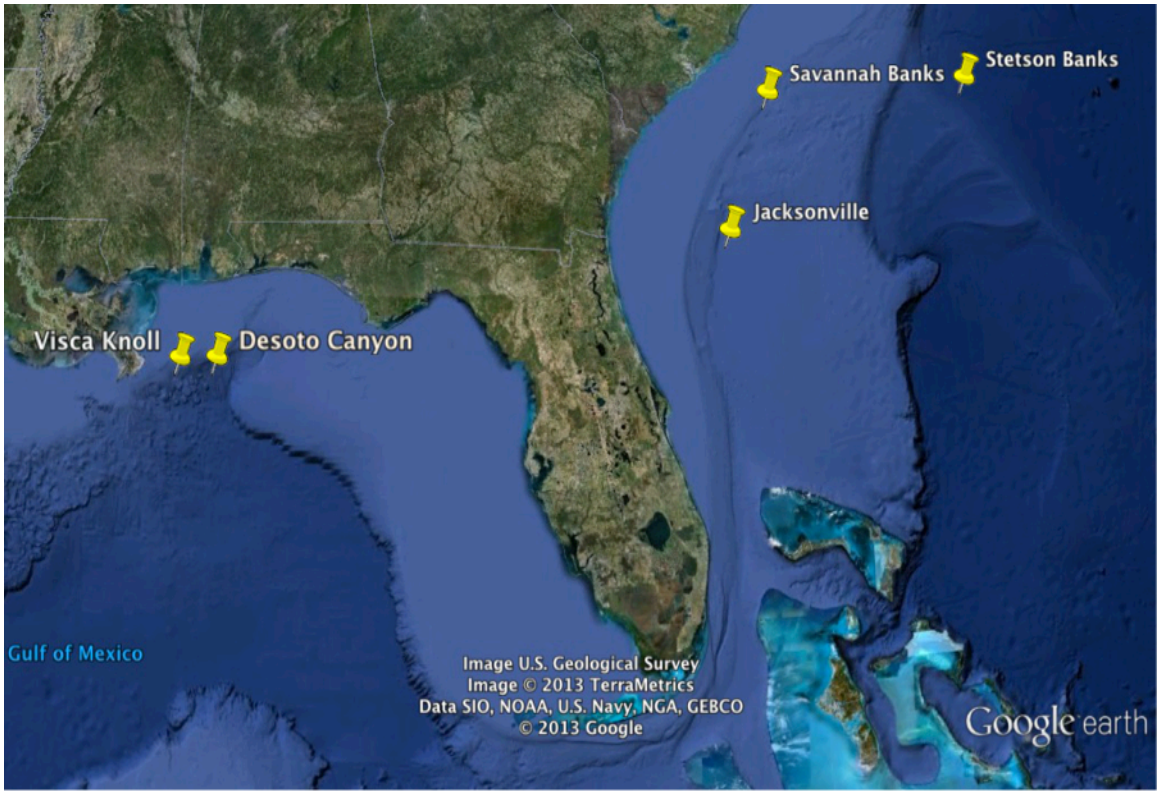

Figure 8 Map of study area. Map of study area of the GOM and SEUS where the *Leiopathes* sp. corals were collected by bottom trawling or a submersible (Google Earth 2013).

Sample ID	Collection Date	Site	Latitude (N)	Longitude (W)	Depth (m)
GOM-JSL04-4734-BC1	07/23/2004	Viosca Knoll	29˚06.22′	88˚23.05′	310
GOM-JLS09-3728-BC1	09/20/2009	Viosca Knoll	29˚06.41′	88˚23.10′	317
GOM-TOW-BC1	11/15/2003	De Soto Canyon	29˚32.24′	86˚52.19′	304
GOM-TOW-BC2	11/15/2003	De Soto Canyon	29˚32.24′	86˚52.19′	304
STET-JSL05-4904-BC1	10/27/2005	Stetson Banks	31˚50.6515′	77˚36.5974′	685
STET-JSL05-4904-BC2	10/27/2005	Stetson Banks	31˚50.6515′	77˚36.5974′	685

Table 1 *Leiopathes* sp. corals. List of six specimens of *Leiopathes* sp. black corals, four of the specimens are from the Viosca Knoll and Desoto Canyon in the GOM and the other two specimens from the SEUS, Stetson Banks. These DSC can be found at a range of 300-700 m depths.

2.6 Methods

2.6.1 Sample Preparation

Multiple (2-4) 0.5 cm thick cross-sectional disks were cut from the basal portion of the black coral (*Leiopathes* sp.) specimens using a diamond band saw. One cross-sectional disk was prepared for SEM analyses by polishing on one side using silicone carbide powder at 120, 400, 600, and 1000 grit size, then cleaned and dried for 24 hours before being epoxied onto the frosted side of a glass slide for thin sectioning. The Epotech epoxy was allowed to harden for 48 hours to ensure the disk adhered to the glass slide properly. The mounted disk was then cut to a thickness of 0.3-0.5 cm with an Isomet precision low-speed saw and the surface re-polished using a Hillquist grinder down to a thickness of 320-340 μm. The final polishing steps were done using silicone carbide powder on glass lapping plates and a Buehler polishing wheel removing an additional ~10-15 μm for a final thickness of ~250 μm.

A second 0.5 cm thick cross-sectional disk adjacent to the SEM disk was utilized for radiocarbon and stable isotope analyses. After measuring the diameter at multiple points the disk was separated into layers (Figure 9) using the method developed by Williams et al. (2007). Briefly, the disks were placed in 4 g of potassium hydroxide (KOH) solution mixed with 50 mL of Milli-Q water in order to detach individual rings from the disk (Figure 9A). Rings were labeled according to their location of the disk starting with ring, 1 as the outermost ring and the center of the disk having the highest ring number (Figure 9B). Typically 4-7 rings at 1-2 mm thick were separated during this step. The thickness of each ring was measured at multiple points around the ring and

then the rings were placed back in KOH solution for ~1 week (Figure 9C & 9D) after which individual layers ~10 µm thick were pealed from the ring using tweezers and a scalpel blade under a microscope. If the layers were not easily separating, the rings were placed in the oven for 24 hours and re-soaked in KOH solution for 1-3 days. The separated layers were rinsed in Milli-Q water in order to remove the KOH solution and dried in air or in an oven at ~60*C (Figure 9E).

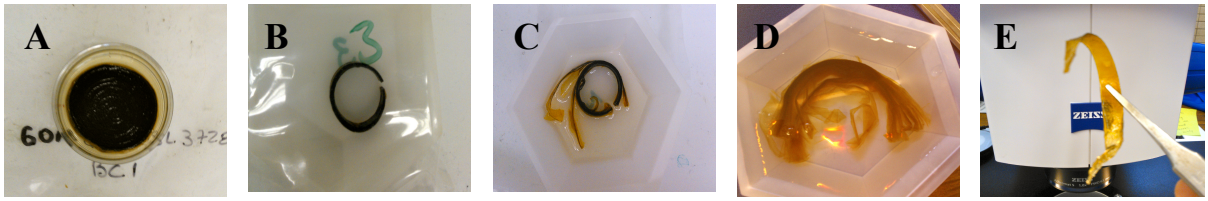

Figure 9 Radiocarbon sample preparation. A) Cross-sectional disk in KOH solution, B) Ring separated from cross-sectional disk, C) Ring separating after ~1 week of soaking in KOH solution, D) Individuals starting to separate from ring, E) Separated layer after it has been rinsed with Milli-Q water and air dried or in oven at ~60ºC.

The radial distance of each layer for both the GOM (Table 2) and SEUS (Table 3) specimens were calculated by dividing the measured thickness of the ring by the number of layers separated from the ring. This method assumes a consistent thickness for each layer but the alternative of measuring each layer, which were ~2-5 μm thick, was not possible or feasible. The thickness of each layer and radial distance for each ring were summed to arrive at a radial distance starting at the outer edge to a specific layer. The cumulative radial distances were doubled to check against the measured diameter of the disk before separations started.

Ring	# of Layers	Average Ring Thickness (μm)	Average Layer Thickness (μm)
Ring 1	93	1650	18
Ring 2	96	1720	18
Ring 3	110	1700	15
Ring 4	49	1000	20
Ring 5	172	1360	8
Ring 6 Part A	48	920	19
Ring 6 Part B	44	1008	23
Ring 7	185	3300	18

Table 2 Radial distance of the GOM specimen. Calculated radial distance for the GOM09-JSL3728-BC1 specimen. The number of layers pealed from each ring is presented with the average measured thickness. The average layer thickness was calculated by dividing the average ting thickness by the number of layers (pealed). Ring 6 has two halves (Part A and B) of the same ring.

Ring	# of Layers	Average Ring Thickness (μm)	Average Layer Thickness (μm)
Ring 1	121	923	8
Ring 2	126	890	7
Ring 3 Part A	67	883	13
Ring 3 Part B	67	796	12
Ring 4	111	1950	18
Ring 5	68	930	14
Ring 6	103	1280	12
Ring 7	109	1897	17
Ring 8	43	820	19
Ring 9	148	3120	21
Total	**963**	**13489**	

Table 3 Radial distance of the SEUS specimen. Calculated radial distance for the STET05-4904-BC1 specimen. The number of layers pealed from each ring is presented with the average measured thickness. The average layer thickness was calculated by dividing the average ting thickness by the number of layers (pealed). Ring 3 has two halves (Part A and B) of the same ring.

2.6.2 Scanning Electron Microscope Analyses

Scanning electron microscope (SEM) analyses were carried out using a Cameca SX50 electron microprobe at the Electron Microprobe Laboratory in the Department of Geology and Geophysics, Texas A&M University. Prior to analyses, ~250 μm thick thin sections were scanned in order to have optical images of the specimens to better orient and map measurement locations (Figure 10). The thin sections were then carbon coated to create a conductive layer of metal on the sample, which prevents charging, reduces thermal damage and improves the secondary electron signal.

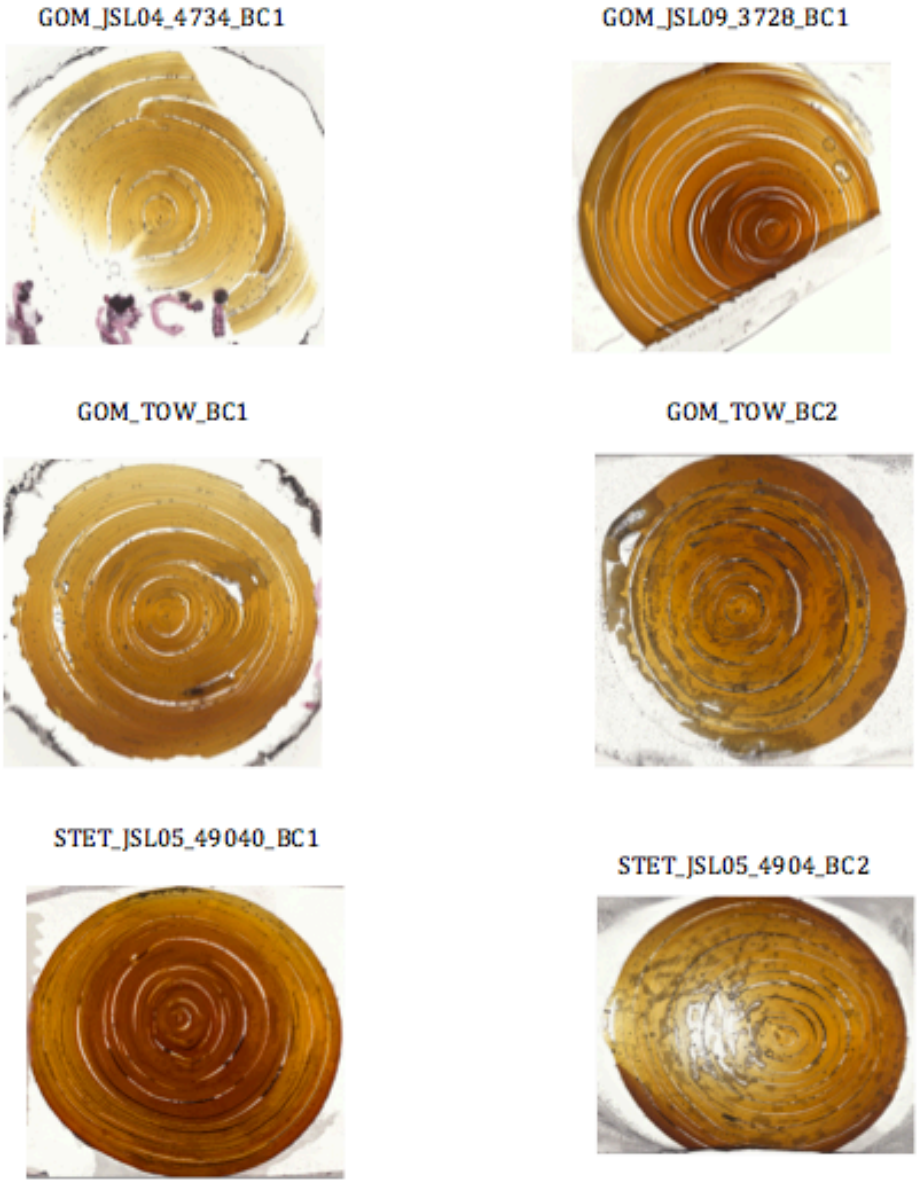

Figure 10 Scanned optical image. Six scanned optical images of polished specimens (labeled in figure).

SEM analyses included both BSE and x-ray elemental analyses of iodine and bromine. BSE are elastically rebounding electrons with high energy that produce images of surface topography and different chemical compositions. In this study, images were acquired at an accelerating voltage of 15 kV and at a beam current of 1 nA along the radial transect of the specimen. BSE image transects were run under two conditions; firstly, low magnification images were acquired at a resolution of 1024x1024 and a screen magnification of 90x (1025 μm width field view), with a 90-second acquisition time per images (Figure 11). Secondly, high magnification images were acquired at a resolution at 1024x1024 and at a screen magnification of 900x (100 μm width of field view), with a 90-second acquisition time per image (Figure 12). Three specimens were imaged by a SEM along the entire radial transect of a specimen in order to count growth bands. The remaining specimens only had 2-4 images of the most outer edge, middle, and innermost edge done to confirm the presence of bands and to correlate with the iodine and BSE measurements. The BSE measurements were correlated to the growth bands using the scar (~1 μm spot size) left behind by the electron beam from the x-ray elemental analyses along the entire radial transect, which can be seen in the BSE images (Figure 12).

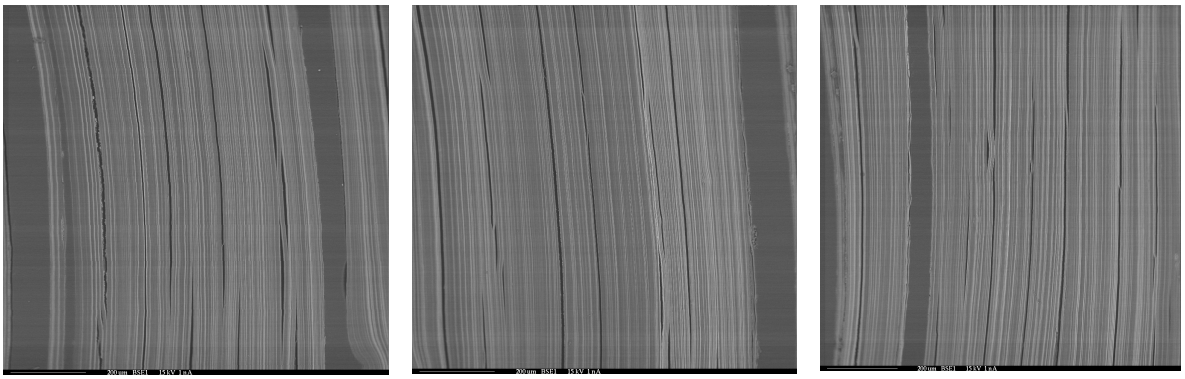

Figure 11 SEM images at 90x magnification. Examples of an SEM image at 90x magnification from the black coral *Leiopathes* sp. from the GOM. These images do not adequately resolve the grow bands in the coral's skeleton.

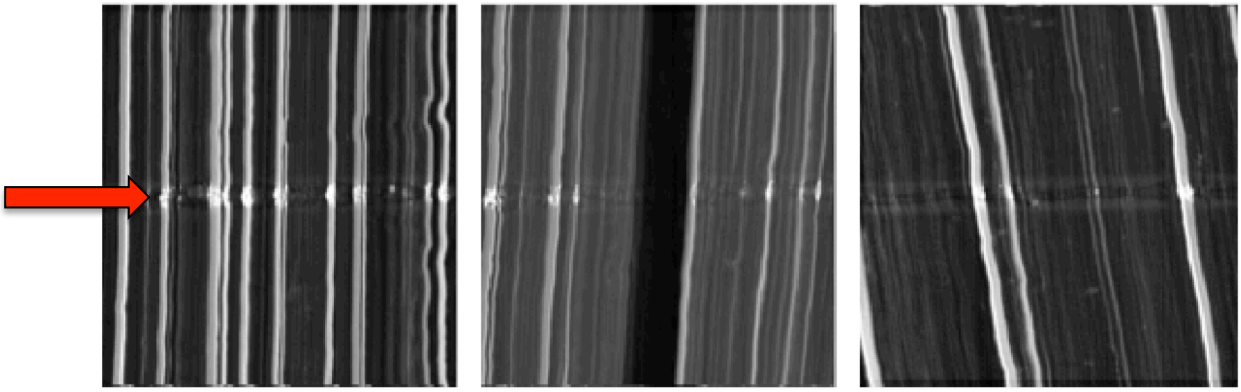

Figure 12 SEM images at 900x magnification. Examples of three different SEM images at 900x magnification that show growth bands of black coral, *Leiopathes* sp. from the GOM. Red arrow indicates the scar left from the 1 µm spot size radial transect. The width of each image is 100 µm.

X-ray elemental profiles of iodine and bromine along with BSE profiles were acquired along the radial transects of each specimen using 1-µm diameter spot beam at an accelerating voltage of 15 kV and a beam current of 20 nA. The x-ray counts were acquired using wavelength-dispersive spectrometers (WDS). Bromine profiles were acquired utilizing the Br L alpha line on 2 TAP (thallium acid phthalate) diffracting crystals. Iodine profiles were acquired using the I L alpha line on 2 PET (pentaerythritol) diffracting crystals. Starting from the center to the outer edge of each thin section, samples were measured beneath the fixed electron beam using a 1-µm spot measurements of shoulder-to-shoulder increments with 2-seconds of acquisition time at each point. BSE, iodine, and bromine were measured from the center to the outer edge of each thin section. In order for the spot size to remain constant, the surface of the specimen must remain within the same focal plane; however, some specimen experienced lifting or bubbling of the coral, which effectively increased the spot size. While every possible effort was made to identify and avoid such problem, it was not always possible. Thus, some measurements may have been made with larger spot sizes.

2.6.3 Visual Ring Counts

Visual growth bands were identified and counted from both the 90x and 900x magnification BSE-SEM images, however the 90x magnification images did not adequately resolve the visual growth bands while the 900x magnification images clearly resolved in very good detail all the visual growth bands (Figure 11 and 12). Transects across the entire radius of three specimens were made using the 100-µm wide 900x

BSE-SEM images stepped across the thin section with 10% overlap on each successive image (Table 4). These transects were used to count growth bands and to compare to spot analyses of BSE, iodine, and bromine counts. The rest of the coral specimens only had ten images taken from the center, middle, and outermost portion of the thin section in order to verify the presence of growth bands and their potential association with BSE, iodine, and bromine spot measurements.

Sample ID	Distance (μm)	# Of Images
GOM-JSL04-4734-BC1	9879	107
GOM-JSL09-3728-BC1	14838	150
GOM-TOW-BC1	7869	87

Table 4 Total number of SEM images for the entire radial transect of the GOM specimens. Black corals *Leiopathes* sp. from the GOM that had SEM images for the inter radial transect. Total number of images per specimen is listed along with the total radial distances associated with each

Independent observers who were not experts in growth band counting were instructed to count the number of growth bands in each of the 100-µm wide 900x SEM images across the entire radial transect of a specimen. The number of growth bands counted in each of the images was summed to calculate the total number of growth bands for the entire specimen. The observers were not informed of the radiocarbon or iodine ages in order to minimize any bias in their growth band counts.

2.6.4 Iodine and Bromine Count Measurements

Iodine and bromine counts were measured along the entire radial transects of six specimens using a 1-µm diameter beam stepped shoulder to shoulder starting from the center and ending at the outer edge of the thin section. This ensured a continuous high-resolution radial profile of iodine and bromine counts. To test the reproducibility of iodine and bromine counts within the same specimen, two radial transects were measured on a specimen from Stetson Banks in the SEUS (STET-JLS05-4904-BC1) (Figure 13). When peaks in iodine or bromine could be identified, observers who had no prior knowledge of the radiocarbon ages counted the identified iodine peaks.

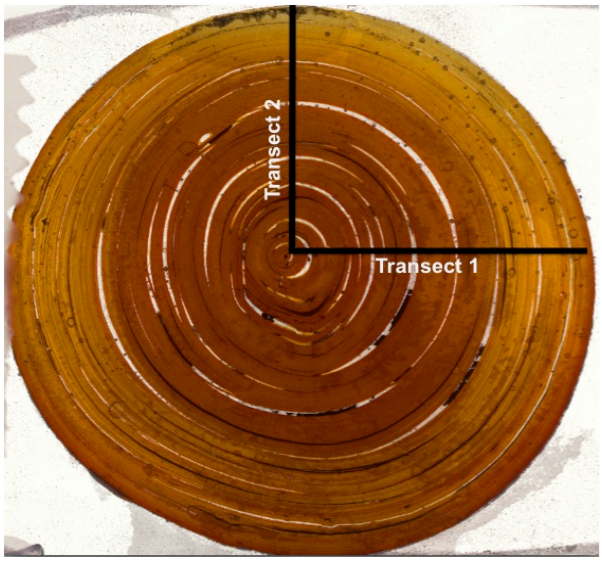

Figure 13 Two radial transects of SEM analyses. Specimen STET-JSL05-4904-BC1 from Stetson Bank SEUS showing two radial transects for iodine and bromine counts and BSE measurements.

For both the GOM (Figure 14) and SEUS (Figure 15) specimens, iodine, bromine, and BSE data points were culled if thought to correspond with desiccation cracks. These gaps were not present when the corals were collected and occurred as the specimen started to dry out as well as during the cutting and polishing phases of the thin section preparation. The desiccation cracks were identified in the iodine data by very low values. Once the gaps were removed from the iodine data, a new radial distance was calculated based on the assumption that each remaining data point represented 1 μm.

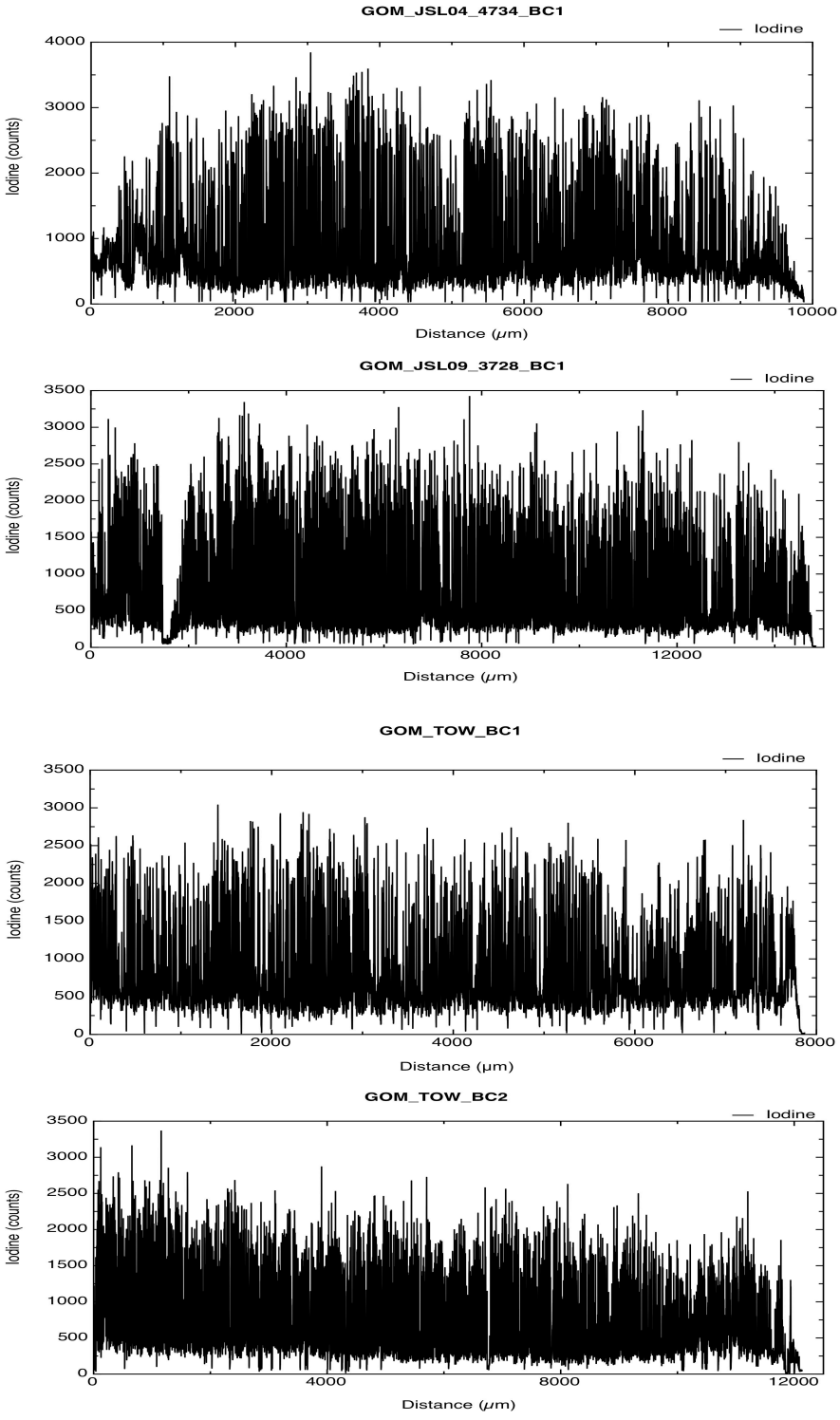

Figure 14 GOM iodine counts with radial distance. Iodine counts plotted with radial distance (μm) with gaps removed for the four specimens from the GOM.

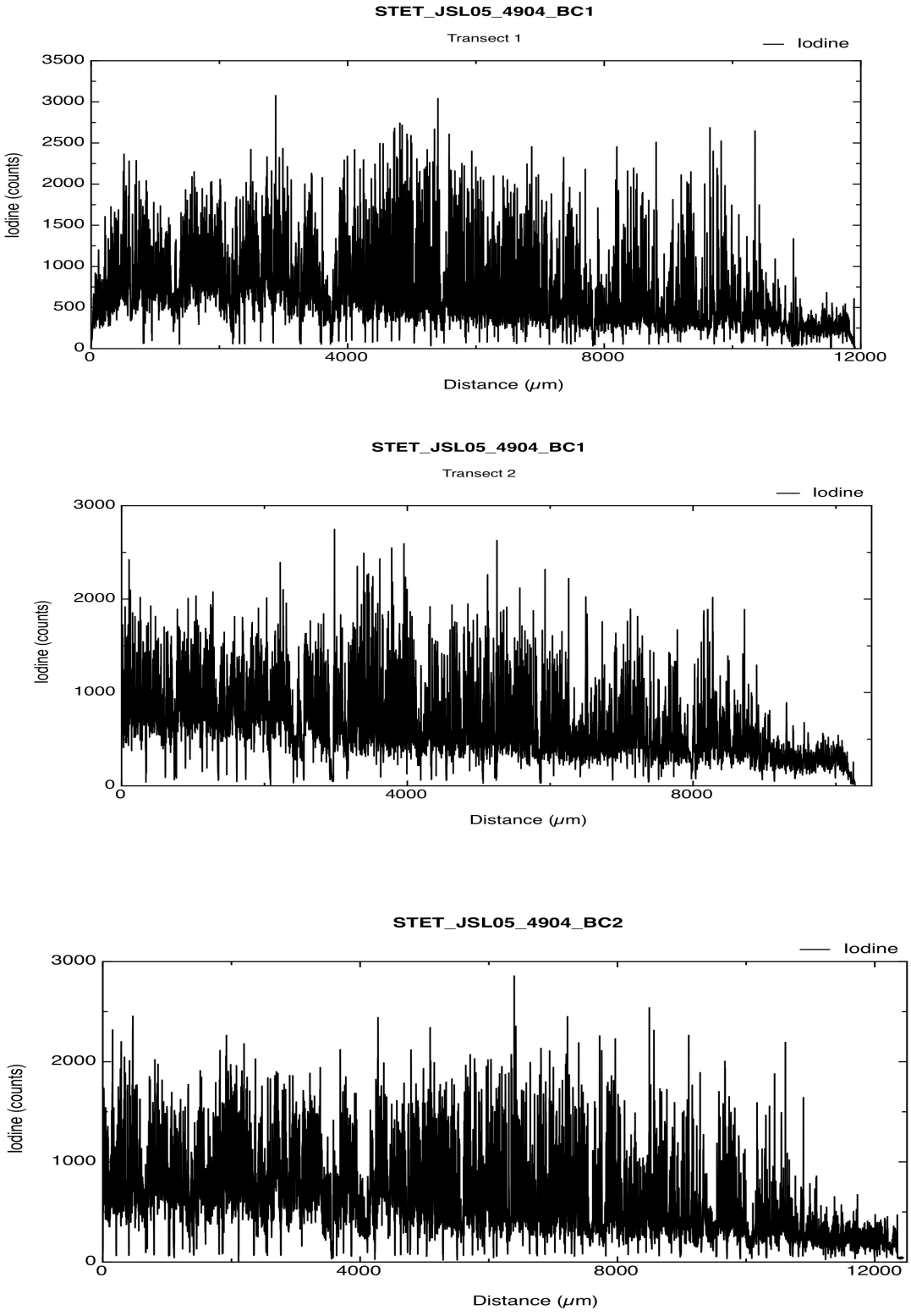

Figure 15 SEUS iodine counts with radial distance. Iodine counts plotted with radial distance (μm) with gaps removed for the specimens from the SEUS (Stetson Banks).

To easily and unambiguously identify the iodine peaks, a set of criteria was used to minimize subjectivity of what constituted an iodine peak. First, a minimum threshold of 1000 counts was utilized to identify and separate iodine peaks from the baseline noise for the GOM (Figure 16) and SEUS (Figure 17) specimens. Once the potential peaks were identified the second criteria utilized was that a second peak within 4 μm of the original peak would constitute a double peak and be counted as only one peak. The 4 μm threshold was later altered to 2 μm when it was realized that the 4 μm represented more than 50 % of the annual growth cycle in some of the slower (7 μm yr^{-1}) growing specimens and both results reported. Then the identified iodine peaks were counted to acquire the life spans for each coral. The growth rates are then calculated by dividing the total radial distance (μm) by the life span.

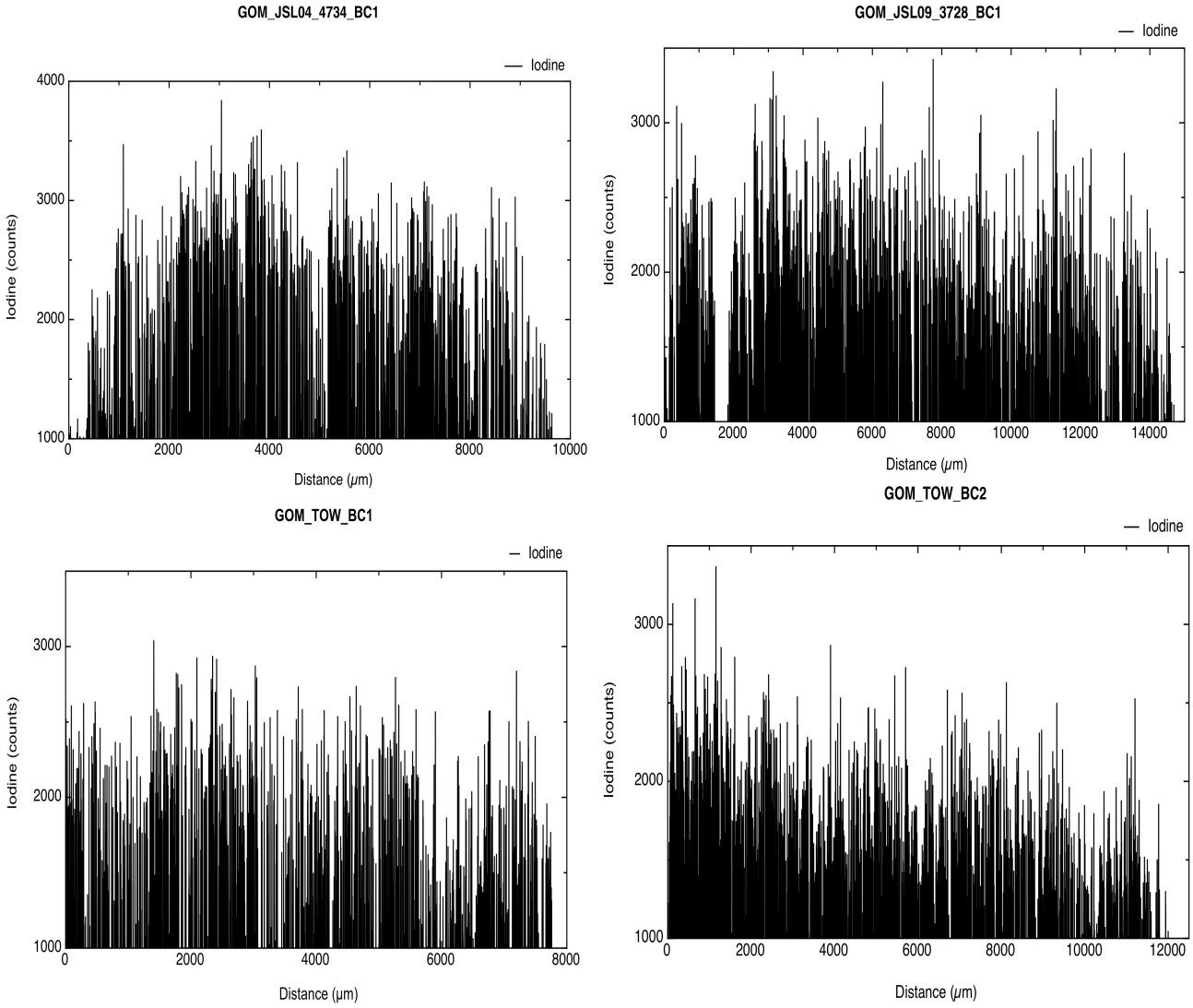

Figure 16 Iodine counts with threshold for GOM. Iodine measurements after a threshold of 1000 were implemented to remove the baseline noise for the black coral specimens from the GOM.

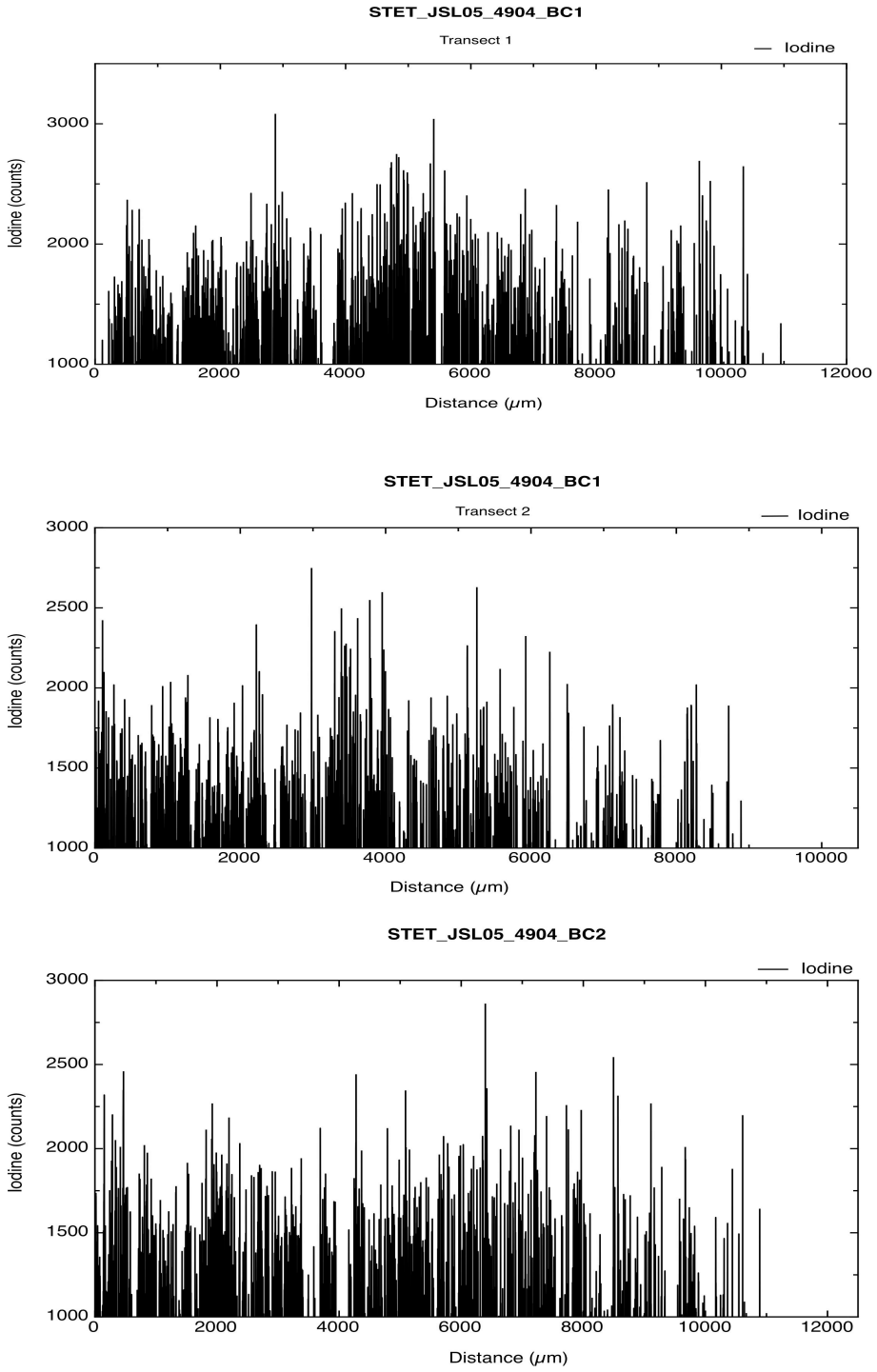

Figure 17 Iodine counts with threshold for SEUS. Iodine measurement s after a threshold of 1000 is implemented to remove the baseline noise for the black coral specimens from the SEUS.

2.6.5 Radiocarbon Dating

Individual layers were radiocarbon dated by accelerator mass spectrometry (AMS) at the Central Accelerator Mass Spectrometry at Lawrence Livermore National Laboratory (CAMS-LLNL). Individual layers were subsampled to obtain weights between 1-4 mg. Samples were then loaded into 6 mm quartz tubes along with a small scoop of silver and 20x the sample weight of CuO. If the layers were wet from the rinsing step that occurred after pealing the layers from the rings, the sample weights were estimated and then dried in a Jouna vacuum centrifuge. The quartz tubes were put on a vacuum manifold to evacuate the atmosphere and then sealed using a hydrogen-oxygen torch. The samples were combusted in a furnace for 3.5 hours at 900°C, which oxidizes the sample and makes CO_2 gas. The amounts of CO_2 gas in the sample were measured and then hydrogen was added. The tube containing CO_2, H_2,, with Fe added was heated to 570*C to reduce CO_2 to pure carbon. The water was then removed from the purified carbon and converted to graphite. The graphite was pressed into a 115 μm deep hole in an aluminum target for analyses on an FN AMS.

The radiocarbon ages were converted to calendar ages using Calb. 7.0 2013 (http://calib.qub.ac.uk/calib/calib.html) program (Stuiver and Reimer, 1993) and the Marine13 calibration curve (Hughen et al., 2004). Radiocarbon ages were corrected for the differences between the atmospheric radiocarbon content and the local radiocarbon content of the surface ocean, also known as a "reservoir age correction" (ΔR). These calibrations include the reservoir age correction (ΔR) for marine specimens to arrive at a calendar age. The GOM had a ΔR of -30 ±26 ^{14}C years (Wagner et al., 2009). The 39

±16 ΔR values of the SEUS samples were calculated based on the average ΔR values from the Bahamas and offshore Florida Keys data set (Druffel, 1982; Lighty et al., 1982). A ^{14}C marine reservoir database (http://calib.qub.ac.uk/marine) was used to determine a reasonable reservoir age based on the type of material used to calculate the reservoir age (coral, gastropod, and bivalve) and the location in which the material was gathered.

2.7 Results

2.7.1 Visual Ring Counts

The 90x magnification images (Figure 18A) did not adequately resolve the visual growth bands while the 900x magnification images (Figure 18B) clearly resolved in very good detail all the visual growth bands. The SEM images at 900x magnification clearly show visual growth bands but lifting, bubbling, and beam spot size of the coral thin section caused ~12 to 45 of the images from each specimen to be out of focus (Figure 19 and 20). Consequently, observers were unable to properly count visual growth bands on those SEM images. Also, when there were uneven surfaces, the 1 μm spot size of the SEM beam increased (e.g. ~3 μm spot size). These issues, as stated above, increased the uncertainty and caused underestimation of the life spans. The SEM images before and after the blurred SEM images were referenced to attempt to estimate the number of growth bands that would have been visible if sampling issues had not occurred (Figure 19). Some of growth bands were still visible in the SEM images that had larger (>1 μm) beam spot size and visual ring counts were attempted, but the images before and after

were still referenced because observers knew that not all the growth bands had been clearly resolved (Figure 20).

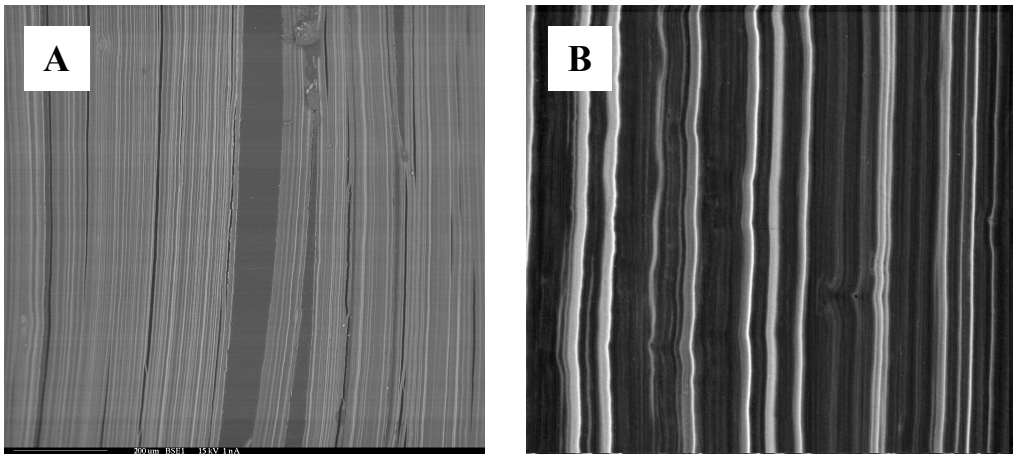

Figure 18 Comparison of SEM images of different magnifications. Comparison of the (A) 90x magnification SEM image and the (B) 900x magnification SEM image, resulting in visual growth bands being clearly resolved in the 900x magnification SEM image in good detail unlike the 90x magnification SEM image.

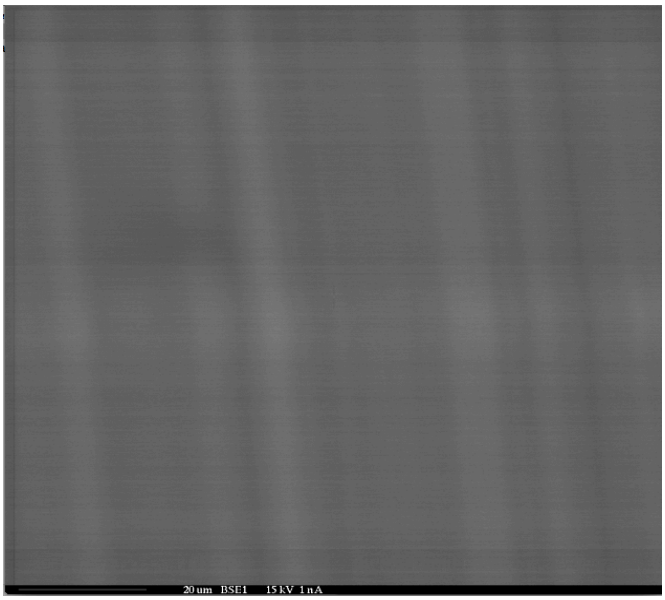

Figure 19 Blurred SEM images. SEM image at 900x magnification representing out of focuses (blurred) images due to an uneven surface of the thin section. Limiting the accuracy of properly counting the growth bands.

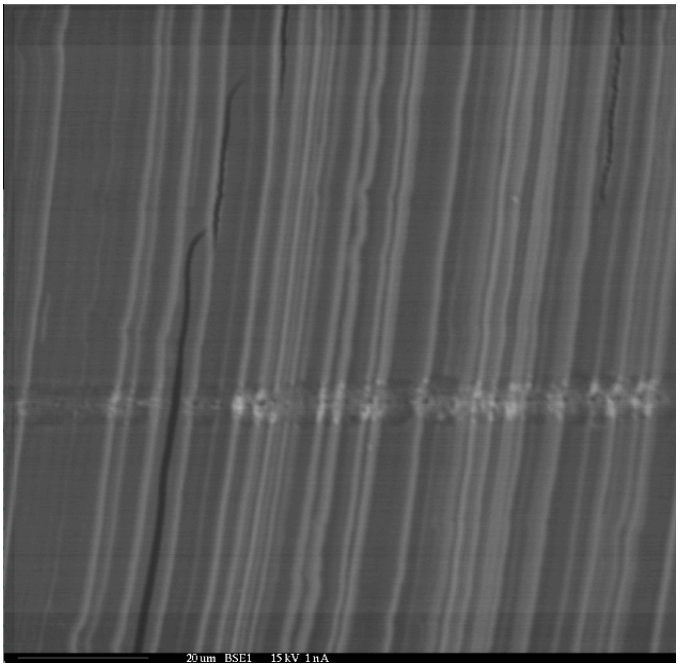

Figure 20 Out-of-focus SEM image. SEM image showing a visual growth band of a *Leiopathes* sp. (GOW-TOW-BC1) with a spot size large than 1 µm.

The results from the visual counts are presented along with the calculated growth rates for each of the specimens that had SEM images at 900x magnification for the entire radial transect (Table 5). The number of out-of-focus images were also counted and considered when conducting the ring count dating method. The visual growth band counts from the GOM specimens resulted in a life span ranging from ~490 ±50 to 1315 ±130 years and growth rates ranging 11 ±1 to 16 ±2 μm yr^{-1}. The SEUS specimen only had ten SEM images (900x magnification) at the outer most edge, the midpoint between the outer edge and the center, and at the center of the thin section for validation purposes only.

Sample ID	Life Span (yr.)	Growth Rates (μm yr^{-1})	Total # of Out-of-Focus SEM Images (900x)
GOM-JSL04-4734-BC1	785 ± 80	13 ± 2	17
GOM-JSL09-3728-BC1	1315 ± 130	11 ± 3	45
GOM-TOW-BC1	490 ± 50	16 ± 2	12

Table 5 Visual ring count results. The life spans of the deep-sea black coral are obtained by visual counts of growth bands in SEM images (at 900X magnification) along the radius of the cross-sectional disk. Total number of out-of-focus SEM images for each of the specimen.

2.7.2 Iodine Analyses

Iodine peaks along the radial transects of six specimens were counted using two methods to correct for double peaks (counting double peaks within 4 µm versus 2 µm). The life spans ranged from 600 ±60 to 1239 ±125 years and growth rates ranging 10 ±1 to 19 ±2 µm yr^{-1}, which includes the results for both (4 µm and 2 µm) methods (Table 6). The number of peaks counted on two different radial transects from STET-JSL05-4904-BC1 was 732 ±100 and 600 ±50 years using the 4 µm method and 778 ±80 and 651 ±65 years within the 2 µm method.

Sample ID	# I Peaks	# I Peaks	Distance	Growth Rates		Threshold	Threshold
	4 µm	2 µm	(µm)	4 µm	2 µm	I	BSE
GOM-JSL04-4734-BC1	665 ±65	695 ±70	9880	15 ±2	14 ±1	1000	65
GOM-JSL09-3728-BC1	1035 ±105	1240 ±125	14840	14 ±1	12 ±1	1000	105
GOM-TOW-BC1	630 ±65	715 ±70	7870	13 ±1	11 ±1	1000	100
GOM-TOW-BC2	1150 ±115	1215 ±120	12132	11 ±1	10 ±1	1000	100
SET-JSL05-4904-BC1 (1)	730 ±75	780 ±80	11910	16 ±2	15 ±2	1000	50
SET-JSL05-4904-BC1 (2)	600 ±60	650 ±65	11600	19 ±2	18 ±2	1000	50
SET-JSL05-4904-BC2	720 ±70	780 ±80	12439	17 ±2	16 ±2	1000	127

Table 6 Results for counting iodine peaks. The life spans and growth rates have been calculated by counting the iodine peaks with a 2 µm threshold and 4 µm threshold. The BSE threshold was utilized to help identify iodine peaks. The growth rates were calculated by dividing the radial distance by the life span of each specimen from the GOM and SEUS.

2.7.3 Radiocarbon Analyses

Radiocarbon results for GOM-JSL09-3528 and STET-JSL05-4904-BC1 were analyzed as part of this project (Table 7). The remaining radiocarbon results were previously reported in Prouty et al. (2011) (Table 7). Some of the ^{14}C ages resulted in "modern" values suggesting the presence of bomb-carbon, which is a reflection of artificially produced ^{14}C from the detonation of nuclear test weapons in the atmosphere in the late 1950's and early 1960's. The peak in surface ocean ^{14}C occurs ~10 years after the atmospheric peak due to air-sea ^{14}C exchange and the decadal time delay for isotopic equilibrium.

Sample ID	^{14}C Ages (yr)	Error
GOM-JSL04-4734-BC1	1020	±30
GOM-JSL09-3728-BC1	2380 1825	±30 ±40
GOM-TOW-BC1	1080	±25
GOM-TOW-BC2	2030	±15
STET-JSL05-4904-BC1	1380	±30
STET-JSL05-4904-BC2	1000	±30

Table 7 Results of ^{14}C ages. Results of ^{14}C ages from CAMS-LLNL for the GOM and SEUS black coral (*Leiopathes* sp.*)* specimens before converting to calendar years. Radiocarbon results for GOM-JSL09-3528 and STET-JSL05-4904-BC1 were analyzed as part of this project (Table 7). The remaining radiocarbon results were previously reported in Prouty et al. (2011).

The ^{14}C age results from CAMS-LLNL were calibrated to calculate the life spans and growth rates for the GOM and SEUS (Table 8). The calibrated radiocarbon ages resulted in life spans ranging from 620 ±40 to 2040 ±40 years for the GOM specimens and 560 to 885 years for the SEUS specimens. The growth rates ranged from 7 to 14 μm yr^{-1} for the GOM and 12 ±1 μm to 17 ±1 μm yr^{-1} for the SEUS. The medium probability was used to report and calculate the life spans and growth rates for the GOM and SEUS specimens. Keeping the numerous amounts of layers in chronological order throughout the separation process is critical to calculating the correct ages and growth rates for the radiocarbon analyses and when converting radiocarbon ages to calendar years.

Plots of radial distance versus Cal yr. BP demonstrate increasing age with increasing radial distance and generally show linear growth rate in both the GOM (Figure 21 and 22) and SEUS (Figure 23) specimens. The GOM specimens had a linear correlation with R^2 values between 0.71 and 0.96. The one exception is the GOM-TOW-BC1 specimen that had a correlation coefficient of 0.47. The specimens from the SEUS had higher linear correlation with R^2 values of 0.98 and 0.93. In some of the more highly sampled specimens (GOM-JSL04-4734, GOM-TOW-BC1, and STET-JSL05-4904-BC1) there is some higher frequency variability of ~100-200 years superimposed on the linear decrease in age with distance.

Sample ID	Cal yr. BP	Median Probability (yr)	Error	Growth Rates ($\mu m\ yr^{-1}$)	Error
GOM-JSL04-4734-BC1	595-655	620	±40	14	±1
GOM-JSL09-3728-BC1	1985-2100 1340-1450	2040 1400	±40 ±30	9 7	±1 ±1
GOM-TOW-BC1	635-695	670	±35	11	±1
GOM-TOW-BC2	1590-1685	1630	±30	7	±1
STET-JSL05-4904-BC1	840-925	885	±30	12	±1
STET-JSL05-4904-BC2	520-570	560	±30	17	±1

Table 8 Calibrated radiocarbon ages with growth rates. Calibrated radiocarbon age ranges with calculated growth rates of each specimen from the GOM and SEUS. These calibrated radiocarbon ages are presented in calendar years BP (1950). The median probability is the reported value for the life spans for specimens from GOM and SEUS. Radiocarbon results for GOM-JSL09-3528 and STET-JSL05-4904-BC1 were analyzed as part of this project (Table 7). The remaining radiocarbon results were previously reported in Prouty et al. (2011).

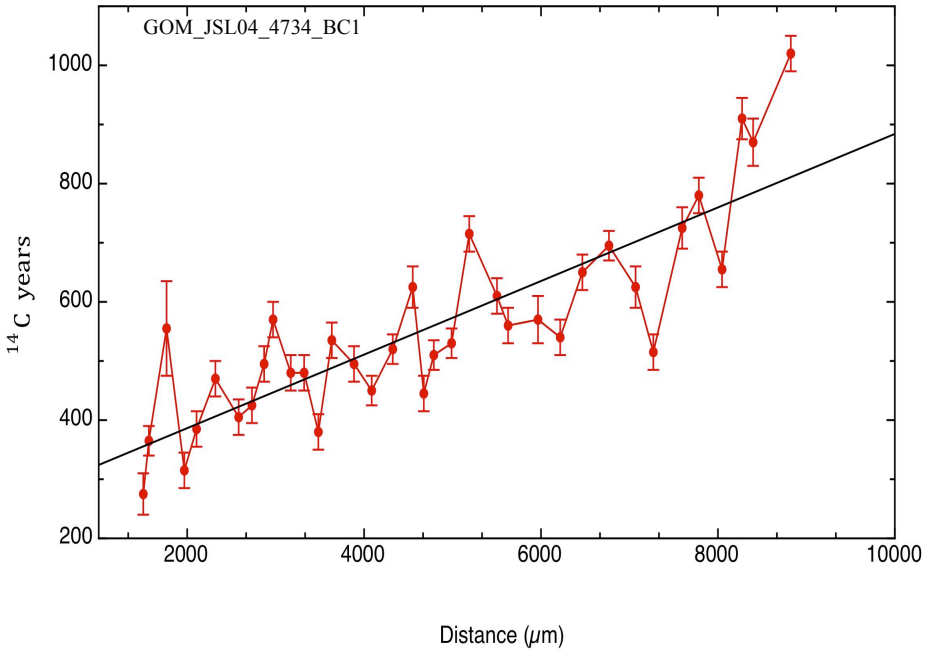

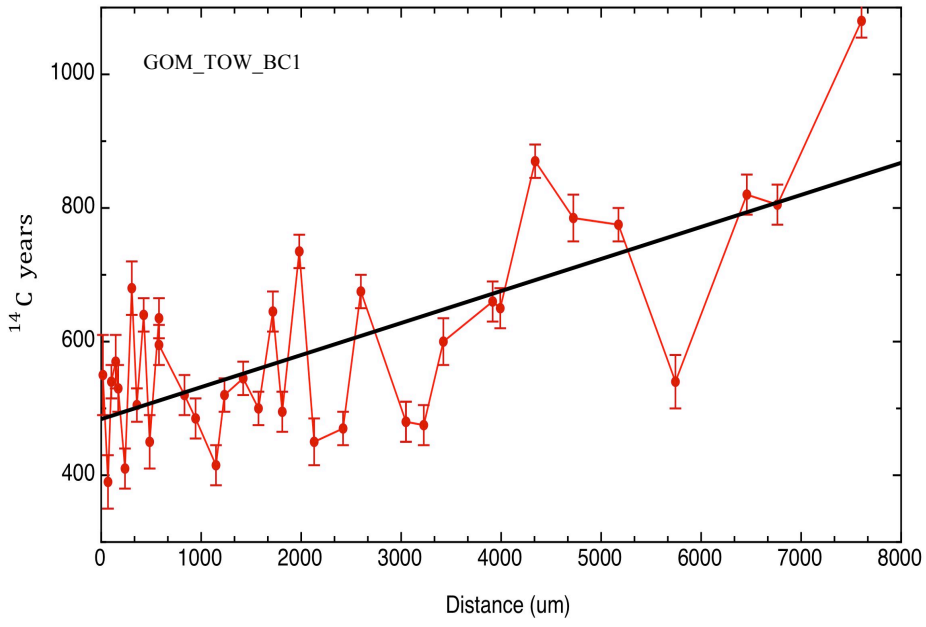

Figure 21 High-sampling resolution of calibrated ^{14}C ages with radial distance for two GOM Specimen. Radial distance (µm) vs. calibrated ^{14}C years for the GOM specimens. Showing a continuous record of variability over time.

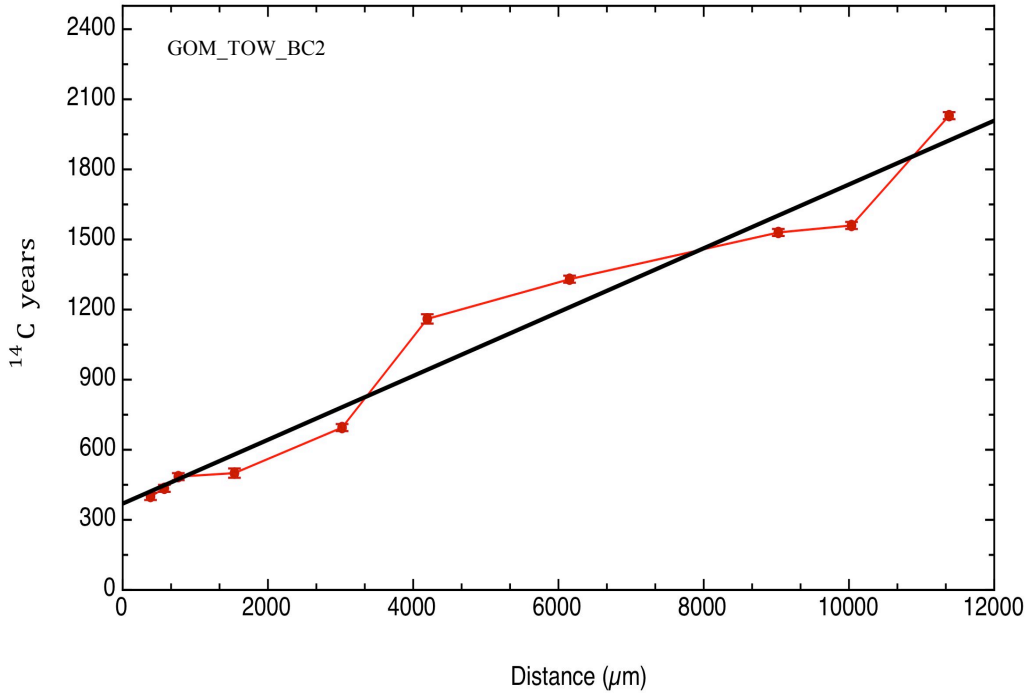

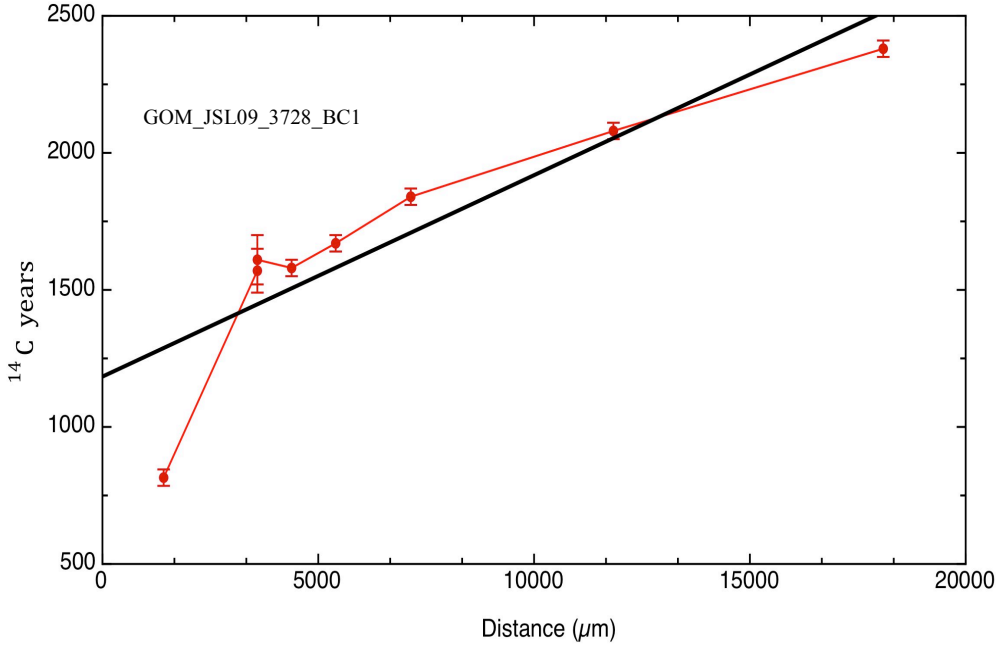

Figure 22 Low-sampling resolution of calibrated ^{14}C ages with radial distance for two GOM Specimen. Radial distance (µm) vs. calibrated ^{14}C years for the GOM specimens. Showing a continuous record of variability over time.

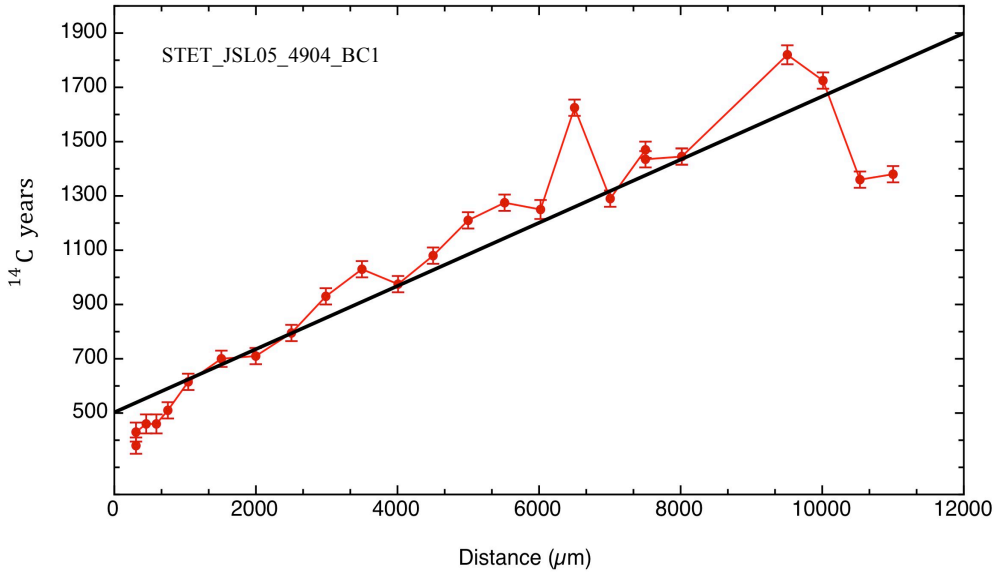

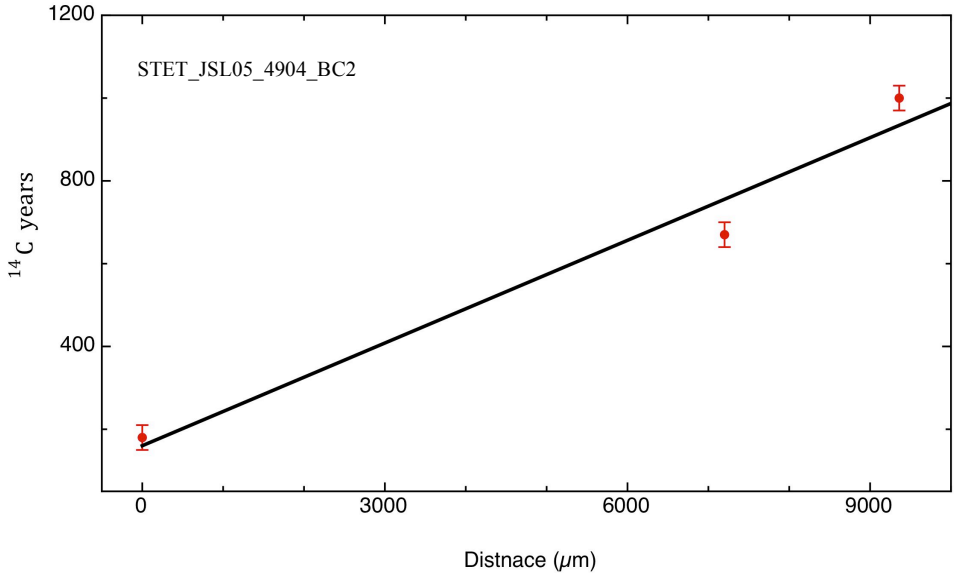

Figure 23 SEUS calibrated ^{14}C ages with radial distance. Radial distance (µm) vs. calibrated ^{14}C years for the SEUS specimens. Showing a continuous record of variability over time for the STET-JSL05-4904-BC1 and STET-JSL05-4904-BC2 having two ^{14}C ages.

2.7.4 Growth Rates and Life Spans

The results of the visual ring counts and iodine analyses were compared to the radiocarbon ages in order to validate growth bands as annual chronometers (Table 9). The ages and growth rates using the iodine dating method closely corresponded with the radiocarbon results. The visual growth band counts, on the other hand, overestimated or underestimated the ages and growth rates in comparison to the radiocarbon results. The GOM-JSL04-4734-BC1 specimen iodine and visual ring counts results best matched the radiocarbon life spans and growth rates. This sample had no indications of bubbling or lifting of the thin section and showed minimal evidence of a beam size increase because only 17 out of 107 SEM images were out-of-focus. The GOM-JSL09-3728-BC1 and GOM-TOW-BC2 specimens had iodine life spans of 360 to 480-year differences in comparison to the life spans from the radiocarbon results. There was lifting of the thin sections and uneven surface associated with both of these thin sections that could have resulted in these age discrepancies between the two different methods. GOM-JSL09-3728-BC1 also had focusing issues with the SEM images as a result of lifting of the thin sections that may have lowered the life spans and growth rates of the visual ring counts. The chronological order of the ^{14}C age from GOM-JSL09-3728-BC1 specimen was also questionable due to age reversal reported in the radiocarbon results. Also, when comparing the radiocarbon results from the GOM-JSL09-3728-BC1 specimen to Prouty et al. (2011) results, there is a life span difference of ~1000 years.

Life Spans (years)	Radiocarbon Calibrated Ages (yr)	Iodine 4 µm	Iodine 2 µm	Visual Band Counts (yr)	Average Life Spans (yr)
GOM-JSL04-4734-BC1	670 ±40	665 ±65	695 ±70	785 ±80	704
GOM-JSL09-3728-BC1	2040 ±40 1399 ±30	- 1035 ±105	- 1240 ±125	- 1315 ±130	- 1408
GOM-TOW-BC1	670 ±35	630 ±65	715 ±70	490 ±50	626
GOM-TOW-BC2	1630 ±30	1150 ±1150	1215 ±120	-	1332
SET-JSL05-4904-BC1 (1)	886 ±30	730 ±75	780 ±80	-	799
SET-JSL05-4904-BC1 (2)	886 ±30	600 ±60	650 ±65	-	712
SET-JSL05-4904-BC2	560 ±30	720 ±70	780 ±80	-	686
Growth Rates (µm)	Radiocarbon Calibrated Ages (yr)	Iodine 4 µm	Iodine 2 µm	Visual Band Counts (yr)	Average Growth Rates (µm)
GOM-JSL04-4734-BC1	14 ±1	15 ±2	14 ±1	13 ±2	14
GOM-JSL09-3728-BC1	9 ±1 7 ±1	14 ±1	12 ±1	11 ±3	12 11
GOM-TOW-BC1	11 ±1	13 ±1	11 ±1	16 ±2	13
GOM-TOW-BC2	7 ±1	11 ±1	10 ±1	-	9
SET-JSL05-4904-BC1 (1)	12 ±1	16 ±2	15 ±2	-	14
SET-JSL05-4904-BC1 (2)	12 ±1	19 ±2	18 ±2	-	16
SET-JSL05-4904-BC2	17 ±1	17 ±2	16 ±2	-	17

Table 9 Life spans and growth rates of different dating methods. The life spans and growth rates results of the visual ring counts, iodine, and radiocarbon dating methods for the specimens from the GOM and SEUS.

2.8 Discussion

2.8.1 SEM Images

The thin sections that had lifting, bubbling, or uneven surfaces caused 12 to 45 SEM image to be blurred or out-of-focus. These issues, stated above, resulted in lower life spans and growth rates along with greater uncertainties. The lifting, bubbling, and uneven surface of the thin section usually occurred after attempting to adhere the cross-sectional disk to the glass slide with Epotech epoxy. A few technique modifications might minimize or even prevent lifting, bubbling, or uneven surface of a thin section. First, properly polishing a cross-sectional disk helps create an even surface on the coral disk, which could minimize out-of-focus images and reduce the chances of beam expansion. Second, allocating enough time for the Epotech epoxy to dry (minimum of 48 hours) so that the cross-sectional disk properly adheres to the glass slide. If after 48 hours the epoxy is not completely dry, allow an extra 24 hours to dry. Putting weight to the thin section during the drying process helps prevent such complications from occurring.

2.8.2 Visual Ring Counts

The visual ring count method was conducted on three specimens by taking SEM images at 900x magnification for the entire radial distance. For each specimen, observers had no prior knowledge of the life spans or growth rates. There were variations in the counts of different observers and those variations were part of what defined the uncertainty used for the growth band counting method. For example, the GOM (GOM-

JSL04-4734-BC1) specimen had five independent observers count the SEM images for the entire radial transect and each observer ended up with different life spans (Table 10). The reason for the different reported life spans for the same specimen is because different observers can have different definitions of what is a visual growth band. Here (Figure 24) one observer can count 9 (gold stars) visual growth bands, but a second observer can count 12 (adding the red stars) visual growth bands using the same SEM image. By taking the average of the results from the five observers helps limit observational bias.

Observer	Visual Growth Bands Counted	Average Visual Growth Band Count
1	793	**783**
2	778	
3	781	
4	778	
5	783	

Table 10 Visual ring counts of different observers. Visual growth band counts from 5 independent observers for the entire radial transect of GOM-JLS04-4734-BC1 utilizing SEM images at 900x magnification.

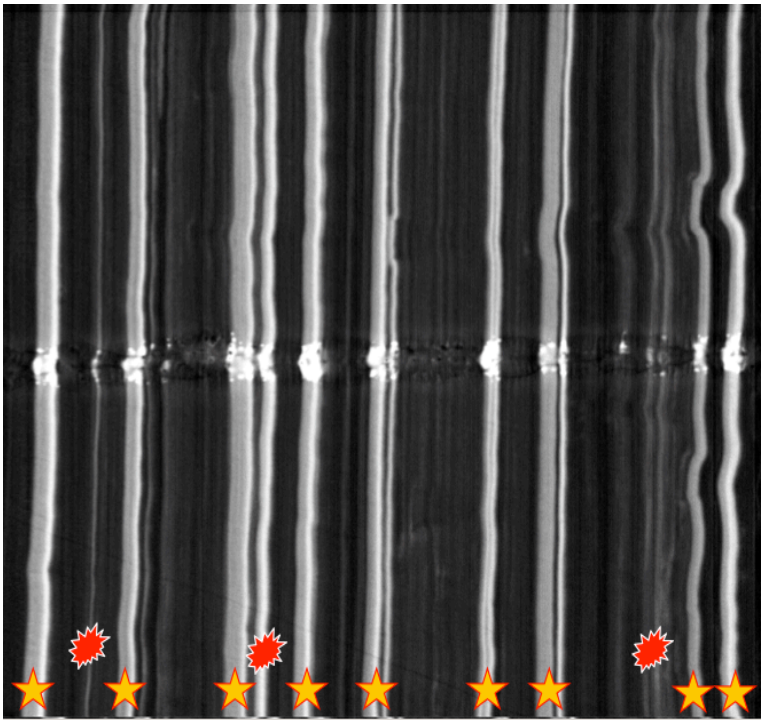

Figure 24 Visual ring counts utilizing SEM images. SEM image (GOM-JSL04-4734-BC1) at 900x magnification representing the subjective side of the visual ring count method. Observer 1 counting the gold stars and the second observer adding the red stars results in different ring counts for the same 100 µm wide SEM image.

2.8.3 Growth Band Formation

Growth bands in coral skeletons have been correlated with age (Grigg, 1976), but little is known about the mechanisms and timing of growth band formation. It has been proposed that the formation of the skeletal growth bands is due to annual variations in food supply (POC and plankton) and/or surface water productivity (Sherwood, 2002; Roark et al., 2006). Grigg (2001) suggested the coral's growth rings could be defined by the alternation of darker organic layers followed by lighter layers. Later studies found that the darker bands represent organic cement layers that serve to "glue" (known as the gluing zone) the growth laminae together (Goldberg, 1991; Nowak et al., 2009).

High iodine concentrations have been noted in antipatharian corals as early as the 1960's and 1970's (Roche et al., 1963; Goldberg, 1978). According to a recent study, the presence of iodine (and to a less extent bromine) was expected since black corals selectively collect both these elements from seawater (Nowak et al., 2009). Goldberg (1978) reported that the amount of iodine present in *Gorgonian* and *Antipathe*s corals accounted for over 23% of the skeletal weight and >94% of all the halogens in the basal portion. Nowak et al. (2009) found high concentrations of iodine in the organic cement layers in the coral skeleton of a black coral. The iodine levels are variable, with an increase in the tip in comparison with the basal portion of the coral (Nowak et al., 2009), but do not affect the results of samples taken from only the basal portion of the coral skeleton. The Nowak et al. (2009) results were the impetus for looking at iodine associated with the growth in this study, yet there is still no detailed explanation of why

the coral is preferentially depositing more iodine in association with the visual growth bands.

2.8.4 Iodine Analyses Evaluation

The iodine peaks along with the BSE measurements correlate very well with the growth bands seen in the SEM images (Figure 25). When two peaks are identified in the iodine and BSE measurements within 2-4 μm, they are classified as a double peak. Observers were told to count double peaks (red arrow) as only one peak when counting the visual growth bands (Figure 25). The good correspondence between the iodine and BSE measurements with the visual growth bands suggests that growth bands can be counted to determine the age of a specimen and develop a chronology assuming they are deposited on an annual basis, which is only true if the methods agree with the radiocarbon method.

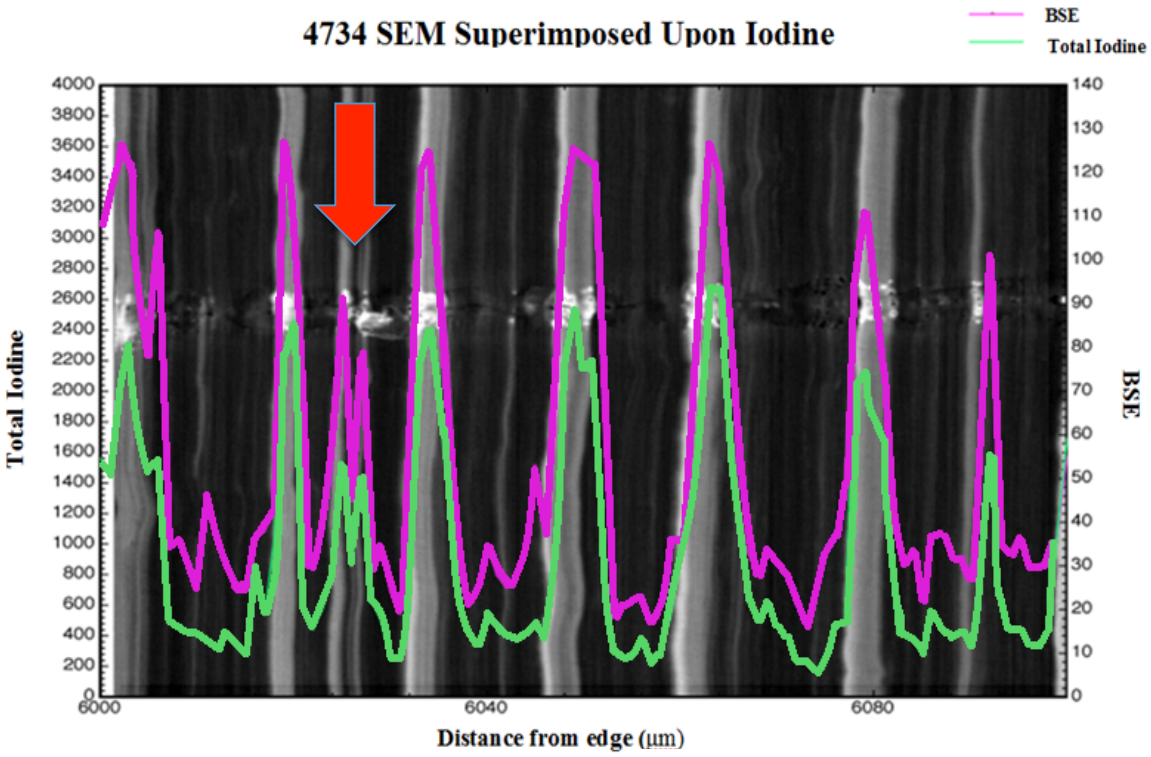

Figure 25 Iodine and BSE counts overlaid on SEM image. SEM image from GOM-JSL04-4734-BC1 at 900x magnifications. The iodine counts overlay the SEM image to valid the correlation of the iodine peaks to visual growth bands.

The iodine method is less subjective than the visual ring count method and there were some limitations and challenges that needed to be addressed. For example, the selection of a baseline threshold might influence results. Use of a baseline threshold of 800 counts on some specimens yielded no significant differences in life span compared with the 1000 counts threshold. The second criteria, which identified a second peak within 4 μm of the original peak as double peak, was altered to 2 μm when it was realized that 4 μm was more than 50% of the annual growth cycle in some of the slower (7 μm yr^{-1}) growing specimens. The change in threshold from 4 μm to 2 μm resulted in a 5% to 20% increase in the life spans of these corals. Even with the two results in life spans from the 2 μm and the 4 μm threshold, both iodine and BSE were counted and correlated with the growth bands. The results from both (2 and 4 μm) thresholds resulted in good agreement with the visual counts and ^{14}C ages. The 2 μm threshold, however, had the best match in life spans and growth rates with the visual growth band counts and ^{14}C ages. This suggests that iodine can be used as a dating method to determine the ages and growth band of deep-sea black coral (*Leiopathes* sp.) from the GOM and SEUS.

There were also a few unique signals from the SEUS iodine measurements, which indicate very low amounts of iodine towards the center of the thin sections. These low measurements may represent a decrease in iodine (or food source) uptake due to the size of the coral at a young age. The second possibility is a reproducible environmental impact signal being documented (e.g. shift in the Gulf Stream). Further research will be required to explain decrease in iodine counts from the SEUS specimen.

2.8.5 Radiocarbon Comparisons

Radiocarbon dates were previously published by Prouty et al. (2011) for GOM-JLS04-4734-BC1, GOM-TOW-BC1, and GOM-TOW-BC2. The remaining specimens, including GOM-JLS09-3728-BC1, STET-JSL05-4904-BC1, and STET-JSL05-4904-BC2, were measured at CAMS-LLNL as part of this study. The GOM-JLS09-3728-BC1 specimen had a life span of 1400 ±30 Cal yr. BP and a growth rate of 7 ±1 μm yr^{-1}. The STET-JSL05-4904-BC1 specimen resulted in a life span of 885 ±30 Cal yr. BP with a growth rate of 12 μm yr^{-1}. The STET-JSL05-4904-BC2 resulted in a life span of 560 ±15 Cal yr. BP and growth rate of 17 μm yr^{-1}. Prouty et al. (2011) reported life spans and growth bands for a few of the same specimens used for this project (Table 10).

For the GOM-JLS09-3728-BC1 specimen, Prouty et al. (2011) used the same specimen and reported a life span of 2040 ±40 Cal yr. BP and a growth rate of 9 ±1 μm yr^{-1}, compared with 1400 ±30 and a growth rate of 9 ±1 μm yr^{-1}, respectively. The rest of the results from Prouty et al. (2011) reported life spans of specimen from the GOM ranging 620 ±40 to 1630 ±30 Cal yr. BP with growth rates ranging from 8 to 22 μm yr^{-1}. Another study radiocarbon dated a black coral (*Leiopathes* sp.) from 450 m depths off Hawaii, resulting in a life span of ~2377 years with a growth rate of ~5 μm yr^{-1} (Roark et al., 2009). Compared with previous studies, this project obtained lower life spans for both GOM and SEUS specimens, which I suggest is a result of regional differences in food supply and nutrient availability.

The GOM-JLS09-3728-BC1 specimens from the GOM were not used for further interpretations due to the radiocarbon data showing age reversals and having extremely

young ages towards the center of the specimen. A previous study also found difficulties in band peeling, reporting horizontal offsets (Williams et al., 2007). These unexplained radiocarbon ages could reflect changes in ocean circulation, ocean seeps, or human error, which includes mislabeling or sample mix-up during the preparation process. Ultimately the GOM-JLS09-3728-BC1was excluded due to the possibility of human error because it was noted in the lab notes that multi layers had separated from the same ring and tracking correct chronological order of these rings was difficult.

2.8.6 Life Spans and Growth Rates Comparisons

The life spans and growth rates have been calculated using visual ring counts, radiocarbon, and the iodine dating methods. Both the iodine and the visual ring count dating methods were evaluated based on how well they compared to the radiocarbon results for both the GOM (Figure 26) and SEUS (Figure 27) specimens.

For the GOM, the life spans (blue) and growth rates (red) for iodine (using both the 2 μm and 4 μm thresholds) matched more closely to the radiocarbon results than the visual ring counts (Figure 26). The visual ring counts seem to overestimate (GOM-JSL04-4734-BC1) or under estimate (GOM-TOW-BC1) the life spans for the GOM specimens. Visual ring counts for GOM-TOW-BC2 were not reported because SEM images for the entire radial transect were not acquired, only the inner, middle, and outer portion of the thin section was imaged for verification purposes only. The iodine life spans and growth rates corresponded well with the radiocarbon results using both 2 μm and 4 μm thresholds.

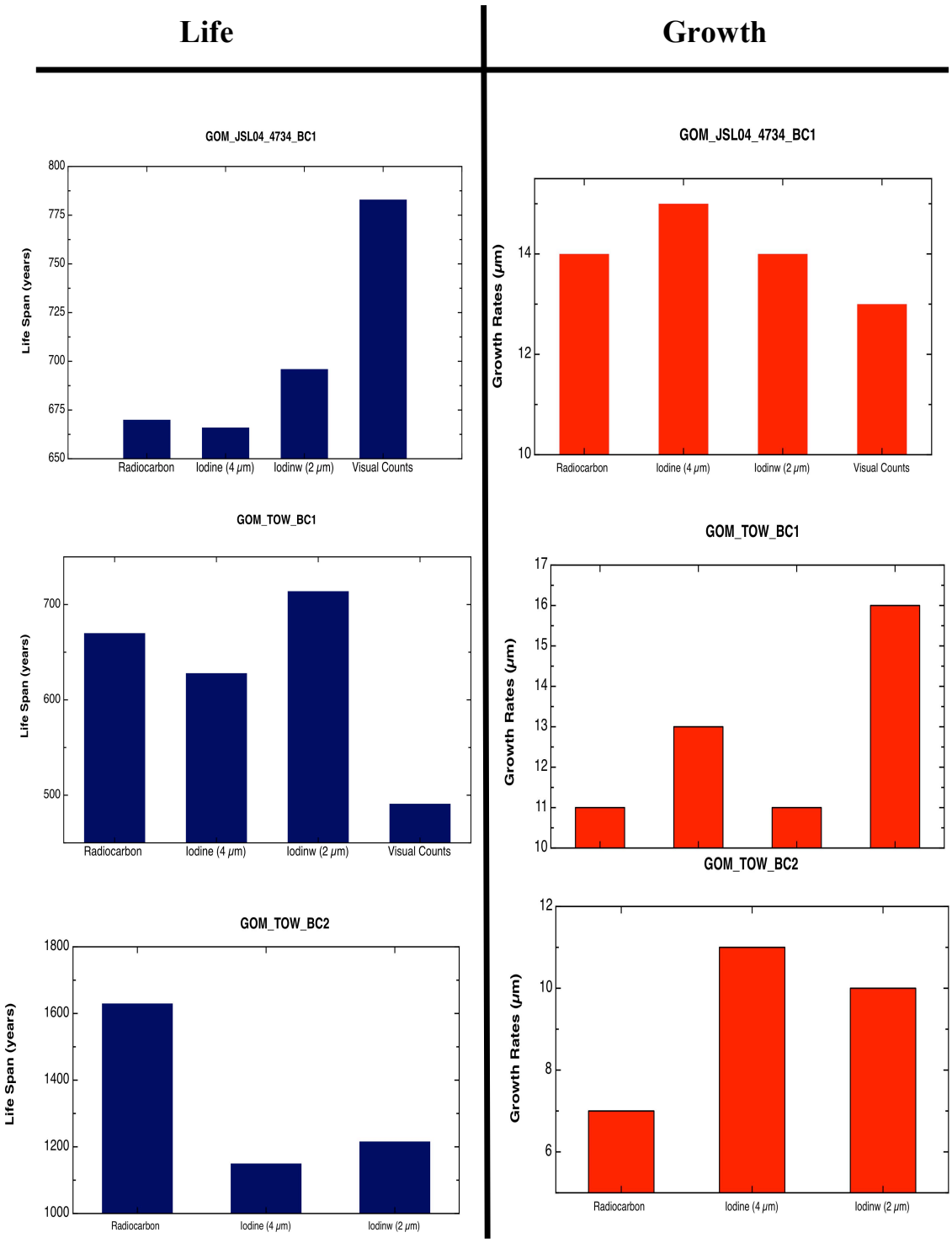

Figure 26 Comparison of life spans and growth rates for GOM. The life spans and growth rates for specimens from the GOM are compared using the different dating methods (radiocarbon, iodine analyses, and visual ring counts). The GOM-JSL09-3728-BC1 is excluded and visual ring counts were not conducted for GOW-TOW-BC2.

The SUES specimens did not have any visual ring counts since SEM images were not taken for the entire radial transect of the thin sections, only ten images at three different spots (outer edge, middle, and center) were obtained for validation purposes only. STET-JSL05-4904-BC1 did, however, have two radial transects measured to determine reproducibility of iodine and BSE measurements within the same specimen. Life spans and growth rates using the 4 μm versus 2 μm double-peak threshold were compared to the radiocarbon results while also comparing the two radial transects from the same specimen.

First, two radial transects for STET-JSL05-4904-BC1 were compared to determine reproducibility of iodine within the same specimen. The radiocarbon analyses resulted in a life span of 886 ±30 years with a growth rate of 12 ±1 μm yr^{-1}. The iodine life spans for transect 1 resulted in 732 ±75 years for the 4 μm threshold and 778 ±80 years for the 2 μm threshold. Transect 2 resulted in life spans of 600 ±60 years for the 4 μm threshold and 651 ±65 years for the 2 μm. The life spans for the two radial transect results were reproducible within the margin of error for the same specimen. The life span from radial transect 1 with the 2 μm threshold was the only one that corresponded to the radiocarbon results within the margin of error. Second, the outcomes of the life spans and growth rates using 4 μm versus 2 μm thresholds were compared. The results (life-spans and growth rates) from STET-JSL05-4904-BC1 for both transect 1 and 2, showed that the 2 μm threshold matched the radiocarbon result more closely than the 4 μm threshold (Figure 27). STET-JLS05-4904-BC1, on the other hand, had a better agreement with the 4 μm threshold when compared to radiocarbon results (Figure 27).

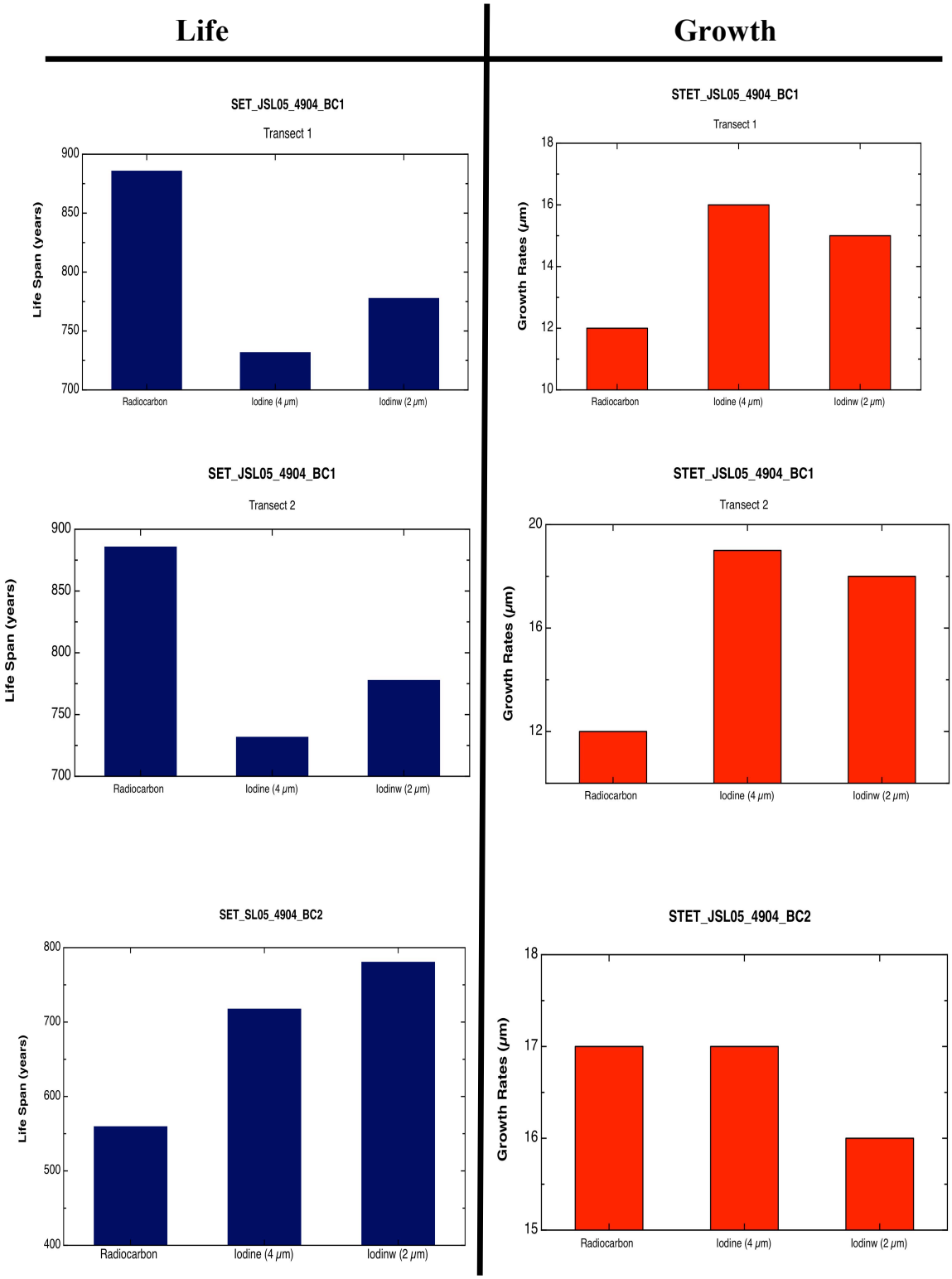

Figure 27 Comparison of life spans and growth rates for SEUS. The life spans (years) and growth rates for each specimen from the SEUS are compared using the different dating methods (radiocarbon, iodine analyses, and visual ring counts).

Iodine and BSE counts along with SEM images at 900x magnification match the radiocarbon derived ages in most cases well, such that they than can be utilized as annual chronometers. The ^{14}C ages from CAMS-LLNL had to be calibrated using a reservoir age correction. This represents a limitation of the radiocarbon dating method because the reservoir ages are not constant due to the mixing of older deep water with surface waters that have lower $\Delta^{14}C$ values or atmosphere-ocean exchanges that can give lower transient reservoir ages (Druffel et al., 2008). Having another independent dating method, such as U/Th, would benefit the project as part of the future work. Even with these limitations, there was good agreement in the life spans and growth rates for both the GOM and SEUS, making this the first study to validate growth bands and iodine peaks in deep-sea black corals as annual chronometers.

2.9 Conclusion

Deep-sea corals are only beginning to be used as paleoclimate archives that can extend our observation of ocean dynamics and climate well beyond the onset of instrumental records. This is important because in order to see climate variations and changes in ocean processes, high-resolution decadally resolved long-term records are needed. Iodine analyses can be used as an independent dating method if good quality thin sections are made before analyses are conducted, and the growth rates are taken into consideration. This is the first time iodine analyses have been used to validate the annual growth bands of any DSC. The limitations of the iodine dating method occur when placing thresholds on iodine count data sets to identify iodine peaks. In the GOM, the

threshold of 2 μm and 4 μm for counting double-peaks as one both had consistent agreement with the radiocarbon results, but the 2 μm threshold resulted in life spans in better agreement with the radiocarbon derived life spans. For the SEUS, using a threshold of 1000 for iodine peaks ended up removing a reproducible signal of lower (<1000) iodine counts toward the outmost edge of the specimens. Further research is required to explain these low iodine counts toward the center of Stetson Banks' specimen.

In conclusion, the new iodine dating method with visual ring counts from SEM images validated annual growth banding in deep-sea black coral *Leiopathes* sp. from the GOM and SEUS. Using the independent age models in conjunction with the radiocarbon records, calculated ocean ventilation records can be developed. Ocean reservoir ages can be used to study past changes in ocean circulation in the Gulf of Mexico and SEUS.

CHAPTER III

DETERMINING OCEAN RESERVOIR AGES IN DEEP-SEA BLACK CORALS

3.1 Introduction

Coral skeletons provide one of the few archives of past seawater $\Delta^{14}C$ variations, since their carbonate skeletons are derived from ambient dissolved inorganic carbon (DIC) at depth. By projecting paleo-$\Delta^{14}C$ values back in time to their intersection with atmospheric records, the residence time, or reservoir age, of different water masses can be calculated. A reservoir age arises from an offset between the ^{14}C compositions of surface ocean DIC and the atmosphere (Druffel el al., 2008; Komugabe et al., 2013). Past reservoir ages measured in corals are typically derived from the differences between the radiocarbon age of corals and the radiocarbon age of the contemporaneous atmosphere (Komugabe et al., 2013). These reservoir ages are maintained mainly by mixing with deeper waters that have older ^{14}C ages because of ^{14}C decay in the ocean interior, which is isolated from exchanging CO_2 and thus radiocarbon with the atmosphere (Druffel et al., 2008).

The global average difference between the surface ocean and the atmosphere is 400 years. The delay in exchange between atmospheric CO_2, and ocean DIC, as well as the mixing of surface waters with upwelled old deep waters cause this apparent older age of oceanic surface waters. It is therefore necessary to apply a correction in order to compare the radiocarbon ages of marine and terrestrial samples. This correction is known as the marine reservoir age, R (Stuiver et al., 1986), and is the difference in years

between the measured ^{14}C age of marine organism's carbonate shell and the atmospheric ^{14}C age at the time as reported in the terrestrial calibration curve (Reimer et al., 2004). A regional correction, designated as ΔR (Stuiver and Braziunas, 1993), is needed to adjust for the difference between the regional reservoir ages and the nominal average global marine reservoir age for surface ocean waters, e.g. 400 years (Oeschger et al., 1975). Knowledge of regional ΔR values is required to accurately calibrate ^{14}C ages derived from marine samples. Typically reservoir ^{14}C ages and ΔR correction values are based on modern ocean circulation patterns since they are calculated from samples collected in the last century. When calibrating the ^{14}C ages for the development of a chronology in a marine archive, one assumption is that the reservoir ages do not change. Typically this assumption is violated due to a number of reasons including changing amounts of ^{14}C stored in different Earth systems such as the ocean and atmosphere, resulting in one of the limitations of ^{14}C chronologies.

The global average reservoir age is ~400 years but Stuiver et al. (1986) reported reservoir ages in nonpolar surface regions determined by shells, corals, and seawater DIC ranged from ~300 to 670 years. Lower reservoir ages were discovered in the mid-gyre regions of the ocean where downwelling is dominant, and higher reservoir ages were found in areas of upwelling (e.g. equator and eastern boundary currents) (Druffel et al., 2008). The average reservoir age for surface ocean DIC in the Florida Straits is 390 ±60 years over the last few centuries, determined using tree ring and coral growth bands from the Florida Keys and Belize (Druffel, 1980; Druffel and Linick, 1978; Stuiver and Quay, 1980). Little information is available regarding how the reservoir ages of the

surface oceans have changed prior to A.D. 1600 because of the challenges involved in obtaining pristine carbonated (corals, shells) that can be age dated (Druffel et al., 2008).

With the development of independent chronologies, radiocarbon measurements in marine archives, typically corals and shells, can be used as a tracer of changing ocean dynamics. Kilbourne et al. (2007) suggested that a muilti-decadal record were needed to resolve interannual to decadal time scales of water-mass tracers that integrated high frequency variability, such as eddies and tides. This was supported by Komugabe et al. (2013), which stated that improvements of marine radiocarbon (^{14}C) chronologies were needed to better understand and constrain paleoceanographic processes. Offshore from La Parguera, Puerto Rico the head of a *Montastraea favolata* coral was utilized and the growth bands found in the coral's skeleton, assumed to be annual, were counted to developed an independent chronology combined with radiocarbon analyses to observe ocean current variability in the northern Caribbean region (Kilbourne et al., 2007). These resulting $\Delta^{14}C$ records showed that large and relatively rapid variations indicating advection of surface water masses and/or mixing were driving most of the corals $\Delta^{14}C$ variability in this region (Kilbourne et al., 2007). Druffel et al. (2008) used U/Th to develop an independent chronology to observe reservoir ^{14}C age variability in the Florida and Caribbean region. Druffel et al. (2008) suggested several potential causes of the lower than average reservoir ages, including restricted flow between the reef and open ocean surface wasters, falling atmospheric $\Delta^{14}C$ values, or reduced mixing between the surface and subsurface waters in the open ocean due to the changes in the strength in the Yucatan Current in this region. Komugabe et al. (2013) also used U/Th, measured

from a deep-sea black coral, to develop an independent chronology to calculate the reservoir ages in the Tasman Sea and understand regional ocean circulation patterns. These results indicated lower reservoir ages after 1900 AD, which were potentially caused by variations in the lateral advection of ^{14}C-rich waters of tropical and temperate origin, or changes in ventilation of surface waters overlaying the Norfolk Ridge region due to differences in mixing with deeper ^{14}C-poor water masses (Komugabe et al., 2013). These studies demonstrate the importance of obtaining reliable independent chronologies in order to observe variability and long-term changes in ocean dynamic (e.g. ocean currents).

3.1.1 Radiocarbon Dating

Radiocarbon dating is the most common means of determining the life spans and growth rates of both calcium carbonate and proteinaceous DSC skeletons (Adkins, 1998; Sherwood et al., 2005; Prouty et al., 2011; Roark et al., 2005, 2006, 2009; Parish and Roark, 2009; Carreiro-Silva et al., 2013). The range of conventional radiocarbon dating is from modern time (defined as 1950 AD) to ~50,000 years BP and simply relies on the known radioactive decay rate of ^{14}C, measurements of ^{14}C in the sample by accelerator mass spectrometer (AMS), and knowledge of the amount of ^{14}C in the sample at the time of formation. While the principles are straightforward and the method well established, there are some limitations. For example, the atmospheric concentration of radiocarbon has varied over time (Stuiver and Braziunas, 1993; Reimer et al., 2009). Age determination in DSC using radiocarbon dating is most applicable to growth occurring

over centuries to millennia for living specimens, and extends into fossil specimens in the 10's of thousands of years (Guilderson et al., 2005).

A second form of radiocarbon dating for DSC, involves the identification of the anthropogenic bomb-radiocarbon signal due to testing of thermonuclear devices in the 1950's and 1960's. This is sometimes referred to as the bomb-radiocarbon dating method (Roark et al., 2005; Sherwood et al., 2005). The bomb radiocarbon results in a sharp increase in atmospheric ^{14}C starting in the late 1950's, peaking in ~1965, and gradually declining since then. In the surface ocean the bomb curve is typically represented by increasing ^{14}C in the early 1960's, peaking in the 1970's, then gradually decreasing. The timing and progression of these inflection points can be used to determine ages in marine organisms where the bomb curve can be reconstructed (Figure 28). Due in part to ocean circulation mixing times, downwelling, and upwelling, there are regional differences in the timing of these inflection points that require the use of a local bomb curve. For example, this has been done by measuring ^{14}C in otoliths of known age (Baker and Wilson, 2001) and in coral records with independent chronologies (typically seasonal variations in $\delta^{18}O$ or Sr /Ca that reflect sea surface temperature (SST)) (Wagner et al., 2009).

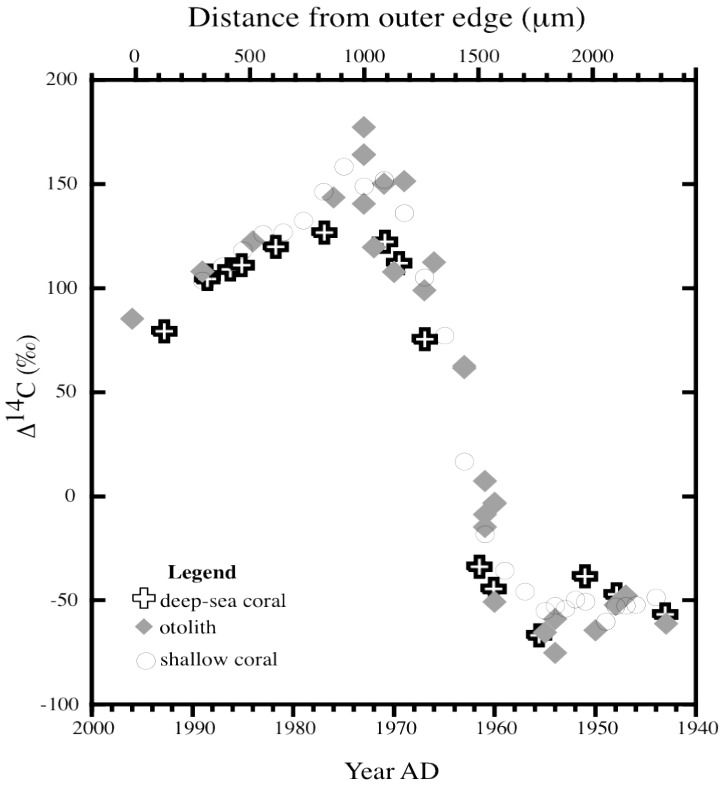

Figure 28 Bomb-radiocarbon signal. The radiocarbon spike that represents the nuclear testing in the late 1950's, peaking in ~1965 (Prouty et al. 2001). Shown are bomb-derived $\Delta^{14}C$ (‰) from red snapper otoliths (n=26) in the Gulf of Mexico (Baker and Wilson, 2001) and shallow coral $\Delta^{14}C$ values (n=27) from the Flower Garden Banks (Wagner, et al., 2009) from 1943-1996. Superimposed on the reference curves is the deep-sea coral $\Delta^{14}C$ record from the GOM-JSL04-4734-BC1 specimen versus distance from outer edge (μm).

Either method will provide reliable estimates of the calendar ages and growth rates of marine specimens. Reconstructing the bomb curve also proves that DSC with proteinaceous skeletons are getting their carbon from POM that falls from the surface (Roark et al., 2005, 2006, 2009; Prouty et al., 2011). An earlier study in the GOM suggested that these DSC were in part feeding on a food chain supported by chemosynthetic bacteria that is reliant on gas seeps (Hovland, 1990). This was proven incorrect based on studies showing similarities between the surface water $\Delta^{14}C$ derived from shallow-water coral $\Delta^{14}C$ records and deep-sea black coral $\Delta^{14}C$ records (Roark et al., 2006, 2009; Prouty et al., 2011).

This research will utilize radiocarbon data along with the novel independent iodine chronology in deep-sea black coral, *Leiopathes* sp., developed in chapter 1, to construct a continuous record of past ocean reservoir ages over the last ~500-1000 years in the GOM and SEUS. Multiple reservoir age records will be compared to assess their reproducibility. Reservoir age records from the GOM and SEUS will also be compared to comprehend regional changes in ocean circulation.

3.2 Study Site and Samples

Black corals are long-lived, habitat-forming, sessile, benthic, suspension feeders. Black corals, or *Leiopathes* sp. are colonial cnidarians in the order Antipatharia and are found in all oceans, usually at water depths greater than 30 m deep to 6,000 m (Prouty et al., 2011; Roark et al., 2009; Nowak et al., 2009). Specimens of *Leiopathes* sp. were collected in the GOM along the continental slope and from the SEUS between 600 m

and 700 m in depth. Four of the corals were collected from the head of the De Soto Canyon and Viosca Knoll from the GOM, which are both east of the Mississippi delta. The other two were collected from Stetson Banks located in the SEUS.

3.3 Methods

3.3.1 Sample Preparation

Detailed methods are described in chapter 1, but briefly two cross sectional disks were cut from the basal-most portions of four specimens. The first disk from each specimen was mounted on a glass slide and polished to a ~250 μm thick thin sections for SEM analysis. A second 0.5 cm thick cross-sectional disk adjacent to the SEM disk was utilized for radiocarbon and stable isotope analyses. After being measured in diameter, soaked in KOH solution, and then rinsed in Milli-Q water, the radial distance of each layer for both the GOM and SEUS were calculated.

3.3.2 Scanning Electron Microscope Analysis

X-ray elemental profiles of iodine and bromine along with BSE profiles were acquired using 1-μm diameter beam at an accelerating voltage of 15 kV and at a beam current of 20 nA. The x-ray counts were acquired using wavelength-dispersive spectrometers (WDS). Bromine profiles were acquired utilizing the Br L alpha line on 2 TAP (thallium acid phthalate) diffracting crystals. Iodine profiles were acquired using the I L alpha line on 2 PET (pentaerythritol) diffracting crystals. Starting from the center to the outer edge of each thin section, samples were stepped beneath the fixed electron

beam in 1-μm spots shoulder-to-shoulder increments with a 2-second acquisition time at each point. In order for the spot size to remain constant, the surface of the specimen must remain within the same focal plane, however some specimen experienced lifting or bubbling of the coral, increasing the spot size. While every possible effort was made to identify and avoid such areas it may not have been always possible, resulting in measurements with larger spot sizes. BSE, iodine, and bromine were measured from the center to the outer edge of each thin section. The SEM analyses were taken at a horizontal or vertical transect at side-by-side 1-μm spot intervals. The directions were chosen based on the quality of the thin section.

3.3.3 Iodine Count Measurement

Iodine counts were measured along the entire radial distance of a thin section for five specimens. For one specimen from the SEUS Stetson Banks, (STET-JSL05-4904-BC2) two radial transects were measured. This was to determine reproducibility of iodine counts within the same specimen. The gaps in the iodine counts, due to desiccation cracks, were removed to properly represent the radial distance of the specimen. To reduce the base-line noise from the iodine analyses, a threshold of 1000 was implemented. The iodine data points were then analyzed in order to count the peaks, which are assumed to correspond with the growth band in the deep-sea black coral skeleton. Once the iodine peaks are identified, a high-resolution chronology was developed for each specimen and the life span was determined. This iodine age chronology was developed by knowing if the specimen were collected alive and

assigning a calendar year to each identified iodine peak, which were proven to be annual in chapter 1 (Figure 29).

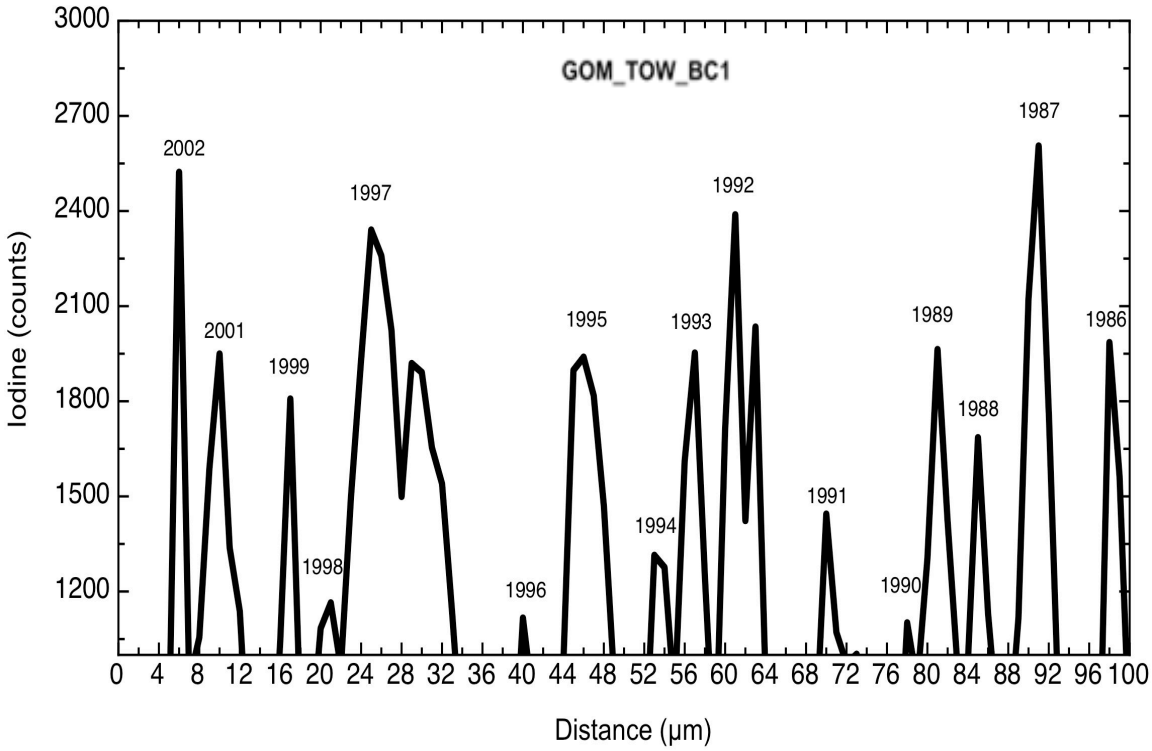

Figure 29 Development of iodine chronology. Examples of how iodine peaks were identified using iodine counts (GOM-TOW-BC1) with the 1000 and 2 µm thresholds (see text for explanation). This specimen was collected alive in 2003, permitting calendar years to be assigned iodine peaks.

3.3.4 Radiocarbon Dating

Individual layers, previously pealed, were radiocarbon dated by AMS at the CAMS-LLNL. Individual layers were subsampled to obtain weights of 1-4 mg. Reported ^{14}C ages were converted to calendar ages using a Calb. 7.0 2013 (http://calib.qub.ac.uk/calib/calib.html) program (Stuiver and Reiner, 1993) and the Marine13 calibration curve (Hughen et al., 2004). Radiocarbon ages are corrected for the differences between the atmospheric radiocarbon content and the local radiocarbon content of the surface ocean, also known as a "reservoir age correction" (ΔR).

3.3.5 Reservoir Age Calculations

To calculate the reservoir ages, the iodine age chronologies were used to determine the atmospheric ^{14}C age. The atmospheric^{14}C ages were obtained from the Intcal13 (Reiner et al., 2013) radiocarbon dataset and were then subtracted from radiocarbon measurements in the coral skeleton to calculate the ^{14}C reservoir ages of the black coral skeleton from the GOM and SEUS specimen.

3.4 Results and Discussion

3.4.1 Reservoir Ages

Using ^{14}C ages and the newly developed iodine chronology from chapter 1, the reservoir ages for both GOM and SEUS specimens were calculated (Table 11). Reservoir ages plotted against the independent calendar age chronology (e.g. iodine chronology) shows reservoir ages varying from 120 to 865 ^{14}C years on decadal to

centennial time scales in the GOM specimens (Figure 30). SUES specimens are also plotted against the independent calendar age chronology showing reservoir ages varying from ~300 to a little over 1000 ^{14}C years on a decadal to centennial time scale (Figure 31).

Sample ID	Reservoir Ages Ranges	Error
	(^{14}C years)	(^{14}C years)
GOM-JSL04-4734-BC1	120-540	±33
GOM-TOW-BC1	230-640	±30
GOM-TOW-BC2	285-865	±19
SET-JSL05-4904-BC1	485-1065	±32
SET-JSL05-4904-BC2	195-400	±32

Table 11 Calculated reservoir ages. The calculated reservoir age ranges of each specimen collected from the Gulf of Mexico and SEUS.

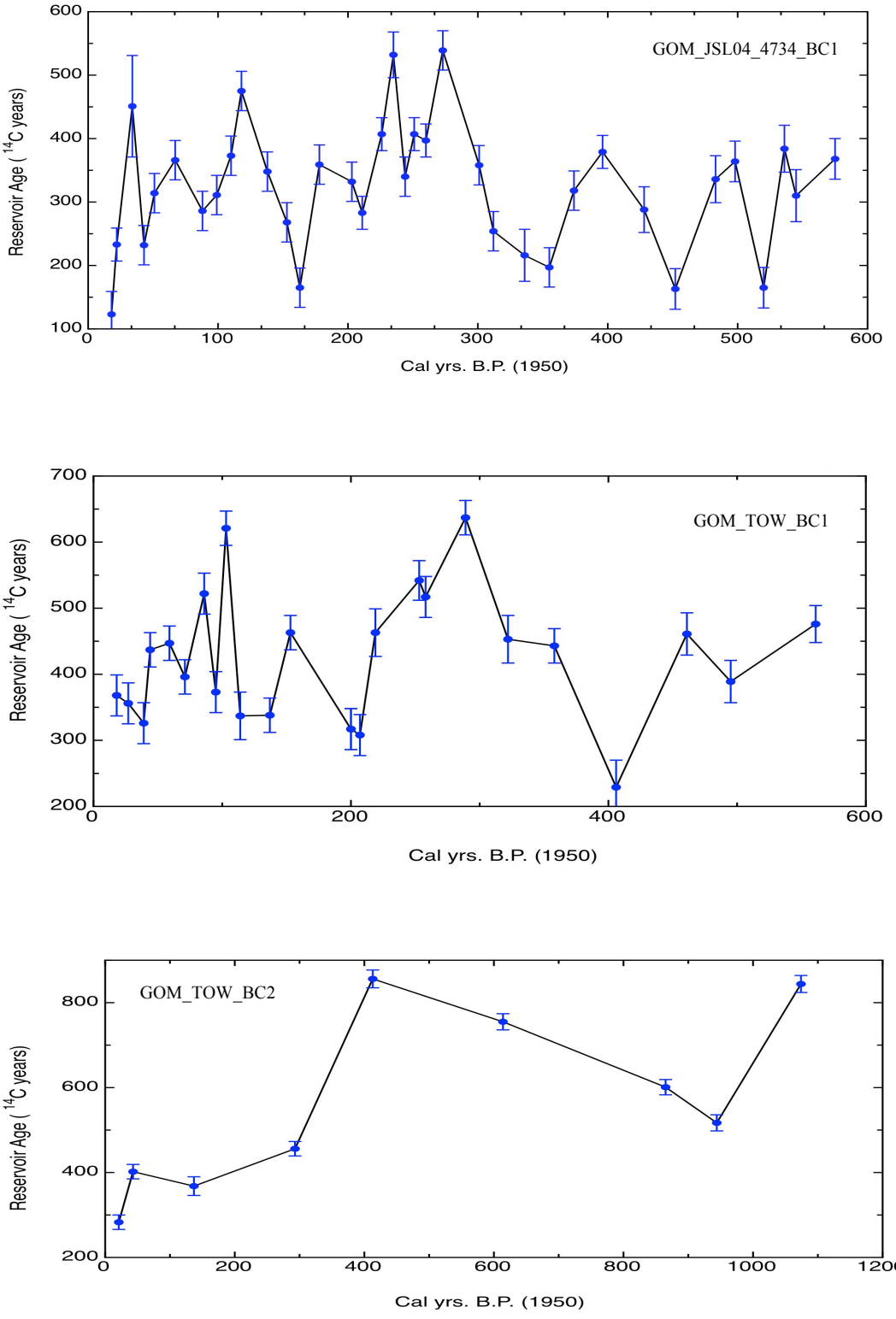

Figure 30 GOM time series od reservoir ages. Records of time versus reservoir ages for specimens from the GOM. The calendar years are from chronologies developed using iodine counts.

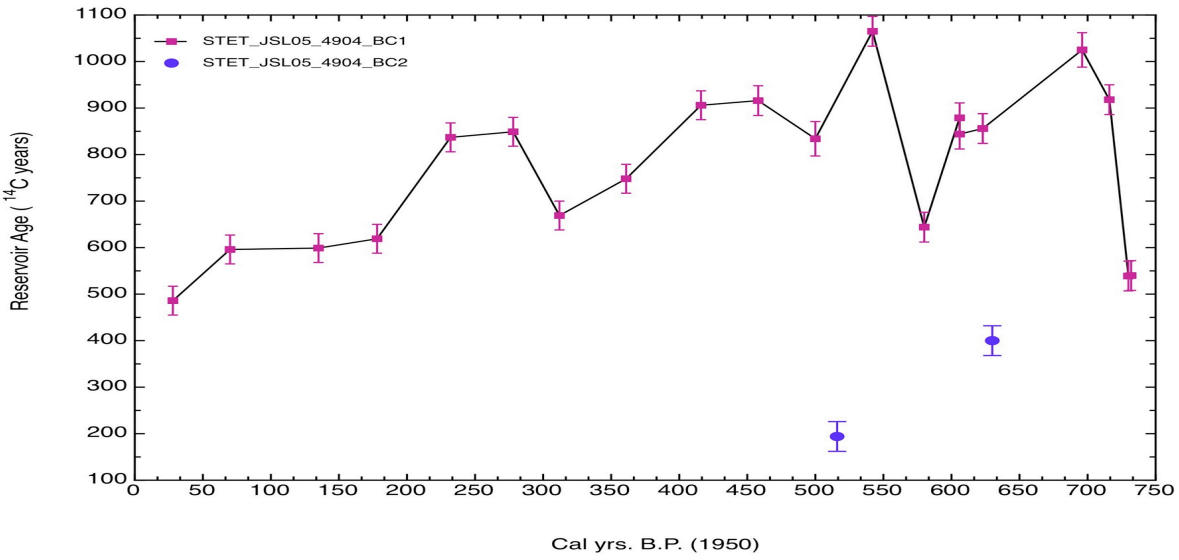

Figure 31 SEUS time series of reservoir ages. Records of time vs. reservoir age from the SEUS. The calendar years are from the chronologies based on iodine counts. The STET-JLS05-4904-BC2 had only three radiocarbon ages, which only two were dated BP (1950) resulting in only two reservoir ages.

After comparing all the specimens from the GOM, GOM-TOW-BC2 reservoir ages did not match the records from the other two specimens prior to 400 yr BP (Figure 32). Since all the specimens from the GOM are from the same general location then 1) these archives are not recording a reproducible environmental signal or 2) there is something wrong in the iodine chronology that is causing the 800-year reservoir ages. The iodine chronologies have shown good correspondence with the visual growth bands found in the corals skeleton (chapter 1), providing confidence that the iodine peaks are annual. The GOM-TOW-BC2 specimen could have experienced lifting or bubbling not seen on the thin section used for the SEM analyses, causing greater uncertainty in the iodine chronology. Alternatively, the pathway that the ^{14}C is taking to the coral may be different. If the POC exports from the surface water, where $^{14}C_{POC} = {}^{14}C_{DIC}$ in surface water but changes in the export process (productivity levels), could have an impact on the reservoir ages of these corals. The dominant signal seen in the GOM reservoir ages is one of changes in ocean circulation and the GOM-TOW-BC2 results should be re-analyzed in future studies. The SEUS specimen (STET-JSL05-4904-BC2) also did not match the reservoir ages of the other SEUS specimen. These differences in reservoir age could also be explained by the problems covered in the GOM (GOM-TOW-BC2) specimen. The STET-JSL05-4904-BC2 specimen had only two reported reservoir ages, which also limits the interpretation of these results. The uncertainties of theses unexplained signals need further investigation so further discussion will be limited.

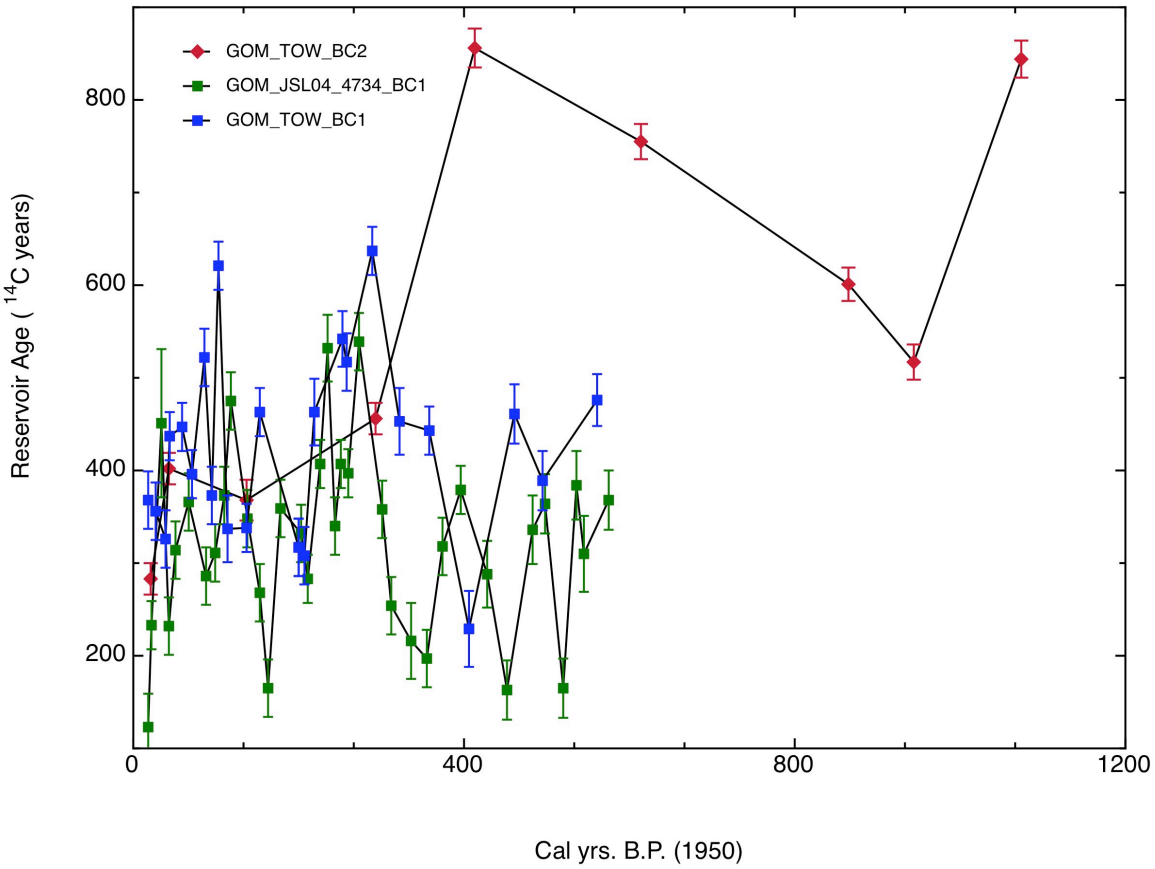

Figure 32 Regional reservoir ages from the GOM and SEUS. Calculated reservoir ages for all SEUS and GOM specimens (except for GOM-JSL09-3728-BC1)

3.4.2 Causes of Variable Reservoir Ages

The reservoir ages in the surface ocean can change because of a number of different influencing factors. First, falling atmospheric $\Delta^{14}C$ values can give transient lower reservoir ages. Influences of regional river discharge, such as proximity of the GOM specimens to the Mississippi River discharge, could also effect ^{14}C reservoir ages due to different mixing of water masses. The most promising explanation for low reservoir ages is reduced mixing between surface and subsurface water. Upwelling has been described in the centers of mesoscale gyres off the Tortugas region (Southwestern Keys) that move north with the Florida Current (Lee et al., 1995). Upwelling is significant because it brings older water to the surface of the ocean and causes older/higher reservoir ages. When the Yucatan Current is strong, it invades the GOM forming a Loop Current, introducing a flow south past the Tortugas that initiates gyre formation as the current reenters the Florida Straits (Figure 33). When the Yucatan current is weak, it turns sharply eastward of the Tortugas directly into the Florida Straits and no gyres are formed (Lee et al., 1995). Thus, there would is a mechanism for turning on and off regional upwelling, which could change the reservoir ages recorded in coral skeletons from the GOM and the Florida Straights (Druffel et al., 2008).

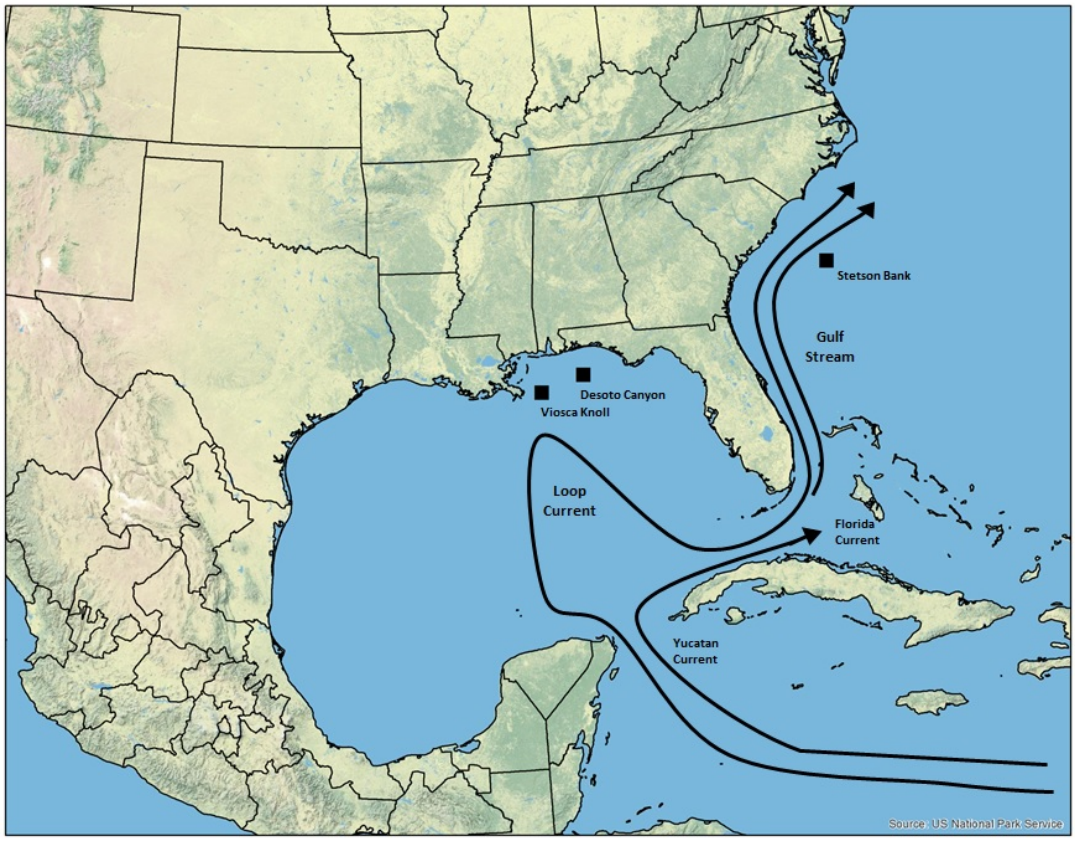

Figure 33 Strength of the Yucatan Current. A map representing the strong (forming a Loop Current in the GOM) and weak (turns sharply eastward) Yucatan Current along with the locations where the GOM and SEUS specimen were collected.

The reservoir age variability reported for this project ranged from ~100 to 600 years for the GOM and ~300 to 1000 years for the SEUS. Previous studies have reported an average reservoir age of 235 ±11 years in the GOM and 242 ±12 years for the Caribbean (Wagner et al., 2009). In the Florida Keys the reservoir ages range from 281 ±21 to 405 ±18 years (Druffel, 1980; Druffel, 1982; Druffel and Linick, 1978). A study of corals in Puerto Rico reported reservoir ages that ranged from 306 ±14 to 402 ±13 years (Kilbourne et al., 2007). Guilderson et al. (2005) reported reservoir ages of corals from Venezuela, varying from 256 ±42 to 285 ±43 years. Compared to these previous studies, most of the reservoir age results (120 to 865 Cal yr BP) of this project from the GOM fall within the ranges previously reported, with the exception of GOM-TOW-BC2 that reported a reservoir age as high as 866 ±19 years. The SEUS also had higher reservoir ages than these previous studies but this could be explained by regional differences in the locations of the corals specimens. Unfortunately, there are no other reservoir age records for the SEUS.

Reconsidering GOM results, the reservoir ages are much more variable than previous records. The most promising explanation for this variability is changes between a strong and weak Yucatan current. When the Yucatan Current is strong, a Loop Current is formed causing gyre formation and upwelling, increasing the reservoir ages in the GOM. When the Yucatan Current is weak, it turns sharply eastward into the Florida Straits causing a reduction of mixing and upwelling of ocean water due to the absence of the Loop Current (Druffel et al., 2008).

The reservoir ages from the SEUS specimens were compared to the reservoir ages from the GOM (Figure 34). The SEUS specimen (STET-JSL05-4904-BC1) has higher reservoir ages than the reservoir ages of the GOM specimens because different water masses have different source regions, such as subtropical waters that contain relatively high amounts of radiocarbon (^{14}C) or equatorial water that are influenced by the upwelling of low ^{14}C water (Kilbourne et al., 2007). The variability in the SEUS reservoir ages could be a response to the strength or weakness of the Gulf Stream. Whenever the density of the Gulf Stream (Florida Straits) current increases there seems to be an increase in reservoir ages (Lund et al., 2006). The same correspondence was seen when the density of the Gulf Stream decreased, in which case there was a decrease in reservoir age in the SEUS region that occurred around the same calendar ages. The higher reservoir ages in the SEUS than the GOM can also be caused by changes in the strength and weakness of the Yucatan Current. For example, when the Yucatan is strong it causes reservoir ages to increase in the GOM and reduces the reservoir age gap between the two regions (Figure 34).

Major climatic events, such as the Little Ice Age or the Medieval Warm Period, can be seen in the reservoir age records. GOM specimens (GOM-JSL04-4734-BC1 and GOM-TOW-BC2) had their lowest reservoir ages starting from ~1650 to 1850, which falls during the Little Ice Age. SEUS specimen STET-JSL05-4904-BC1 had the longest reservoir age record from both regions and revealed high reservoir ages in ~AD 1250, during the Medieval warming period (Figure 34).

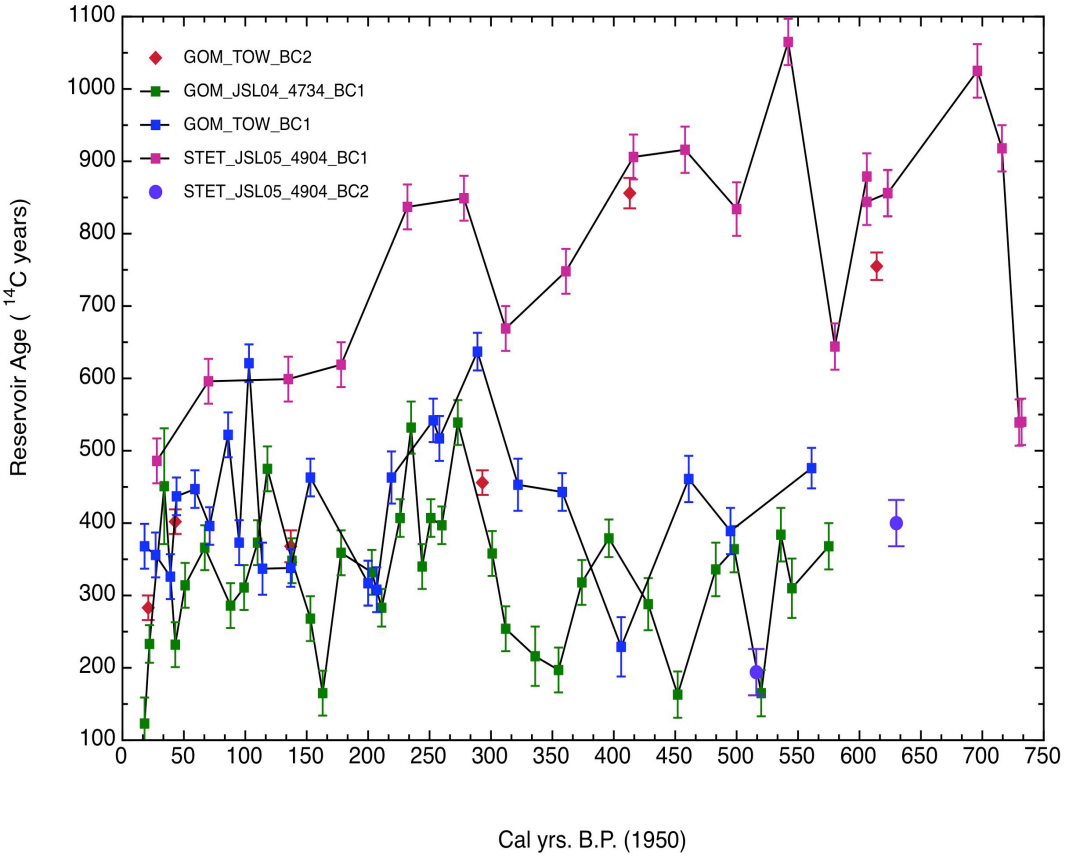

Figure 34 Variability of reservoir ages. Calculated reservoir ages for all the GOM and SEUS specimens (except for GOM-JSL09-3728-BC1).

3.5 Conclusion

High-resolution sampling of iodine analyses and radiocarbon ages in DSC (*Leiopathes* sp.) allowed the determination of ^{14}C reservoir ages in the GOM and SEUS regions over the last ~500 to 1000 years. These findings provide a rare time-series record of highly variable reservoir ages suggestive of changing ocean dynamics in association with climatic events in the late Holocene period. The preferred explanation for the variability in these reservoir ages is the effect of changes in the strength of the Yucatan Current. When the Yucatan Current is strong, a loop current forms and causes gyre formation and upwelling to occur, increasing the reservoir ages in the GOM. When the Yucatan Current is weak, it turns sharply eastward into the Florida Straits and causes a reduction of mixing and upwelling of ocean water due to the absence of the loop current (Druffel et al., 2008). For the GOM samples, another explanations of variability is proximity of the corals to Mississippi River discharge. Decreasing atmospheric $\Delta^{14}C$ values could also result in lower reservoir ages. The SEUS high and variable reservoir ages could be a result of the changes in the Gulf Stream.

Major climatic events, such as the Little Ice Age or the Medieval Warm Period can be seen in the reservoir age records of the GOM and SEUS. Geochemical signatures are also captured in coral skeletal protein, like stable carbon ($\delta^{13}C$), that has been used to reproduce environmental impacts, such as the "Seuss effect". Thus, establishing independent chronologies of coral skeletons as archives of oceanographic biochemical changes are vital to observing long-term changes and variance in ocean dynamics associated with climatic events.

CHAPTER IV

SUMMARY

This study is the first to validate that the rings deposited in the skeleton of deep-sea black corals, Leiopathes sp., are annual growth bands and that peaks in iodine counts associated with the growth band can be used as an independent dating method if good quality thin sections are made before analyses are conducted. The high-resolution iodine chronologies paired with radiocarbon ages allowed this project to resolve reservoir ages in the GOM and SEUS regions. These findings provide a rare, continuous time series of highly variable reservoir ages suggestive of changing ocean dynamics in association with climatic events in the late Holocene. The preferred explanation for the variability in reservoir ages is the effect of changes in the strength of the Yucatan current.

REFERENCES

Adkins, JF (1998). Deep-sea Corals: A New Oceanic Archive. *Doctoral Dissertation*, Massachusetts Institute of Technology Woods Hole Oceanographic Institute, Cambridge, MA, 1-233.

Adkins, JF, H Cheng, EA Boylem, ERM Druffel, RL Edwards (1998) Deep-sea coral evidence for rapid change in ventilation of the deep North Atlantic 15,400 years ago. *Science* 280, 725-728.

Andrew, AH, GM Cailliet, LA Kerr, KH Coale, C Lundstrom, A DeVogelaere (2005). Investigations of age and growth for three species of deep-sea coral from the Davidson Seamount off central California. *Cold-water corals and ecosystems,* Springer-Verlag, Berlin**,** 965-982.

Baker, MS and CA Wilson (2001). Use of bomb radiocarbon to validate otolith section ages of red snapper *Lutjanus campechanus* from the Northern Gulf of Mexico. *Limnol Oceanogr*, 46, 1819-1824.

Bradley, RS (1999) Paleoclimatology: reconstructing climates of the quaternary. San Diego, CA. Academic Press.

Brook, S and WW Schroeder (2007). State of deep coral ecosystems in the Gulf of Mexico region: Texas to the Florida Straits. *The state of deep coral ecosystems of the United States.* NOAA Tech Memo CRCP-3. Silver Springs, MD**,** 271-306.

Carreiro-Silva, M, AH Andrews, A Braga-Henriques, V de Matos, FM Porteiro, RS Santos (2013). Variability in growth rates of long-lived black coral *Leiopathes* sp. from Azores. *Marine Ecology-Progress Series,* 473**,** 189-199.

Chuenpagdee, R, LE Morgan, SM Maxwell, EA Norse, D Pauly (2003). Shifting gears: assessing collateral impacts of fishing methods in US waters. *Frontiers in Ecology and the Environment,* 1, 517-525.

Druffel, ERM and TW Linick (1978). Radiocarbon in annual coral rings of Florida. *Geophysical Research Letters*, 5, 913-916.

Druffel, ERM (1980). Radiocarbon in annual coral rings of Belize and Florida. *Radiocarbon*, 22, 363-371.

Druffel, ERM, (1982). Banded corals: changes in oceanic carbon-14 during the Little Ice Age. *Science* 218, 13-19.

Druffel, ERM, S Griffin, A Witter, E Nelson, J Southon, M Kashgarian, J Vogel (1995). *Gerardia*: bristlecone pine of the deep-sea. *Geochim Cosmochim Acta,* 59, 5031-5036.

Druffel, ERM, LF Robinson, S Griffin, RB Halley, JR Southon and JF Adkins (2008). Low reservoir ages for the surface ocean from mid-Holocene Florida corals. *Paleoceanography,* 23.

Fossa, JH, PB Mortensen, and DM Furevik (2002). The deep-water coral *Lophelia pertusa* in Norwegin waters: distribution and fishery impacts. *Hydrobiologia*, 471, 1-12.

Goldberg, WM (1978). Chemical changes accompanying maturation if the connective tissue skeletons of gorgonian and antipatharian corals, *Marine Biology*, 49, 669-670.

Goldberg, WM (1991). Chemistry and structureod skeletal growth rings in the black coral Anthipathes *fiordensis* (Cnidaria, Antipathatia). *Hydrobiologia*, 216-217, 403-409.

Grange, KR and WM Goldeberg (1992). Chronology of black coral growth bands: 300 years of environmental history. *Proc 2nd Int. Temperate Reef Symp, Auckland, New Zealand*, NIWA Marine, Wellington, 169-174.

Grigg, RW (1974). Growth rings: annual periodicity in two gorgonian corals. *Ecology*, 55, 876-881.

Grigg, RW (1976). Fishery Management of Precious and Stony Corals in Hawaii. *Sea Grant Technical Report*, 1-48.

Grigg, RW (2001). Black Coral: Historical of sustainability fishery in Hawaii. *Pac Science*, 55, 291-299.

Grigg, RW (2002). Precious Corals in Hawaii: Discovery of a New Bed and Revised Management Measures for Existing Beds. *Marine Fisheries Review 64 (1)*, 13-20.

Guilderson, TP, JE Cole, J Southon (2005). Pre-bomb $\Delta\ ^{4}C$ variability and the Seuss Effect in Cariaco Basin surface waters are recorded in hermatypic corals. *Radiocarbon*, 47, 57-65.

Hillaire-Marcel, C and A de Vernal (2007). Proxies in Late Cenozoic Paleoceanography. *Jordan Hill*, Oxford, UK: Elsevier, 1-425

Hovlan, M (1990). Do carbonate reefs form due to fluid seep-age? *Terra Nova*, 2, 8-18.
Hughen, KA, MGL Basille, E Bard, A Bayliss, and 23 others (2004). Marine04: marine radiocarbon age calibration, 26-0 ka BP. *Radiocarbon*, 46, 1059-1086.

Kilboutne, KH, TM Quinn, TP Guilderson, RB Webb, FW Taylor (2007). Decadal- to interannual-scale source water variations in the Caribbean Sea recorded by Puerto Rican coral radiocarbon, *Cilmate Dynamics*, 29, 5-63.

Komugabe, AF, SJ Fallon, RE Thresher, SM Eggings (2013). Modern Tasman Sea surface reservoir ages from deep-sea black corals. *Deep-Sea Research II,* 99, 207-212.

Koslow, JA, KG Holmes, JK Lowry, et al. (2001). Seamounts benthic macrofauna off southern Tasmania: community structure and impacts of trawling. *Marine-Ecology Progress Series*, 213, 111-25.

Lee, TN et al. (1995). Florida current meanders and gyre formation in the southern Straits of Florida. *Journal of Geophysical Research: Oceans*, 100, 8607-8620.

Lighty, RG, IG Macintyre, and R Stuckenrath (1982). Acropora Palmata reef framework: A reliable indicator of sea level in the Western Atlantic for the past 10,000 years. *Coral Reefs* 1,125-130.

Lund, DC, J Lynch-Stieglitz, and WB Curry (2006). Gulf Stream density structure and transport during the past millennium. *Nature*, 444, 601-604.

Morgan, LE, P Etnoyer, AJ Scholz, N Nertens, M Powell (2005). Conservation and management implications of deep-sea coral and fishing effort distributions in the northeast Pacific Ocean. *Cold-water Corals and Ecosystem,* 157-169.

Nowak, D, M Florek, J Nowak, W Kwiatek, and others (2009). Morphology and chemical make-up of the inorganic components of black corals. *Materials Science and Engineering: C,* 29**,** 1029-1038.

Oeschger, H, U Siegenthaler, U Schotterer, and A Gugelman (1975). A box diffusion model to study the carbon dioxide exchange in nature. *Tellus*, 27, 168-192.

Parrish, FA and EB Roark (2009). Growth validation of gold coral Gerardia sp in the Hawaiian Archipelago. *Marine Ecology-Progress Series,* 397**,** 163-172.

Prouty, NG, EB Roark, NA Buster, and SW Ross (2011). Growth rate and age distribution of deep-sea black corals in the Gulf of Mexico. *Marine Ecology-Progress Series,* 423**,** 101-U121.

Reimer, PJ, MGL Ballie, E Brad, A Bayliss, and others (2004). IntCal04 terrestrial radiocarbon age calibration, 0-26 Cal kyr BP. *Radiocarbon* 46(3), 1029-1058.

Reimer, PJ, MGL Ballie, E Brad, A Bayliss, and others (2009). IntCal09 and Marine 09 radiocarbon age calibration curves, 0-50,000 years cal BP. *Radiocarbon* 51, 1111-1150.

Reimer, E Brad, A Bayliss, and others (2013). IntCal13 and Marine13 radiocarbon age calibration curves, 0-50,000 years cal BP. *Radiocarbon*, 55, 1869-1887.

Risk, MJ, OA Sherwood, R Nairn, C Gibbons (2009). Tracking the record of sewage discharge off Jeddah, Saudi Arabia, since 1950, using stable isotopes records from Antipatharians. *Marine Ecology-Progress Series,* 397, 219-226.

Roark, EB, TP Guilderson, S Flood-Page, RB Dunbar, BL Ingram, SJ Fallon, M McCulloch (2005). Radiocarbon-based ages and growth rates of bamboo corals from the Gulf of Alaska. *Geophysical Research Letters*, Vol 32, Issue, 4, L04606.

Roark, EB, TP Guilderson, RB Dunbar, and BL Ingram (2006). Radiocarbon-based ages and growth rates of Hawaiian deep-sea corals. *Marine Ecology-Progress Series,* 327**,** 1-14.

Roark, EB, TP Guilderson, RB Dunbar, BL Fallon SJ, and DA Mucciarone (2009). Extreme Longevity in Proteinaceous Deep-sea coral. *Proceedings of the National Academy of Science USA,* 106**,** 5204-5208.

Robert, S and M Hirshfield (2004). Deep-sea corals: out of sight, but no longer out of mind. *Frontiers in Ecology and the Environment*, 2, 123-130.

Robinson, LF, JF Adkins, LD Keigwin, J Southon, DP Fernandez, SL Wang, DS Scheirer (2005). Radiocarbon variability in the Western North Atlantic during the last deglaciation. *Science*, 310, 1469-1473.

Roche, JMF, M Fontaine, J Leleoup (1963). Halides. *Comparative Biochemistry*, 5, 493-547.

Sherwood, OA (2002). The deep-sea gorgonian coral Primnoa resedaeformis as an oceanographic monitor. *MSc Thesis,* McMaster University, Hamilton, ON.

Sherwood, OA, DB Scott, MJ Risk, and TP Guilderson (2005). Radiocarbon evidence for annual growth rings in the deep-sea octocoral Primnoa resedaeformis. *Marine Ecology-Progress Series,* 301**,** 129-134.

Sherwood, OA, EN Edinger (2009). Ages and Growth rates of some deep-sea gorgonian and antipatharian corals of Newfoundland and Labrador. *Can J Fish Aquat Science* 66**,** 142-152.

Stanley, CD and SD Cairns (1988). Constructional azooxanthellate coral communities: an overview with implications for the fossil records. *Palaios*, 3, 233-243.

Stuiver, M and PD Quay (1980). Changes in atmospheric carbon-14 attributed to a variable Sun. *Science*, 207, 11-19.

Stuiver, M, et al (1986). Radiocarbon age calibration of marine samples back to 9000 cal yr BP. *Radiocarbon,* 28, 980-1021.

Stuiver, M and TF Braziunas (1993). Modeling atmospheric ^{14}C influences ans ^{14}C ages of marine samples to 10,000 BC. *Radiocarbon,* 35**,** 123-130.

Stuiver, M and PJ Reimer (1993). Extended ^{14}C database and revised CALIB radiocarbon calibration program. *Radiocarbon*, 35, 215-230.

Wagner, AJ, TP Guilderson, N Slowey, JE Cole (2009). Pre-bomb surface water radiocarbon of the Gulf of Mexico and Caribbean as recorded in hermatypic corals. *Radiocarbon*, 51, 947-954.

Williams, B., M. J. Risk, S. W. Ross & K. J. Sulak (2006). Deep-water antipatharians: Proxies of environmental change. *Geology,* 34**,** 7-14.

Williams, B, MJ Risk, SW Ross, and KJ Sulak (2007). Stable isotope data from deep-water Antipatharians: 400-year records from the southeastern coast of the United States of America. *Bulletin of Marine Science,* 81**,** 437-447.

Witherell D, P Clarence, D Fluharty (2000). A ecosystem-based approach for Alaska groundfish fisheries. *ICES Journal of Marine Science*, 55, 771-777.

APPENDIX A

SUMPLEMENT DATA SUMMARY

Sample ID	Lab ID	Distance (um)	Fraction Modern	± SD	Δ 14C	14C Age	± SD	ΔR	± SD	No. Age Ranges	Minumum Cal age range (1s) cal BP	Maximum Cal age range (1s) Cal BP	Relative area under distribution	Median probability Age	Iodine cal year (4 um)	I Cal ±	IntCal13 14C age	IntCal13 Error	Delta 14C	Sigma	reservoir age	res age ±
GOM-JSL04-4734-BC1 (Prouty et al. 2011) .																						
VK 1	NOSAMS	125	1.0793	0.0036	71.86	>Modern		-30	26						2001							
VK 2	NOSAMS	313	1.1061	0.0042	98.50	>Modern		-30	26						1999							
VK 1a	NOSAMS	313	1.1045	0.0042	96.91	>Modern		-30	26						1999							
VK 3a	BetaAnalytic	414	1.109	-	101.38	>Modern		-30	26						1994							
VK 4	NOSAMS	464	1.1109	0.0039	103.31	>Modern		-30	26						1992							
VK 6	NOSAMS	614	1.1200	0.0042	112.28	>Modern		-30	26						1982							
VK 8	NOSAMS	827	1.1267	0.0059	118.93	>Modern		-30	26						1967							
VK 8a	NOSAMS	1090	1.1222	0.0043	114.52	>Modern		-30	26						1956							
VK 1a	BetaAnalytic	1153	1.112	-	104.36	>Modern		-30	26						1952							
VK 34a	NOSAMS	1266	1.0754	0.0039	68.02	>Modern		-30	26						5	1						
VK 16	NOSAMS	1504	0.9662	0.0041	-40.44	275 a	35	-30	26						18	2	152	7	-16.4	0.9	123	36
VK 10a	NOSAMS	1567	0.9555	0.003	-51.10	365 a	25	-30	26						22	2	132	6	-13.3	0.7	233	26
VK 5a	NOSAMS	1767	0.9332	0.0095	-73.18	555	80	-30	26	1	100	305	1.00	210	34	3	104	7	-8.7	0.9	451	80
VK 23a	NOSAMS	1968	0.9616	0.0037	-45.00	315 a	30	-30	26						43	4	83	7	-4.9	0.9	232	31
VK 33a	NOSAMS	2106	0.9530	0.0035	-53.56	385 a	30	-30	26						51	5	71	7	-2.8	0.9	314	31
VK 2a	NOSAMS	2319	0.9432	0.0035	-63.27	470	30	-30	26	4	0 55 160	10 150 195	0.05 0.67 0.19	120	67	7	104	7	-4.5	0.9	366	31
VK 14a	NOSAMS	2582	0.9510	0.0037	-55.53	405 a	30	-30	26						88	9	119	6	-3.9	0.7	286	31
VK 11a	NOSAMS	2732	0.9485	0.0036	-57.99	425	30	-30	26	1	0	100	1.00	70	99	10	114	9	-2.1	1.1	311	31
VK 7a	NOSAMS	2870	0.9401	0.0037	-66.41	495	30	-30	26	1	105	240	1.00	160	110	11	122	8	-1.9	1	373	31
VK 20a	NOSAMS	2971	0.9316	0.0037	-74.8	570	30	-30	26	3	150 190 220	160 215 290	0.10 0.14 0.76	240	118	12	95	7	2.7	0.9	475	31
VK 16a	NOSAMS	3171	0.9419	0.0036	-64.53	480	30	-30	26	2	80 155	155 230	0.53 0.47	135	138	14	132	8	0.5	1	348	31
VK 4a	NOSAMS	3322	0.9417	0.0036	-64.76	480	30	-30	26	2	81 155	156 230	0.53 0.48	135	153	15	212	8	-7.6	1	268	31
VK 38A	NOSAMS	3483	0.9537	0.0037	-52.84	380	30	-30	26						163	16	215	8	-6.8	1	165	31
VK 6a	NOSAMS	3635	0.9356	0.0037	-70.87	535	30	-30	26	2	145 170	170 260	0.21 0.79	195	178	18	176	8	-0.1	1	359	31
VK 26a	NOSAMS	3886	0.9399	0.0036	-66.55	495	30	-30	26	1	105	240	1.00	160	203	20	163	7	4.5	0.9	332	31
VK 24a	NOSAMS	4086	0.9454	0.0032	-61.13	450	25	-30	26	2	0 40	35 125	0.25 0.75	95	211	21	167	7	4.6	0.9	283	26
VK 12a	NOSAMS	4324	0.9370	0.0029	-69.43	520	25	-30	26	1	140	250	1.00	185	226	23	113	6	13.2	0.8	407	26
VJ 28a	NOSAMS	4550	0.9249	0.040	-81.5	625	35	-30	26	1	260	360	1.00	305	235	24	93	7	17	0.9	532	36
VK 35a	NOSAMS	4675	0.9462	0.0036	-60.33	445	30	-30	26	2	0 40	35 125	0.28 0.72	90	244	24	105	6	16.7	0.8	340	31
VK 27a	NOSAMS	4788	0.9381	0.0032	-68.31	510	25	-30	26	1	130	245	1.00	175	251	25	103	6	17.6	0.8	407	26
VK 22a	NOSAMS	4989	0.9358	0.0031	-70.6	530	25	-30	26	2	145 170	170 255	0.22 0.78	195	260	26	133	6	15	0.8	397	26
VK 3a	NOSAMS	5189	0.9148	0.0037	-91.51	715	30	-30	26	1	330	435	1.00	385	273	27	176	7	11.4	0.9	539	31
VK 25a	NOSAMS	5502	0.9269	0.0036	-79.5	610	30	-30	26	1	245	335	1.00	290	301	30	252	7	4.9	0.9	358	31

VK 32a	NOSAMS	5628	0.9325	0.0037	-73.93	560	30	-30	26	2	145 190	165 280	0.13 0.87	225	312	31	306	7	0	0.9	254	31
VK 5a	BetaAnalytic	5966	0.9315	-	-74.90	570	40	-30	26	2	145 185	165 295	0.12 0.88	240	336	34	354	7	-3.5	0.9	216	41
VK 36a	NOSAMS	6217	0.9351	0.0036	-71.33	540	30	-30	26	2	145 175	165 265	0.19 0.81	200	355	36	343	8	0.2	1	197	31
VK 13a	NOSAMS	6468	0.9220	0.0036	-84.36	650	30	-30	26	1	280	375	1.00	330	374	38	332	8	4	1	318	31
Vk 31a	NOSAMS	6768	0.9173	0.0030	-88.97	695	25	-30	26	1	320	425	1.00	370	396	40	316	8	8.5	1	379	26
VK 29a	NOSAMS	7069	0.9249	0.004	-81.43	625	35	-30	26	1	260	360	1.00	305	428	43	337	8	10.1	1	288	36
VK 39a	NOSAMS	7270	0.9376	0.0034	-68.84	515	30	-30	26	1	130	250	1.00	180	452	45	352	11	11.3	1.4	163	32
VK 19a	NOSAMS	7596	0.9134	0.0039	-92.90	725	35	-30	26	2	335 350	345 450	0.09 0.91	395	483	50	389	11	10.3	1.4	336	37
VK 17a	NOSAMS	7784	0.9072	0.0033	-99.04	780	30	-30	26	1	420	490	1.00	450	498	50	416	12	8.7	1.5	364	32
VK 37a	NOSAMS	8047	0.9217	0.0036	-84.68	655	30	-30	26	1	285	380	1.00	335	520	52	490	12	1.9	1.5	165	32
VK 30a	NOSAMS	8273	0.8926	0.0040	-113.54	910	35	-30	26	2	500 580	565 595	0.90 0.10	540	536	54	526	11	-0.8	1.4	384	37
VK 4a	BetaAnalytic	8398	0.8974	-	-108.81	870	40	-30	26	1	475	545	1.00	515	545	55	560	11	-3.8	1.4	310	41
VK 9a	NOSAMS	8824	0.8803	0.0031	-125.78	1020	30	-30	26	2	565 595	580 655	0.13 0.87	620	575	60	652	11	-11.5	1.4	368	32
GOM_JSL09_3728_BC1	(Prouty et al. 2011)																					
3728 1.1	KCCAMS	45	1.061	0.0035	53.35	>Modern		-30	26						2004							
3728 1.2	KCCAMS	72	1.0753	0.0036	67.50	>Modern		-30	26						2003							
3728 1.3	KCCAMS	95	1.0773	0.0039	69.50	>Modern		-30	26						2002							
3728 1.4	KCCAMS	112	1.0803	0.0037	72.45	>Modern		-30	26						2001							
3728 1.5	KCCAMS	151	1.1036	0.0036	95.62	>Modern		-30	26						2000							
3728 2.1	KCCAMS	1418	0.9036	0.0032	-102.98	815	30	-30	26	1	450	505	1.00	475	61	6	98	7	-4.9	0.9	717	31
3728 3.1	KCCAMS	3589	0.8221	0.0081	-183.89	1570	80	-30	26	1	1070	1245	1.00	1150	222	22	113	6	13.2	0.8	1457	80
3728 3.1 duplicate	KCCAMS	3589	0.8188	0.0089	-187.09	1610	90	-30	26	1	1100	1285	1.00	1190	222	22	113	6	13.2	0.8	1497	90
3728 4.1	KCCAMS	4382	0.822	0.0029	-183.94	1580	30	-30	26	1	1130	1230	1.00	1170	289	29	233	7	6.1	0.9	1347	31
3728 5.1	KCCAMS	5404	0.8126	0.0028	-193.30	1670	30	-30	26	1	1220	1295	1.00	1250	364	36	332	8	2.8	1	1338	31
3728 6.1	KCCAMS	7144	0.7955	0.0027	-210.21	1840	30	-30	26	1	1350	1465	1.00	1410	500	50	416	12	8.7	1.5	1424	32
3728 7.1	KCCAMS	11838	0.7724	0.0026	-233.18	2080	30	-30	26	1	1615	1740	1.00	1690	835	84	950	10	-17.1	1.2	1130	32
3728 7.19	KCCAMS	18090	0.7439	0.0025	-261.44	2380	30	-30	26	1	1985	2100	1.00	2040	-							
GOM_JSL09_3728_BC1	Mohon																					
GOM_1.24	CAMS	17	0.9455	0.0034	-54.50	215	30	-30	26	2	0 40	30 131	0.23 0.77	100	2006							
GOM_1.59	CAMS	52	0.9370	0.0033	-63.00	345	30	-30	26	1	136	251	1.00	185	2003							
GOM_1.74	CAMS	67	0.9412	0.0033	-58.80	410	30	-30	26	1	88	234	1.00	145	2002							
GOM_1.9	CAMS	115	0.9324	0.0033	-64.60	425	30	-30	26						2001							
GOM_2.17	CAMS	248	0.9253	0.0033	-74.70	450	30	-30	26	2	258 343	337 357	0.91 0.09	305	1991							
GOM_2.88	CAMS	745	0.9324	0.0033	-67.60	485	30	-30	26	2	147 189	163 281	0.12 0.88	230	1952							
GOM_3.20B	CAMS	1271	0.9172	0.0032	-82.80	520	30	-30	26	1	316	415	1.00	370	43	4	83	7	-4.9	0.9	437	31
GOM 09 4.25	CAMS	2332	0.9235	0.0033	-76.50	560	30	-30	26	1	271	366	1.00	325	111	11	122	8	-1.9	1	438	31
GOM 09 4.53	CAMS	2836	0.9487	0.0041	-51.30	565	35	-30	26	1	0	99	1.00	70	153	15	212	8	-7.6	1	353	36
GOM 09 4.79	CAMS	3304	0.9503	0.0033	-49.70	625	30	-30	26						200	20	163	7	3.9	0.9	462	31

GOM 09 4.108	CAMS	3826	0.9580	0.0035	-42.00	640	30	-30	26						247	25	103	6	17.6	0.8	537	31
GOM 09 5.32	CAMS	4328	0.8738	0.0031	-126.20	695	30	-30	26	1	638	703	1.00	630	285	29	215	7	7.7	0.9	480	31
GOM 09 5.67	CAMS	4818	0.8878	0.0028	-112.20	735	30	-30	26	1	537	613	1.00	575	326	33	332	7	-2	0.9	403	31
GOM 09 6.41	CAMS	5324	0.9127	0.0031	-87.30	955	30	-30	26	1	360	462	1.00	410	357	36	332	8	2.2	1	623	31
GOM 09 6.83	CAMS	5828	0.9734	0.0038	-26.60	1085	35	-30	26						399	40	310	7	9.8	0.9	775	36
GOM 09 7.40	CAMS	6748	0.8465	0.0030	-153.50	1320	30	-30	26	1	874	966	1.00	920	476	48	375	12	10.8	1.5	945	32
GOM09-7-101	CAMS	7785	0.8483	0.0030	-151.70	1340	30	-30	26	1	845	943	1.00	895	530	53	513	12	0.3	1.5	827	32
GOM09-8-27	CAMS	8434	0.8277	0.0038	-172.30	1520	40	-30	26	1	1057	1164	1.00	1110	587	60	621	12	-5.9	1.5	899	42
GOM09-8-42	CAMS	8719	0.8252	0.003	-174.80	1545	30	-30	26	1	1072	1183	1.00	1140	610	61	581	12	1.5	1.5	964	32
GOM09-9-24	CAMS	9242	0.7968	0.0035	-203.20	1825	40	-30	26	2	1341 1452	1448 1458	0.97 0.03	1400	650	65	642	12	-1.3	1.5	1183	42
GOM_TOW_BC1	(Prouty et al. 2011)		Delaminated	Transect											.							
GOMBC 1-2	BetaAnalytic	17	0.9338	-	-72.59	550	60	-30	26	1	130	285	1.00	205	2000							
GOMBC 1-6	BetaAnalytic	68	0.9526	-	-53.94	390	40	-30	26						1992							
GOMBC 1_14a	NOSAMS	102	0.9351	0.0031	-71.3	540	25	-30	26	2	145 180	165 265	0.18 0.82	205	1988							
GOMBC 1-13	BetaAnalytic	145	0.9315	-	-74.90	570	40	-30	26	2	145 185	165 295	0.12 0.88	240	1984							
GOMBC 1_1a	NOSAMS	170	0.9362	0.0039	-70.26	530	35	-30	26	1	140	260	1.00	190	1982							
GOMBC 1_25a	NOSAMS	238	0.9503	0.0033	-56.27	410	30	-30	26						1978							
GOMBC 1_23	BetaAnalytic	306	0.9188	-	-87.48	680	40	-30	26	1	300	405	1.00	360	1971							
GOMBC 1_2a	NOSAMS	357	0.9390	0.0032	-67.45	505	25	-30	26	1	125	245	1.00	170	1969							
GOMBC 1_10a	NOSAMS	425	0.9233	0.0032	-83.00	640	25	-30	26	1	270	360	1.00	320	1964							
GOMBC 1-31	BetaAnalytic	485	0.9455	-	-60.98	450	40	-30	26	1	0	140	1.00	100	1960							
GOMBC 1_15a	NOSAMS	578	0.9240	0.0033	-82.36	635	30	-30	26	1	265	360	1.00	315	1955							
GOM-TOW-BC1 117	KCCAMS	578	0.9287	0.0031	-77.99	595	30	-30	26	2	155 230	155 325	0.00 1.00	270	1955							
GOMBC 1_8a	NOSAMS	833	0.9373	0.0036	-69.17	520	30	-30	26	1	135	250	1.00	185	18	2	152	7	-16.4	0.9	368	31
GOMBC 1_27a	NOSAMS	944	0.9411	0.0036	-65.36	485	30	-30	26	1	90	235	1.00	145	27	3	129	7	-12.4	0.9	356	31
GOMBC 1_28a	NOSAMS	1148	0.9493	0.0036	-57.21	415 a	30	-30	26						39	4	99	7	-7.5	0.9	326	31
GOMBC 1_13a	NOSAMS	1233	0.9373	0.0029	-69.13	520	25	-30	26	1	140	250	1.00	185	44	4	83	7	-4.9	0.9	437	26
GOMBC 1_4a	NOSAMS	1420	0.9342	0.0028	-72.17	545	25	-30	26	2	145 185	165 265	0.17 0.83	210	59	6	98	7	-4.9	0.9	447	26
GOMBC 1_26a	NOSAMS	1573	0.9396	0.0032	-66.87	500	25	-30	26	1	120	245	1.00	165	71	7	104	7	-4.5	0.9	396	26
GOMBC 1_11a	NOSAMS	1717	0.9231	0.0035	-83.28	645	30	-30	26	1	275	370	1.00	325	86	9	123	6	-5	0.7	522	31
GOMBC 1_5a	NOSAMS	1811	0.9400	0.0035	-66.43	495	30	-30	26	1	105	240	1.00	160	95	10	122	8	-3.7	1	373	31
GOMBC 1_16a	NOSAMS	1981	0.9125	0.0031	-93.76	735	25	-30	26	1	365	460	1.00	410	103	10	114	8	-1.5	1	621	26
GOMBC 1_30a	NOSAMS	2130	0.9453	0.0043	-61.16	450	35	-30	26	1	0	130	1.00	100	114	11	113	8	-0.2	1	337	36
GOMBC 1_29a	NOSAMS	2419	0.9429	0.0032	-63.60	470	25	-30	26	4	0 55 160 210	10 150 195 225	0.05 0.68 0.19 0.08	120	137	14	132	8	0.5	1	338	26
GOMBC 1_17a	NOSAMS	2597	0.9196	0.0031	-86.74	675	25	-30	26	1	300	395	1	355	153	15	212	8	-7.6	1	463	26
GOMBC 1_18a	NOSAMS	3048	0.9419	0.0035	-64.55	480	30	-30	26	2	80 155	155 230	0.53 0.47	135	200	20	163	7	3.9	0.9	317	31
GOM-TOW-BC1 34	KCCAMS	3048	0.9421	0.0031	-64.70	480	30	-30	26	2	80 155	155 230	0.53 0.47	135	200	20	163	7	3.9	0.9	317	31

GOMBC 1_3a	NOSAMS	3226	0.9424	0.0035	-64.11	475	30	-30	26	3	65 160 205	150 200 225	0.62 0.25 0.13	130	207	21	167	7	4.6	0.9	308	31
GOMBC 1_7a	NOSAMS	3422	0.9281	0.0039	-78.26	600	35	-30	26	2	230 345	335 355	0.97 0.03	275	219	22	137	8	9.6	1	463	36
GOMBC 1_19a	NOSAMS	3915	0.9213	0.0035	-85.07	660	30	-30	26	1	285	385	1.00	340	253	25	118	5	16.3	0.6	542	30
GOMBC 1_6a	NOSAMS	3991	0.9223	0.0035	-84.05	650	30	-30	26	1	280	375	1.00	330	258	26	133	6	15	0.8	517	31
GOMBC 1_20a	NOSAMS	4340	0.8971	0.0028	-109.11	870	25	-30	26	1	485	535	1.00	510	289	29	233	7	6.1	0.9	637	26
GOMBC 1_21a	NOSAMS	4722	0.9068	0.0040	-99.41	785	35	-30	26	1	420	495	1.00	450	322	32	332	7	-2	0.9	453	36
GOMBC 1_22a	NOSAMS	5173	0.9081	0.0029	-98.16	775	25	-30	26	1	420	485	1.00	450	358	36	332	8	2.2	1	443	26
GOMBC 1_9a	NOSAMS	5743	0.9349	0.0050	-71.49	540	40	-30	26	1	140	265	1.00	200	406	41	311	8	10.3	1	229	41
GOMBC 1_23a	NOSAMS	6457	0.9231	0.0034	-103.1	820	30	-30	26	1	450	510	1.00	480	461	46	359	12	11	1.5	461	32
GOMBC 1_24a	NOSAMS	6763	0.9044	0.0032	-101.82	805	30	-30	26	1	440	500	1.00	470	495	50	416	12	8.7	1.5	389	32
GOMBC 1_12a	NOSAMS	7604	0.8743	0.0027	-131.70	1080	25	-30	26	1	635	695	1.00	670	561	56	604	12	-7.5	1.5	476	28
GOM_TOW_BC1	(Prouty et al. 2011)		Milled	Transect				-30	26													
145279	LLNL-CAMS	0	0.9335	0.0039	-73.10	550	35	-30	26	2	145 180	165 275	0.16 0.84	210	2003							
145280	LLNL-CAMS	5100	0.9028	0.0031	-103.66	820	30	-30	26	1	450	510	1.00	480	348	35	347	7	-0.9	0.9	473	31
145281	LLNL-CAMS	9750	0.8737	0.0034	-132.53	1090	35	-30	26	1	635	705	1.00	670	575	58	652	11	-11.5	1.4	438	37
GOM_TOW_BC2	(Prouty et al. 2011)		Delaminated	Transect																		
1.1	KCCAMS	191	1.0549	0.0018	47.26	>Moderm		-30	26						1979							
1.2	KCCAMS	383	0.9516	0.0017	-55.29	400 a	15	-30	26						1952							
1.3	KCCAMS	574	0.9474	0.0016	-59.47	435	15	-30	26	1	0	95	1.00	70	21	2	152	7	-16.4	0.9	283	17
1.4	KCCAMS	766	0.9413	0.0016	-65.54	485	15	-30	26	1	100	230	1.00	145	43	4	83	7	-4.9	0.9	402	17
2a.1	KCCAMS	1539	0.9395	0.0018	-67.29	500	20	-30	26	1	125	240	1.00	170	137	14	132	8	0.5	1	368	22
3a.1	KCCAMS	3021	0.9172	0.0017	-89.40	695	15	-30	26	1	320	410	1.00	370	293	29	239	7	6	0.9	456	17
4.1	KCCAMS	4194	0.8658	0.0018	-140.45	1160	20	-30	26	1	680	755	1.00	725	413	41	304	7	12.4	0.9	856	21
7.1	KCCAMS	6153	0.8480	0.0014	-158.15	1330	15	-30	26	1	870	945	1.00	905	614	61	575	11	2.8	1.4	755	19
8.1	KCCAMS	7562	0.7576	0.0013	-247.88		15	-30	26						744	74	857	11	-16.4	1.3		
9.1	KCCAMS	9027	0.8273	0.0014	-178.68	1530	15	-30	26	1	1070	1155	1.00	1110	865	87	929	10	-10.9	1.2	601	18
10.1	KCCAMS	10035	0.8235	0.0015	-182.47	1560	15	-30	26	1	1110	1210	1.00	1150	944	94	1043	11	-15.4	1.3	517	19
11.5	KCCAMS	11379	0.7765	0.0013	-229.10	2030	15	-30	26	1	1590	1685	1.00	1630	1074	107	1186	13	-17.4	1.6	844	20
GOM_TOW_BC2	(Prouty et al. 2011)		Milled	Transect																		
145276	CAMS	0	0.9580	0.0033	-48.81	345	30	-30	26						2003							
145277	CAMS	8500	0.8184	0.0037	-157.36	1610	40	-30	26	1	1160	1260	1.00	1200	829	83	938	12	-16.2	1.5	672	42
145278	CAMS	15000	0.7706	0.0035	-234.85	2100	40	-30	26	1	1650	1790	1.00	1710	1095	110	1199	12	-16.7	1.5	901	42
STET_JSL05_4904_BC1																						
STET 1	N104995	18	1.0739	0.0036	73.90	>Modern		39	16						2005							
STET 1.7	N104996	144	1.0655	0.0048	65.50	>Modern		39	16						2003							
STET 1.16A	N104997	306	0.9539	0.0033	-46.10	380	30	39	16						1995							
STET 1.16B	N104998	306	0.9479	0.0039	-52.10	430	35	39	16						1995							
STET 1.24	N104999	450	0.9446	0.0036	-55.40	460	35	39	16						1979							
STET 1.32	N105000	594	0.9442	0.0039	-55.80	460	35	39	16						1965							
STET 1.41	N105001	756	0.9385	0.0033	-61.50	510	30	39	16	2	0 40	30 118	0.28 0.72	80	1953							
STET 1.57	N105002	1044	0.9263	0.0032	-73.70	615	30	39	16	2	146 185	165 268	0.17 0.83	215	28	3	129	7	-12.4	0.9	486	31

STET 1.83*	N105003	1512	0.9168	0.0032	-83.20	700	30	39	16	2	264 344	336 356	0.92 0.08	310	70	7	104	7	-4.5	0.9	596	31	
STET 2.15	N105004	1998	0.9154	0.0032	-84.60	710	30	39	16	1	274	360	1.00	320	135	14	111	8	2.5	1	599	31	
STET 2.43	N105005	2502	0.9057	0.0032	-94.30	795	30	39	16	2	337 357	343 450	0.04 0.96	400	178	18	176	8	-0.1	1	619	31	
STET 2.71	N105006	2988	0.8905	0.0031	-109.50	930	30	39	16	1	481	528	1.00	505	232	23	93	7	17	0.9	837	31	
STET 3.3B	N105007	3498	0.8794	0.0031	-120.60	1030	30	39	16	1	543	614	1.00	570	278	28	181	8	11.4	1	849	31	
STET 3.36	N105008	4008	0.8858	0.0031	-114.20	975	30	39	16	1	498	561	1.00	535	312	31	306	7	0	0.9	669	31	
STET 3.69*	N105009	4503	0.8740	0.0032	-126.00	1080	30	39	16	2	566 591	579 650	0.15 0.85	615	361	36	332	8	2.2	1	748	31	
STET 3.105	N105010	4998	0.8603	0.0030	-139.70	1210	30	39	16	1	671	741	1.00	715	416	42	304	7	12.4	0.9	906	31	
STET 4.23*	N105011	5513	0.8533	0.0030	-146.70	1275	30	39	16	1	723	822	1.00	780	458	46	359	12	11	1.5	916	32	
STET 5.1	N105012	6021	0.8561	0.0036	-143.90	1250	35	39	16	1	695	788	1.00	750	500	50	416	12	8.7	1.5	834	37	
STET 5.61	N105013	6501	0.8167	0.0029	-183.30	1625	30	39	16	1	1102	1208	1.00	1150	542	54	560	11	-3.8	1.4	1065	32	
STET 5.124	N105014	7005	0.8515	0.0030	-148.50	1290	30	39	16	1	739	844	1.00	800	580	58	646	12	-10.2	1.5	644	32	
STET 6.6A	N105015	7503	0.8330	0.0029	-167.00	1470	30	39	16	1	927	1012	1.00	980	606	61	591	11	-0.4	1.4	879	32	
STET 6.6B	N105016	7503	0.8364	0.0029	-163.60	1435	30	39	16	1	903	976	1.00	945	606	61	591	11	-0.4	1.4	844	32	
STET 6.33A	N105017	8016	0.8352	0.0029	-164.80	1445	30	39	16	1	910	986	1.00	955	623	62	589	11	2.3	1.4	856	32	
STET 6.33B	N105018	8016	0.8354	0.0029	-164.60	1445	30	39	16	1	910	986	1.00	955	623	62	589	11	2.3	1.4	856	32	
STET 7.67	N105019	9507	0.7973	0.0031	-202.70	1820	35	39	16	1	1283	1358	1.00	1325	696	70	795	11	-14.8	1.3	1025	37	
STET 7.94	N105020	10011	0.8067	0.0028	-193.30	1725	30	39	16	1	1216	1284	1.00	1250	716	72	807	10	-13.9	1.2	918	32	
STET 7.123	N105021	10533	0.8441	0.0030	-155.90	1360	30	39	16	1	822	911	1.00	865	730	73	821	10	-13.8	1.2	539	32	
STET 1.149	N105022	11001	0.8421	0.0030	-157.90	1380	30	39	16	1	839	927	1.00	890	732	73	840	10	-15.5	1.2	540	32	
STET_JSL05_4904_BC2																							
4904_BC2_outer	164343	0	0.9778	0.0034	-22.2	180	30	39	16						2005								
4904_BC2_mid	164344	7200	0.9198	0.0032	-80.2	670	30	39	16	1	245	312	1.00	280	516	52	476	11	3	1.4	194	32	
4904_BC2_ctr	164345	9360	0.8829	0.0031	-117.1	1000	30	39	16	2	519 575	570 597	0.75 0.25	560	630	63	600	12	1.5	1.5	400	32	